Automated Left Ventricle Detection

in Gated Radionuclide Ventriculography

Via Fuzzy Clustering

by

Boyd M.C. McCurdy

A thesis submitted to the Faculty of Graduate Studies of the University of Manitoba
in Partial Fulfillment of the Requirements for the Degree of

MASTER OF SCIENCE

Department of Physics

University of Manitoba

Winnipeg, Canada

ISBN 0-612-13358-3

Name _____

Dissertation Abstracts International and *Masters Abstracts International* are arranged by broad, general subject categories. Please select the one subject which most nearly describes the content of your dissertation or thesis. Enter the corresponding four-digit code in the spaces provided.

Biophysics - Medical
SUBJECT TERM

0760
SUBJECT CODE

UMI

Subject Categories

THE HUMANITIES AND SOCIAL SCIENCES

COMMUNICATIONS AND THE ARTS
Architecture 0729
Art History 0377
Cinema 0900
Dance 0378
Fine Arts 0357
Information Science 0723
Journalism 0391
Library Science 0399
Mass Communications 0708
Music 0413
Speech Communication 0459
Theater 0465

EDUCATION
General 0515
Administration 0514
Adult and Continuing 0516
Agricultural 0517
Art 0273
Bilingual and Multicultural 0282
Business 0688
Community College 0275
Curriculum and Instruction 0727
Early Childhood 0518
Elementary 0524
Finance 0277
Guidance and Counseling 0519
Health 0680
Higher 0745
History of 0520
Home Economics 0278
Industrial 0521
Language and Literature 0279
Mathematics 0280
Music 0522
Philosophy of 0998
Physical 0523
Psychology 0525
Reading 0535
Religious 0527
Sciences 0714
Secondary 0533
Social Sciences 0534
Sociology of 0340
Special 0529
Teacher Training 0530
Technology 0710
Tests and Measurements 0288
Vocational 0747

LANGUAGE, LITERATURE AND LINGUISTICS
Language
- General 0679
- Ancient 0289
- Linguistics 0290
- Modern 0291

Literature
- General 0401
- Classical 0294
- Comparative 0295
- Medieval 0297
- Modern 0298
- African 0316
- American 0591
- Asian 0305
- Canadian (English) 0352
- Canadian (French) 0355
- English 0593
- Germanic 0311
- Latin American 0312
- Middle Eastern 0315
- Romance 0313
- Slavic and East European 0314

PHILOSOPHY, RELIGION AND THEOLOGY
Philosophy 0422
Religion
- General 0318
- Biblical Studies 0321
- Clergy 0319
- History of 0320
- Philosophy of 0322

Theology 0469

SOCIAL SCIENCES
American Studies 0323
Anthropology
- Archaeology 0324
- Cultural 0326
- Physical 0327

Business Administration
- General 0310
- Accounting 0272
- Banking 0770
- Management 0454
- Marketing 0338

Canadian Studies 0385
Economics
- General 0501
- Agricultural 0503
- Commerce-Business 0505
- Finance 0508
- History 0509
- Labor 0510
- Theory 0511

Folklore 0358
Geography 0366
Gerontology 0351
History
- General 0578
- Ancient 0579
- Medieval 0581
- Modern 0582
- Black 0328
- African 0331
- Asia, Australia and Oceania 0332
- Canadian 0334
- European 0335
- Latin American 0336
- Middle Eastern 0333
- United States 0337

History of Science 0585
Law 0398
Political Science
- General 0615
- International Law and Relations 0616
- Public Administration 0617

Recreation 0814
Social Work 0452
Sociology
- General 0626
- Criminology and Penology 0627
- Demography 0938
- Ethnic and Racial Studies 0631
- Individual and Family Studies 0628
- Industrial and Labor Relations 0629
- Public and Social Welfare 0630
- Social Structure and Development 0700
- Theory and Methods 0344

Transportation 0709
Urban and Regional Planning 0999
Women's Studies 0453

THE SCIENCES AND ENGINEERING

BIOLOGICAL SCIENCES
Agriculture
- General 0473
- Agronomy 0285
- Animal Culture and Nutrition 0475
- Animal Pathology 0476
- Food Science and Technology 0359
- Forestry and Wildlife 0478
- Plant Culture 0479
- Plant Pathology 0480
- Plant Physiology 0817
- Range Management 0777
- Wood Technology 0746

Biology
- General 0306
- Anatomy 0287
- Biostatistics 0308
- Botany 0309
- Cell 0379
- Ecology 0329
- Entomology 0353
- Genetics 0369
- Limnology 0793
- Microbiology 0410
- Molecular 0307
- Neuroscience 0317
- Oceanography 0416
- Physiology 0433
- Radiation 0821
- Veterinary Science 0778
- Zoology 0472

Biophysics
- General 0786
- Medical 0760

EARTH SCIENCES
Biogeochemistry 0425
Geochemistry 0996
Geodesy 0370
Geology 0372
Geophysics 0373
Hydrology 0388
Mineralogy 0411
Paleobotany 0345
Paleoecology 0426
Paleontology 0418
Paleozoology 0985
Palynology 0427
Physical Geography 0368
Physical Oceanography 0415

HEALTH AND ENVIRONMENTAL SCIENCES
Environmental Sciences 0768
Health Sciences
- General 0566
- Audiology 0300
- Chemotherapy 0992
- Dentistry 0567
- Education 0350
- Hospital Management 0769
- Human Development 0758
- Immunology 0982
- Medicine and Surgery 0564
- Mental Health 0347
- Nursing 0569
- Nutrition 0570
- Obstetrics and Gynecology 0380
- Occupational Health and Therapy 0354
- Ophthalmology 0381
- Pathology 0571
- Pharmacology 0419
- Pharmacy 0572
- Physical Therapy 0382
- Public Health 0573
- Radiology 0574
- Recreation 0575
- Speech Pathology 0460
- Toxicology 0383

Home Economics 0386

PHYSICAL SCIENCES
Pure Sciences
Chemistry
- General 0485
- Agricultural 0749
- Analytical 0486
- Biochemistry 0487
- Inorganic 0488
- Nuclear 0738
- Organic 0490
- Pharmaceutical 0491
- Physical 0494
- Polymer 0495
- Radiation 0754

Mathematics 0405
Physics
- General 0605
- Acoustics 0986
- Astronomy and Astrophysics 0606
- Atmospheric Science 0608
- Atomic 0748
- Electronics and Electricity 0607
- Elementary Particles and High Energy 0798
- Fluid and Plasma 0759
- Molecular 0609
- Nuclear 0610
- Optics 0752
- Radiation 0756
- Solid State 0611

Statistics 0463

Applied Sciences
Applied Mechanics 0346
Computer Science 0984
Engineering
- General 0537
- Aerospace 0538
- Agricultural 0539
- Automotive 0540
- Biomedical 0541
- Chemical 0542
- Civil 0543
- Electronics and Electrical 0544
- Heat and Thermodynamics 0348
- Hydraulic 0545
- Industrial 0546
- Marine 0547
- Materials Science 0794
- Mechanical 0548
- Metallurgy 0743
- Mining 0551
- Nuclear 0552
- Packaging 0549
- Petroleum 0765
- Sanitary and Municipal 0554
- System Science 0790

Geotechnology 0428
Operations Research 0796
Plastics Technology 0795
Textile Technology 0994

PSYCHOLOGY
General 0621
Behavioral 0384
Clinical 0622
Developmental 0620
Experimental 0623
Industrial 0624
Personality 0625
Physiological 0989
Psychobiology 0349
Psychometrics 0632
Social 0451

Nom _____

Dissertation Abstracts International est organisé en catégories de sujets. Veuillez s.v.p. choisir le sujet qui décrit le mieux votre thèse et inscrivez le code numérique approprié dans l'espace réservé ci-dessous.

_____ ☐☐☐ U·M·I

SUJET — CODE DE SUJET

Catégories par sujets

HUMANITÉS ET SCIENCES SOCIALES

COMMUNICATIONS ET LES ARTS
Architecture 0729
Beaux-arts 0357
Bibliothéconomie 0399
Cinéma 0900
Communication verbale 0459
Communications 0708
Danse 0378
Histoire de l'art 0377
Journalisme 0391
Musique 0413
Sciences de l'information 0723
Théâtre 0465

ÉDUCATION
Généralités 515
Administration 0514
Art 0273
Collèges communautaires 0275
Commerce 0688
Économie domestique 0278
Éducation permanente 0516
Éducation préscolaire 0518
Éducation sanitaire 0680
Enseignement agricole 0517
Enseignement bilingue et multiculturel 0282
Enseignement industriel 0521
Enseignement primaire. 0524
Enseignement professionnel 0747
Enseignement religieux 0527
Enseignement secondaire 0533
Enseignement spécial 0529
Enseignement supérieur 0745
Évaluation 0288
Finances 0277
Formation des enseignants 0530
Histoire de l'éducation 0520
Langues et littérature 0279
Lecture 0535
Mathématiques 0280
Musique 0522
Orientation et consultation 0519
Philosophie de l'éducation 0998
Physique 0523
Programmes d'études et enseignement 0727
Psychologie 0525
Sciences 0714
Sciences sociales 0534
Sociologie de l'éducation 0340
Technologie 0710

LANGUE, LITTÉRATURE ET LINGUISTIQUE
Langues
- Généralités 0679
- Anciennes 0289
- Linguistique 0290
- Modernes 0291

Littérature
- Généralités 0401
- Anciennes 0294
- Comparée 0295
- Médiévale 0297
- Moderne 0298
- Africaine 0316
- Américaine 0591
- Anglaise 0593
- Asiatique 0305
- Canadienne (Anglaise) 0352
- Canadienne (Française) 0355
- Germanique 0311
- Latino-américaine 0312
- Moyen-orientale 0315
- Romane 0313
- Slave et est-européenne 0314

PHILOSOPHIE, RELIGION ET THÉOLOGIE
Philosophie 0422
Religion
- Généralités 0318
- Clergé 0319
- Études bibliques 0321
- Histoire des religions 0320
- Philosophie de la religion 0322

Théologie 0469

SCIENCES SOCIALES
Anthropologie
- Archéologie 0324
- Culturelle 0326
- Physique 0327

Droit 0398
Économie
- Généralités 0501
- Commerce-Affaires 0505
- Économie agricole 0503
- Économie du travail 0510
- Finances 0508
- Histoire 0509
- Théorie 0511

Études américaines 0323
Études canadiennes 0385
Études féministes 0453
Folklore 0358
Géographie 0366
Gérontologie 0351
Gestion des affaires
- Généralités 0310
- Administration 0454
- Banques 0770
- Comptabilité 0272
- Marketing 0338

Histoire
- Histoire générale 0578
- Ancienne 0579
- Médiévale 0581
- Moderne 0582
- Histoire des noirs 0328
- Africaine 0331
- Canadienne 0334
- États-Unis 0337
- Européenne 0335
- Moyen-orientale 0333
- Latino-américaine 0336
- Asie, Australie et Océanie 0332

Histoire des sciences 0585
Loisirs 0814
Planification urbaine et régionale 0999
Science politique
- Généralités 0615
- Administration publique 0617
- Droit et relations internationales 0616

Sociologie
- Généralités 0626
- Aide et bien-être social 0630
- Criminologie et établissements pénitentiaires 0627
- Démographie 0938
- Études de l' individu et de la famille 0628
- Études des relations interethniques et des relations raciales 0631
- Structure et développement social 0700
- Théorie et méthodes. 0344
- Travail et relations industrielles 0629

Transports 0709
Travail social 0452

SCIENCES ET INGÉNIERIE

SCIENCES BIOLOGIQUES
Agriculture
- Généralités 0473
- Agronomie. 0285
- Alimentation et technologie alimentaire 0359
- Culture 0479
- Élevage et alimentation 0475
- Exploitation des pâturages 0777
- Pathologie animale 0476
- Pathologie végétale 0480
- Physiologie végétale 0817
- Sylviculture et faune 0478
- Technologie du bois 0746

Biologie
- Généralités 0306
- Anatomie 0287
- Biologie (Statistiques) 0308
- Biologie moléculaire 0307
- Botanique 0309
- Cellule 0379
- Écologie 0329
- Entomologie 0353
- Génétique 0369
- Limnologie 0793
- Microbiologie 0410
- Neurologie 0317
- Océanographie 0416
- Physiologie 0433
- Radiation 0821
- Science vétérinaire 0778
- Zoologie 0472

Biophysique
- Généralités 0786
- Medicale 0760

SCIENCES DE LA TERRE
Biogéochimie 0425
Géochimie 0996
Géodésie 0370
Géographie physique 0368
Géologie 0372
Géophysique 0373
Hydrologie 0388
Minéralogie 0411
Océanographie physique 0415
Paléobotanique 0345
Paléoécologie 0426
Paléontologie 0418
Paléozoologie 0985
Palynologie 0427

SCIENCES DE LA SANTÉ ET DE L'ENVIRONNEMENT
Économie domestique 0386
Sciences de l'environnement 0768
Sciences de la santé
- Généralités 0566
- Administration des hôpitaux 0769
- Alimentation et nutrition 0570
- Audiologie 0300
- Chimiothérapie 0992
- Dentisterie 0567
- Développement humain 0758
- Enseignement 0350
- Immunologie 0982
- Loisirs 0575
- Médecine du travail et thérapie 0354
- Médecine et chirurgie 0564
- Obstétrique et gynécologie 0380
- Ophtalmologie 0381
- Orthophonie 0460
- Pathologie 0571
- Pharmacie 0572
- Pharmacologie 0419
- Physiothérapie 0382
- Radiologie 0574
- Santé mentale 0347
- Santé publique 0573
- Soins infirmiers 0569
- Toxicologie 0383

SCIENCES PHYSIQUES
Sciences Pures
Chimie
- Généralités 0485
- Biochimie 487
- Chimie agricole 0749
- Chimie analytique 0486
- Chimie minérale 0488
- Chimie nucléaire 0738
- Chimie organique 0490
- Chimie pharmaceutique 0491
- Physique 0494
- PolymÈres 0495
- Radiation 0754

Mathématiques 0405
Physique
- Généralités 0605
- Acoustique 0986
- Astronomie et astrophysique 0606
- Électronique et électricité 0607
- Fluides et plasma 0759
- Météorologie 0608
- Optique 0752
- Particules (Physique nucléaire) 0798
- Physique atomique 0748
- Physique de l'état solide 0611
- Physique moléculaire 0609
- Physique nucléaire 0610
- Radiation 0756

Statistiques 0463

Sciences Appliqués Et Technologie
Informatique 0984
Ingénierie
- Généralités 0537
- Agricole 0539
- Automobile 0540
- Biomédicale 0541
- Chaleur et thermodynamique 0348
- Conditionnement (Emballage) 0549
- Génie aérospatial 0538
- Génie chimique 0542
- Génie civil 0543
- Génie électronique et électrique 0544
- Génie industriel 0546
- Génie mécanique 0548
- Génie nucléaire 0552
- Ingénierie des systèmes 0790
- Mécanique navale 0547
- Métallurgie 0743
- Science des matériaux 0794
- Technique du pétrole 0765
- Technique minière 0551
- Techniques sanitaires et municipales 0554
- Technologie hydraulique 0545

Mécanique appliquée 0346
Géotechnologie 0428
Matières plastiques (Technologie) 0795
Recherche opérationnelle 0796
Textiles et tissus (Technologie) 0794

PSYCHOLOGIE
Généralités 0621
Personnalité 0625
Psychobiologie 0349
Psychologie clinique 0622
Psychologie du comportement 0384
Psychologie du développement 0620
Psychologie expérimentale 0623
Psychologie industrielle 0624
Psychologie physiologique 0989
Psychologie sociale 0451
Psychométrie 0632

THE UNIVERSITY OF MANITOBA

FACUTY OF GRADUATE STUDIES

COPYRIGHT PERMISSION

AUTOMATED LEFT VENTRICLE DETECTION IN GATED RADIONUCLIDE VENTRICULOGRAPHY VIA FUZZY CLUSTERING

BY

BOYD M.C. MCCURDY

A Thesis/Practicum submitted to the Faculty of Graduate Studies of the University of Manitoba in partial fulfillment of the requirements for the degree of

MASTER OF SCIENCE

Abstract

Gated radionuclide ventriculography is a procedure commonly used to assess cardiac function. A time sequence of images representing the blood pool volume over a single heart beat is acquired. These studies are then analysed to extract a quantitative parameter representing contraction efficiency of the left ventricle, termed 'ejection fraction'.

Currently implemented automated left ventricle recognition techniques rely on edge-detection methods. A more adaptable algorithm based on a double application of the fuzzy *c*-means clustering algorithm was developed. The fuzzy technique was optimised using a set of ten test images, to yield a global set of parameters which were then used to reanalyse the entire test group. The performance of the fuzzy method correlated well ($r = 0.90$) with a manual method used by a human operator. A systematic 7.8% underestimation of ejection fraction by the fuzzy method was shown to be attributable to the fact that the fuzzy *c*-means technique tends to use a tighter left ventricle boundary identification than does a typical manual analysis.

A comprehensive list of possible error sources affecting ejection fraction measurement was compiled. This prompted a preliminary investigation of the effects of photon attenuation within the blood volume. A computer program was written to model the attenuation effects and estimate the magnitude of attenuation effects on the measured ejection fraction. A novel technique for correcting the ejection fraction estimate for blood volume attenuation effects was developed.

Acknowledgements

I would like to thank my supervisors, Dr. Norm Davison and Dr. Roger Palser for providing guidance and assistance. I would also like to thank my parents for their continued support and encouragement in all my pursuits.

A hearty thank you to the Natural Sciences and Engineering Research Counsel (NSERC) for providing the primary funding for this project. Thank you to Dr. Stephen Pistorius for allowing time to finish this work.

Finally, I would like to extend my gratitude to friends and colleagues who have put up with my whining: Himu Shukla, Kurt Luchka, Collins Yeboah, Richard Lee, and Randy Roels.

Table of Contents

Chapter One: BACKGROUND TO CARDIAC EJECTION FRACTION MEASUREMENT

1.0 Introduction

One of the primary uses of cardiac scintigraphy is the evaluation of left ventricular function through quantitative analysis. Equilibrium gated blood pool imaging permits visualization of the distributed blood volume within the heart chambers as a function of time within a representative cardiac cycle. The technique generates both qualitative and quantitative data; ventricular wall motion is visualized and analysis of the same images provides parameters for the assessment of ventricular function. The most important quantitative parameter for left ventricle (LV) assessment is the ejection fraction (EF). This is defined as the ratio of blood volume ejected from the LV to maximum blood volume of the LV.

Estimation of LV EF requires the delineation of the LV contour from the sequence of two-dimensional images taken throughout the cardiac cycle, as well as an appropriate background subtraction. The quantification of the EF parameter from the gated blood pool images involves two major assumptions (Green, 1978):

(1) the externally measured LV count rate at the gamma camera is absolutely proportional to the LV volume, and

(2) all cardiac cycles during the image acquisition period are mechanically identical.

The first assumption is violated due to attenuation of radioactivity by intervening tissue, including the LV blood volume itself. Due to naturally occurring heart rate fluctuations,

the second assumption is also violated. The contravention of these assumptions and the effects on EF estimation are further discussed in chapter two.

Manual methods of finding LV EF are characterized by relatively large inter- and intra-observer variations, which hamper the assessment of effects of interventions on EF (Okada, 1980; Burow, 1977). To reduce this variability, several semi-automatic and fully automatic methods for calculating LV EF from gated blood pool studies have been developed since the introduction of this imaging technique. These approaches include several variations of edge detection such as first derivative (Douglas, 1978), second derivative (Christian, 1985), combination first and second derivative (Links, 1982), ellipsoidally restricted edge detection (MacIntyre, 1982), second derivative combined with minimal cost contouring (Reiber, 1985, 1983), second derivative combined with thresholding (Slutsky, 1980), interpolative schemes (Almasi, 1982), non-linear edge operators (Chang, 1980), best-fit edge detection (Chang, 1980), bidirectional scanning combined with functional criteria (Goris, 1978), and Gram-Schmidt processing combined with edge following (Jouan, 1990). Virtually all previous methods of LV identification have been highly dependent on edge detection.

At the Health Sciences Centre (HSC) in Winnipeg, approximately 10-15 equilibrium gated blood pool studies are performed each week. These studies are analysed by a manual method as well as a semi-automated routine, and saved (via film hardcopy) in the patient's permanent records. A fully automated analysis available in the software is not utilized due to unreliable performance. The LV ROI's identified by the

automated algorithms are derived through the thresholding and second derivative process as described by Slutsky (1980).

It was felt that exploration of an automated approach to LV ROI recognition which involved less edge detection than classical methods might lead to a more reliable algorithm. Fuzzy clustering is a well explored topic and generally applicable in the research areas of pattern recognition and artificial intelligence, and thus a logical choice for application to LV boundary identification. Arguments justifying this choice are presented in section 1.3.1.

This work has several objectives:

(1) Develop a working computer program capable of identifying, through the application of fuzzy clustering techniques, the LV in an equilibrium gated blood pool scan of a normal patient. This is described in chapter three.

(2) By automating the background activity correction process, the ejection fraction parameter may be quantified without manual intervention. This particular process is discussed further in section 3.5. A comparison between the automated and manual methods of background activity estimation is given in section 5.2.

(3) Another aim is to compile a detailed list of possible error sources affecting the absolute uncertainty of any single measurement of ejection fraction. This comprises the entirety of chapter two.

(4) A novel and simple method of correcting ejection fraction estimates for blood volume self-attenuation is developed and presented in chapter four.

The results of the fuzzy clustering based automated algorithm applied to a limited number of clinical images are presented in chapter five. A brief overview of the equilibrium gated blood pool imaging process and the mathematical basis of fuzzy clustering is supplied below.

1.1 Gated Blood Pool Imaging

1.1.1 Red Blood Cell Labeling

In order to be imaged, the red blood cells must first be 'labeled' with a radioactive compound and then observed with a properly tuned scintillation or 'gamma' camera (Sharp, 1989; Palmer, 1991; Cardiac Imaging, 1991). Red blood cell labeling generally employs a radiopharmaceutical which remains within the intravascular space. The standard radioactive compound used for this type of imaging is Technetium-99m, which emits photons of energy 140 KeV. There are several procedures for tagging the red blood cells: in vivo, modified in vivo, and in vitro.

The in vivo process involves intravenous administration of approximately 10-20 μg of stannous ion per kg body weight, followed after 20 minutes by about 740 Mbq (20 mCi) of $^{99m}TcO_4^-$. During the 20 minute interval, the stannous ion (Sn^{2+}) enters the red blood cells and excess ion clears from the plasma. Immediately upon injection, $^{99m}TcO_4^-$ diffuses into the red blood cells, where it is reduced by the stannous ion and binds to the beta chain of hemoglobin. Some of the $^{99m}TcO_4^-$ diffuses into the extracellular fluid, and some labels plasma elements in addition to red blood cells. The modified in vivo technique is similar to the in vivo, but after the 20 minute interval, a small quantity of blood (2-5 mL) is withdrawn into a syringe containing about 740 Mbq (20 mCi) of $^{99m}TcO_4^-$. The cells incubate in the syringe at room temperature for 10 to 15 minutes before reinjection. This modification of the in vivo method results in a reduction in diffusion of $^{99m}TcO_4^-$ into extracellular space at the cost of increased time.

The in vitro labeling process is entirely carried out external to the patient. The procedure involves stannous reduction of a small amount of patient's blood in a syringe. The red cells are separated from plasma elements by centrifugation and then labeled with $^{99m}TcO_4^-$. The in vitro method results in the best signal-to-noise ratio of the three

labeling methods. However, the in vivo method is the easiest to perform and requires the shortest amount of time to complete, at a cost of a reduced signal-to-noise ratio. The nuclear medicine department at the HSC utilizes in vivo labeling.

1.1.2 Dosimetry

The dosimetry of gated blood pool imaging depends in part upon the efficiency of the red blood cell labeling. For the in vivo method of labeling, a binding efficiency of 75% is typical. An estimation of absorbed dose for several organs is given in Table 1.1. Structures containing blood, such as the heart, receive about 10 mGy per 750 MBq dose. Shortly after injection, loosely bound Tc^{99m} is excreted in the urine. Dose to the bladder may be reduced if the patient voids frequently.

Organ	Absorbed Dose (mGy/750 MBq)
Spleen	3.6
Bladder wall	24.0
Testes	2.4
Ovaries	4.6
Blood	10.4
Whole body	3.2

Table 1.1: Estimated absorbed radiation dose from labeled red blood cells [source: Palmer, *et.al.*, 1991].

1.1.3 Image Acquisition

1.1.3.1 Protocol

After injection of the 750 MBq dose an interval of 5 minutes is allowed for the activity in the blood to achieve equilibrium before the image acquisition is begun. Otherwise, a slow rise and fall of activity will be observed corresponding to the passing of the injection bolus. Standard protocol decrees that studies at three views be obtained. This enables one to observe, as far as possible, the complete anatomy of both ventricles and the separation of both ventricles with the septum end-on in at least one view. These views include a left lateral, an anterior, and a left anterior oblique (LAO) view, as depicted in Figure 1.1. At HSC the LAO view is taken as the best septal view (ie. where the left and right ventricles are readily distinguished). This view is found through manual adjustment of the gamma camera position while the technician examines the real-time image of the heart. The anterior view is attained at minus 40° rotation with respect to the LAO view about the head-foot axis of the patient (counter-clockwise as viewed from the feet) , while the left lateral view is taken at plus 30°. The LAO view is collected for 600 s, while the other two views are collected for 300 s each. The LAO view is acquired with better statistics (due to the longer imaging time), since it is involved in several quantitative analyses of heart function, and therefore needs to be as accurate as reasonably possible. Approximately 8×10^6 counts are collected during a 600 s imaging time.

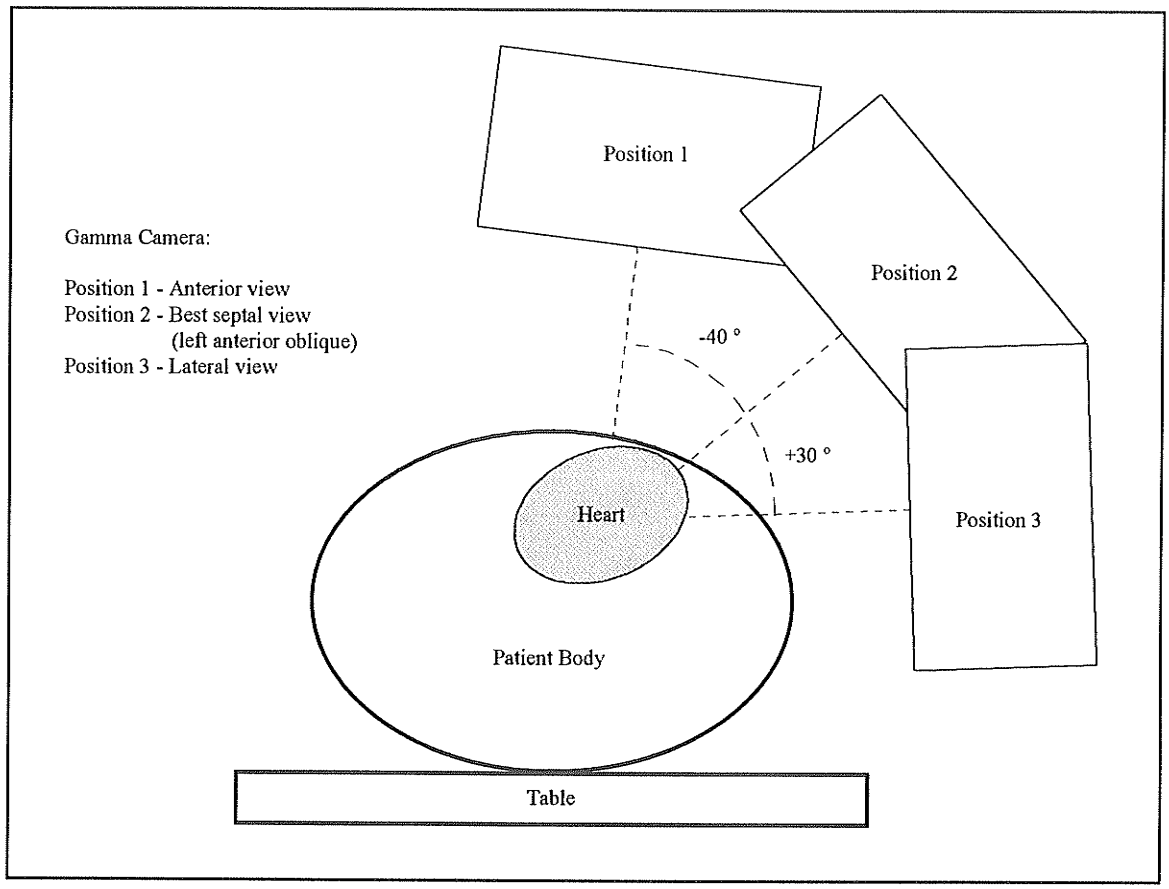

Figure 1.1: Cross sectional diagram of camera-patient geometry for three standard gated blood pool scans as viewed along patient axis from feet direction.

1.1.3.2 Gating

The amount of radioactivity uniformly distributed throughout the blood volume is much too small for a useful image to be acquired over a single cardiac cycle. However, by summing the activity measured over several hundred cardiac cycles, an image with adequate statistics may be attained. An electrocardiogram (ECG) serves as the gate for the purpose of defining the beginning of each cardiac contraction, and hence differentiating successive heart beats for imaging purposes. The image acquisition for each cardiac cycle is initiated by the strong R wave electrical pulse of the heart. This pulse initiates the depolarization of the ventricular walls from endocardium toward

epicardium (ie. ventricular contraction) Contraction of the ventricle chambers is termed ventricular *systole*, and is followed by a time period where the chambers are relaxed, termed *diastole*. The R wave of the ECG identifies the onset of mechanical systole as the reference point for the imaging. At HSC a four electrode configuration is used to obtain the ECG signal for the patient, but these positions may be modified to ensure a strong R-wave triggering signal.

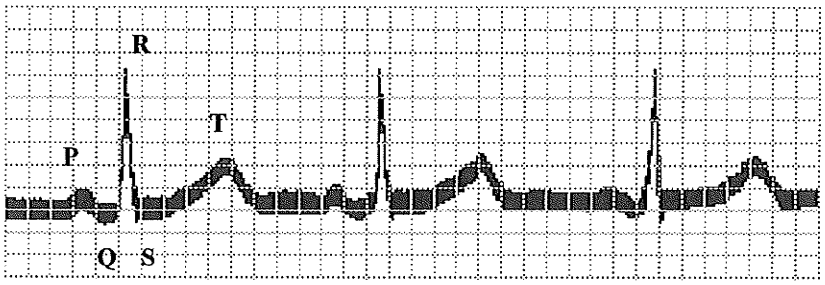

Figure 1.2: Normal output of an electrocardiogram lead, demonstrating a strong R-wave pulse from which the gated image acquisition is triggered. Vertical lines are 65 ms apart, R-wave pulse height is approximately 1 mV. [adapted from Patton, *et.al.*, 1989]

1.1.3.3 Frame Time

Generally the cardiac cycle is divided into 16 to 32 frames and varies between institutions. At HSC the cycle is separated into 24 frames. Thus, the length of time each frame represents is:

$$\text{time per frame} = \frac{time\ of\ one\ heart\ beat}{24\ frames\ per\ heart\ beat} = \frac{60}{24 * heart\ rate\ (bpm)}$$

where *bpm* represents the heart rate as measured in beats per minute. Ideally, a frame time of 0.025 to 0.030 s should be used, since end systole may last as little as 0.050 s.

This is simple application of the Shannon-Whittaker sampling theorem. If frame times of longer length are employed, it may be possible that no single frame will occupy end systole, resulting in an overestimation of minimum ventricular volume. Consequently, ejection fraction will be underestimated also. This error is rendered negligible if the frame time is kept below 0.050 s. The equation above yields a minimum heart rate of 50 bpm if the frame time is to be kept below 0.050 s. Any heart rate above this will decrease the time per frame. The impact of frame time choice upon reproduction of an accurate volume activity curve is further discussed in section 2.1.2.1.

1.1.3.4 Beat Rejection

During the course of the image acquisition, the heart rate will normally vary. However, in certain situations (such as arrythmia), the patient may experience a highly fluctuating heart rate. Premature heart beats are identified as those cardiac cycles whose R-R interval are much shorter than the average R-R interval as measured over the duration of the acquisition. The beat following an abnormal beat is also abnormal due to the abnormal filling and emptying of cardiac chambers during the bad beat. If the premature beats (PB) are frequent, the gating process will result in an image consisting of a superposition of normal, PB's, and post PB's. In this situation the evaluation of cardiac function with respect to normal beats will in error. To circumvent this problem, abnormal beats must be detected and rejected.

By defining a beat length window before the acquisition, the user can specify the limits for rejection or acceptance of a heart beat. At HSC, a 15% window is used to allow for the normal variation in R-R interval lengths. A running average of cycle length is kept during image acquisition. Only those beats which are within the window contribute to the running average. A 15% beat window is thus defined as: $(0.85 \times \overline{time}_{R-R}) \leq time_{R-R} \leq (1.15 \times \overline{time}_{R-R})$. A beat is identified as abnormal if its R-R

interval lies outside this predefined window. The method of rejecting the bad beat or subsequent beats varies with the acquisition mode, as discussed in the following section.

1.1.3.5 Acquisition Modes

There exist several methods of processing the count data acquired in gated blood pool imaging. The two most common are frame mode and list mode.

In frame mode, the data are summed into the study frames as they are acquired in real time. Any data detected during a specific time segment are stored in a corresponding frame on the terminal screen. The presence of a bad beat will not be recognized until all the data from that cardiac cycle have been stored in each of the frames. Hence, it is not possible to reject the data for the bad beat itself. Only subsequent beat(s) following the abnormal one may be rejected. When the R-R interval varies, data collected from short beats are terminated by the arrival of the next R wave. Thus a short cycle will contribute no data to the final frames of a study. Therefore studies in patients with irregular heart beats result in an observable decrease in counts in the final frames. This problem is known as count drop-off. The summation of cardiac cycles tends to blur the data, since the frames from the different cycles do not correspond properly.

In list mode, data for each cycle are acquired into a temporary memory buffer. The data are not included in a study until after the R-R interval length has been accepted. If a bad beat is detected, the data within the temporary buffer are ignored. Thus, the abnormal beat may be rejected, as well as subsequent beats. The count drop-off problem is partially circumvented in this manner. Complete elimination of the count drop-off problem is achieved by acquiring data in the phase mode, which is a variation of the list mode. The phase mode subdivides each cardiac cycle into a preset fixed number of frames, whose individual time lengths vary between cycles corresponding to the length of heart beat. Hence short cycles are stretched and long cycles are compressed to fit the same number of frames for each cardiac cycle. In this manner, the drop-off effect is

eliminated. Beats falling outside the beat window are still rejected. Studies performed at the HSC employ the phase mode.

1.1.3.6 Preprocessing

Two types of smoothing are performed on the raw image data at HSC by the acquisition computer prior to digital storage. A temporal smoothing is performed which smoothes the data along the time axis. Each pixel in each frame is averaged with the corresponding pixels in the previous frame and the following frame. The 24 frame smoothed image set is reformatted into 16 frames, in order to fit a three view study into a single 512×512 pixel image (containing the three 16 frame data sets of size 256×256). A spatial smoothing is also performed, which involves replacing the pixel of interest with a weighted average of the surrounding 3×3 group of pixels within the frame to be smoothed. The weighting of the pixels is dependent on their position, with the convolution mask configured as:

$$Linear\ Filter\ Mask = \frac{1}{16}\begin{pmatrix} 1 & 2 & 1 \\ 2 & 4 & 2 \\ 1 & 2 & 1 \end{pmatrix}$$

1.2 Current Techniques of Finding Ejection Fraction

1.2.1 Introduction

The software currently in use at the HSC provides three methods of analysing gated blood pool images for the ejection fraction parameter. A manual, semi, and fully automated analysis of the left ventricle is available. The manual and semi-automated routines require subjective judgment on the part of the user thus suffering from inter- and intra-observer variabilities. While the fully automated routine removes these inter- and intra-observer subjectivities, there still exists a built in bias in the analysis dependent on the exact particulars of the method employed. The software documentation suggests the fully automated analysis should be reviewed by a trained observer. At the HSC, both the manual and the semi-automated routines are applied to each test, and the results of these analyses are saved on films which are included in the patient's permanent records. The acquired images are stored in an archive, and may be accessed at any future time for review. The fully automated method fails on approximately 15% of studies performed at this site, according to an informal survey of several Nuclear Medicine Department staff members.

It should be noted that the techniques for image acquisition and analysis will vary somewhat between hospitals.

1.2.2 Definition of Ejection Fraction

Left ventriclular ejection fraction is defined as the ratio of the volume of blood discharged from the left ventricle during one contraction to the volume of the left ventricle at end-diastole. If one knows the LV volumes at end-diastole and end-systole, then the ejection fraction (EF) is:

$$EF = \frac{EDV - ESV}{EDV} \tag{1.1}$$

where EDV = end-diastolic volume, and

ESV = end-systolic volume.

It is one of the most important parameters used to evaluate left ventricle performance (Cardiology, 1991).

Gated blood pool scanning is a noninvasive test which is frequently used to estimate LV ejection fraction. By assuming the counts collected in the gamma camera are proportional to the blood volume, conclusions regarding the 3D volume of blood in the LV may be drawn, despite using only planar images. The equation for calculating EF from these images is modified to:

$$EF = \frac{(EDC - n_{ED} \cdot BG) - (ESC - n_{ES} \cdot BG)}{(EDC - n_{ED} \cdot BG)} \tag{1.2}$$

where EDC = sum of counts in LV region of interest (ROI) in end-diastolic view,

ESC = sum of counts in LV ROI in end-systolic view,

BG = background activity estimate per pixel

n_{ED} = number of pixels in end-diastolic LV ROI

n_{ES} = number of pixels in end-systolic LV ROI

This formula employs a LV ROI which varies from frame to frame (generally described as a 'variable ROI' method). In addition, a time independent, spatially uniform background correction is performed

1.2.3 Manual Method

The image data are smoothed temporally and spatially in order to reduce the effects of statistical uncertainty in the data. The temporal smoothing is accomplished by averaging each pixel in each frame with the corresponding pixels in the preceding frame and the next frame. The spatial smoothing is performed by convoluting a weighted 3×3 matrix over each image frame. The smoothing process has been previously described in section 1.1.3.6, where the kernel is also given explicitly.

The user then manually draws a region of interest (ROI) around the left ventricle of the end-diastolic (ED) image. This ROI is applied to all the image frames to generate a preliminary time activity curve (TAC) in order to find the end-systolic (ES) frame. The TAC is generated by summing all the counts lying within the ROI of each image frame, and when registered counts are assumed proportional to blood volume, the TAC is proportional to the time-volume curve. The ES frame is identified as the frame with the lowest activity in the generated TAC. The user then draws a region of interest around the left ventricle (LV) of this frame, and another TAC is generated from this ROI. The user defines a crescent shaped background region by defining the starting and ending angles

(relative to the geometric centre of mass of the LV), the width of the crescent, and the spacing between the crescent and the LV boundary as in Figure 1.3. The background activity per pixel is found and subtracted from each pixel in each ROI for both TAC's. A new left ventricular TAC is produced through linear interpolation of the two initial TAC's which were generated from the fixed ED and ES regions of interest. This interpolation is performed in order to approximate the left ventricular TAC which would be generated from a variable left ventricular ROI. Finally, the ejection fraction is calculated and the analysis is printed out onto film as well as saved to disk.

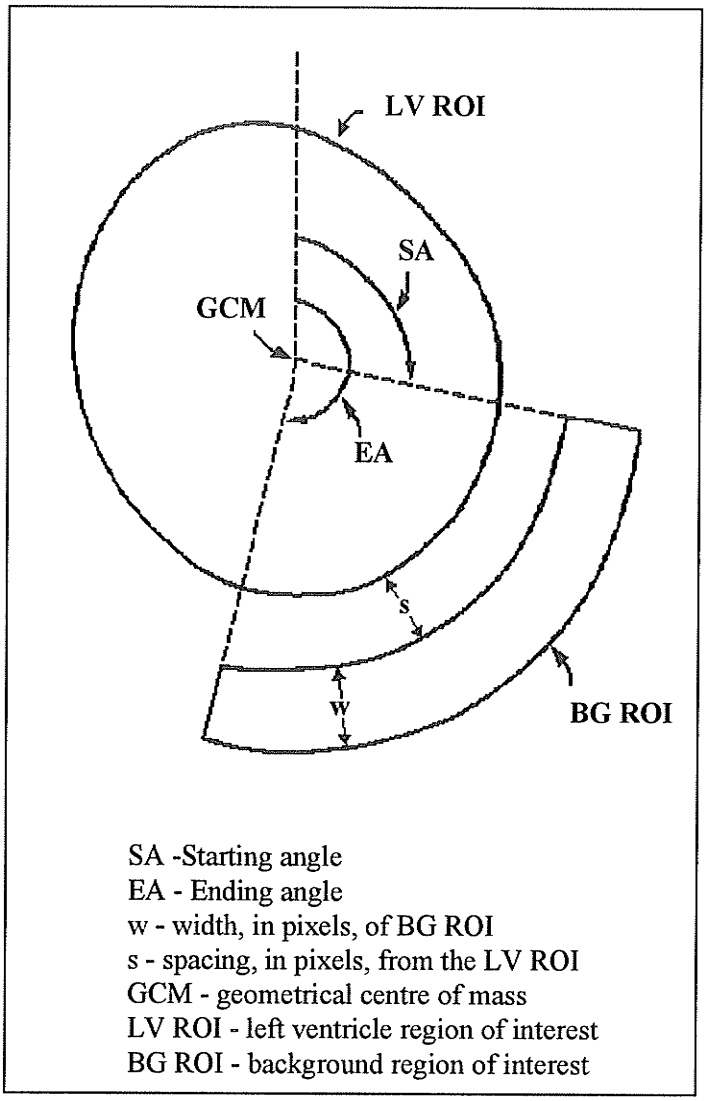

Figure 1.3: Parameters involved in background region of interest selection in manual method of ejection fraction calculation [adapted from APEX SP-1 Operation Manual].

1.2.4 Semi-Automated Method

The image set is smoothed both temporally and spatially, as in the manual technique. A master ROI is created which encompasses the left ventricle in all image frames. This ROI is defined by the software and is based on the phase image (a single image conveying the relative time of contraction of each pixel, mathematically defined to be the first harmonic resulting from Fourier analysis, as described in section 3.1.1), the amplitude image (a single image in which each pixel represents the maximum change in measured counts over the entire cardiac cycle), and the average grayscale image of the entire sequence of frames. The master ROI simply defines the image area to which the edge detection algorithm will be applied in every frame of the study. The user is given the opportunity to redraw this master ROI. An edge detector is then applied to the master ROI in each image frame, in order to create an LV boundary on each frame. The edge detection is based on a second derivative technique with predefined thresholds. The thresholds are defined for each of the eight main cardinal directions and applied to the second derivative information along ray traces outwards from the LV grayscale maximum, to generate LV edge points. The user may redraw the LV boundary in any of the image frames. A low pass filter is applied to the LV TAC to decrease noise. A background ROI is automatically created in the ES frame and consists of a crescent shaped region 3 pixels in width, 1 pixel outside the LV boundary, extending from 90 to 180 degrees relative to the LV centre. The user may redefine this background ROI. The background activity is subtracted in the same manner as in the manual method, and the

LV TAC analysed for ejection fraction. The analysis is printed out on film, and saved to disk.

1.2.5 Fully Automated Method

This technique is essentially the same as the semi-automated procedure, except that the user is not given opportunities to redefine the LV ROI's nor the background ROI. The software documentation recommends careful review of the results, and possible verification using the manual method. The fully automated technique is not currently used at the HSC for several reasons:

1) The sensitivity of the edge detection algorithm employed in the automated (and semi-automated) routine is very cumbersome to modify in situations where the automatically identified edges are in disagreement with the physician's estimate.

2) The correlation between the automated results and the previous method of EF measurement was measured at the time of installation of the current equipment and software. The automated results correlated poorly with the results of the previous method (relative to the manual analysis), and hence has been unused in favour of the manual analysis.

1.3 Fuzzy Clustering

1.3.1 Motivation for Using Fuzzy Set Theory

Fuzzy set theory is a generalization of abstract set theory. Since abstract set theory is simply a special case of fuzzy set theory any definition, theorem, proof, etc., of fuzzy set theory will always hold for abstract sets. Fuzzy set theory has a wider scope of applicability than abstract set theory because of this generalization, especially in solving problems requiring subjective evaluation (such as left ventricle boundary identification).

Inexactness may take several different forms: (1) generality: that a concept may apply in a variety of situations, (2) ambiguity: that a situation may be described by more than one distinguishable concept, and (3) vagueness: that boundaries are not defined precisely. The fuzzy set is a mathematical representation of all these forms of inexactness. Manifestations of inexactness that are contained in the nuclear medicine image set being analysed include low resolution, noise from scatter and background sources, relatively poor statistics, and overlapping of anatomical features (2-D view of a volume source). The resulting images are of generally poor resolution and contrast as compared with images from other modern modalities, with the anatomical features being blurred and indistinct. This high degree of inexactness which characterizes gated blood pool images make them an excellent candidate on which to apply fuzzy set theory. Furthermore, the physician makes several subjective decisions when analysing an image set for an ejection fraction. Thus, an analysis based on fuzzy set theory approach as opposed to abstract set theory seems most logical. Previous applications of fuzzy set theory in the medicine field are numerous [Adlassnig, 1986; Maiers, 1985; Tazaki, 1986; Zaifu, 1986].

1.3.2 Non-Mathematical Discussion of Fuzzy Clustering

Fuzzy classes of objects are often encountered in the real world (as opposed to an ideal mathematical construct). For example, A may be the set of beautiful women in a city W, or A may be the set of tall trees in city W. Traditionally, the grade of membership 1.00 is assigned to those objects that fully and completely belong to A, while 0.00 is assigned to objects which do not belong to A at all. This form of membership assignment presents problems when applied to the examples given above. How tall does a tree have to be to be classified as a 'tall tree', and similarily, how beautiful a woman to be classified as belonging to the set of 'beautiful woman'. This lack of a precisely defined criteria of membership is commonly encountered in the real physical world. In situations such as these, an object does not necessarily need to either belong or not belong to a class. There exists the possibility of assigning intermediate grades of membership. This is the concept of a fuzzy set, consisting of a class with a continuum of grades of membership. Applied to a single frame of a gated radionuclide ventriculography study, each pixel may be assigned a membership grade determining its association with a particular anatomical feature. For instance, the membership grades for a cross-section of pixel intensities in such an image may be thought of as belonging to the right ventricle, left ventricle, septum, or descending aorta, as depicted in Figure 1.4. The fuzzy set memberships consist of smoothly varying functions (in this case gaussian form was chosen for illustrative purposes), while the non-fuzzy set memberships are composed of step functions.

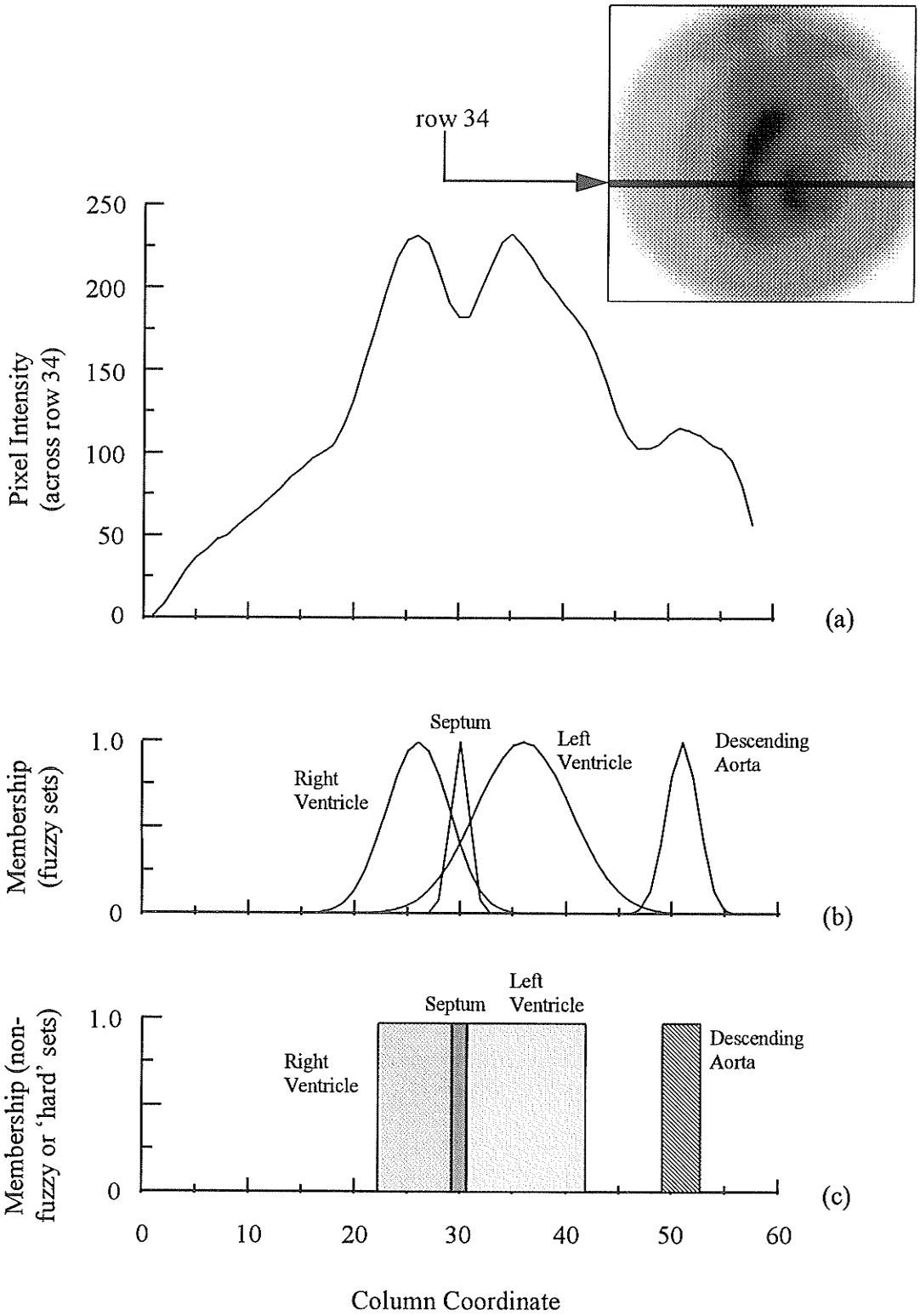

Figure 1.4: (a) Profile of pixel intensity across row 34 of end-diastolic image frame, (b) possible fuzzy memberships of pixels according to anatomical representation, and (c) possible non-fuzzy or 'hard' memberships.

Classification is the process of assigning an item (or observation) to its proper place; the problem of cluster analysis is frequently stated as one of finding the 'natural groups' within a set of data. The essence of cluster analysis may be viewed as identifying homogeneous and well-separated structures within a given data set (Kandel, 1982). Applied to the problem at hand, this could translate into the identification of a set of pixels representative of the left ventricle, where all the member pixels possess homogeneous properties (such as similar phase and intensity), yet significantly different properties when compared to other groups of pixels such as those belonging to the right ventricle, descending aorta, or background.

Most cluster analysis methods require some measure of similarity to be defined for every pairwise combination of the data to be clustered. When clustering data, the proximity of individual data points is usually expressed as a distance. This implies that clusters are generally shaped in a spherical manner.

An object is characterized by assigning to it the values of a finite set of parameters considered relevant to the object (ie. *features* of the object or data set). These input features are generally defined by the data acquired by a sensory device. In this case, the sensory device is a standard nuclear medicine gamma camera. Some features used in applying fuzzy clustering in this work include the first harmonic phase (section 3.1.1), isolation value (section 3.1.2), grayscale intensity (section 3.4), x-, and y-coordinates (sections 3.1 & 3.4).

It should be emphasized that cluster analysis is a device for suggesting hypotheses. The classification of data, or variables obtained from a cluster analysis

procedure, has no inherent validity. The worth of a particular classification and its underlying explanatory structure is to be justified by its consistency with known facts.

It is hoped that this non-mathematical discussion of fuzzy set theory and fuzzy clustering has been useful in quickly illustrating some of the main ideas and principles involved in this broad field. The following few sections will delve more deeply into the mathematics of fuzzy clustering, and eventually present the fuzzy clustering algorithm which has been employed in this work.

1.3.3 Fuzzy Set Theory

The theory of fuzzy sets deals with some subset C of the universe (or collection of objects) Y, where the transition between no membership and full membership in the subset is gradual and continuous, rather than a discrete change. The fuzzy subset C has no well defined boundaries while the universe Y covers a definite range of objects. The membership grade of 1 is assigned to those objects which fully and completely belong to C, while 0 is assigned to objects which do not belong to C; the more representative of C an object is, the closer to 1 is its membership grade. In nonfuzzy (or abstract) set theory, membership is either 0 or 1, with no intermediate classifications.

If $Y = \{y\}$ denotes a collection of objects, then a fuzzy set C in Y is a set of ordered pairs defined as:

$$C = \{(y, u_C(y))\}, \qquad y \in Y, \quad u_C \in [0,1]$$

where u_C is the grade of membership of y in C. This membership grade lies between 0 and 1 as discussed previously. The grades of membership reflect an ordering of the

objects in the universe, produced by the association of attributes of C. The membership grade $u_C(y)$ of an object y in C can be alternatively interpreted as the degree of compatibility of the attributes associated with C and the object y.

1.3.4 Cluster Analysis

The cluster analysis problem is generally stated as one of finding the 'natural groups' within a data set. The objective is to sort the data set into categories (or clusters) such that the degree of association is high among members of the same cluster, but low between members of different clusters. In other words, homogenous and well-separated clusters are desired.

Generally cluster analysis requires some measure of similarity to be defined for every pairwise combination of data points to be clustered. A common similarity measure is the proximity of individual data points, usually expressed as a distance. Clusters are defined through the application of the similarity measure (also known as the clustering criterion). Many different similarity measures for clustering have been proposed and used, but the most popular and well studied method to date is the generalized least-squared errors criterion. This criterion is used in the present analysis, and will be described in detail in a following section.

Outlier data points ideally fall into a category reserved for 'unclassifiable' points. Conventional methods of clustering (based on abstract set theory) possess no natural mechanism for assimilating the effects of indistinctive or deviant data. However, fuzzy set theory alters the basic axioms underlying clustering in order to accommodate this requirement. In fuzzy clustering, a data point may belong entirely to a single cluster, but generally retains partial membership in several clusters thereby removing (or at least reducing) the effect of a potential outlier.

An example adapted from Bezdek (1981) illustrates how a simple array of geometric points is assigned memberships within two clusters. This is the classic Butterfly example, and is illustrated in Figure 1.5, and Table 1.2. The set of input vectors used by the fuzzy clustering routine simply consists of the x- and y-coordinate data of each point. The clustering routine has been set to find two clusters within the given set of data. Each data point has partial membership to both clusters. Due to the mirror symmetry about the eighth data point, the membership functions for the two clusters are also symmetric about this point, as observed in Table 1.2.

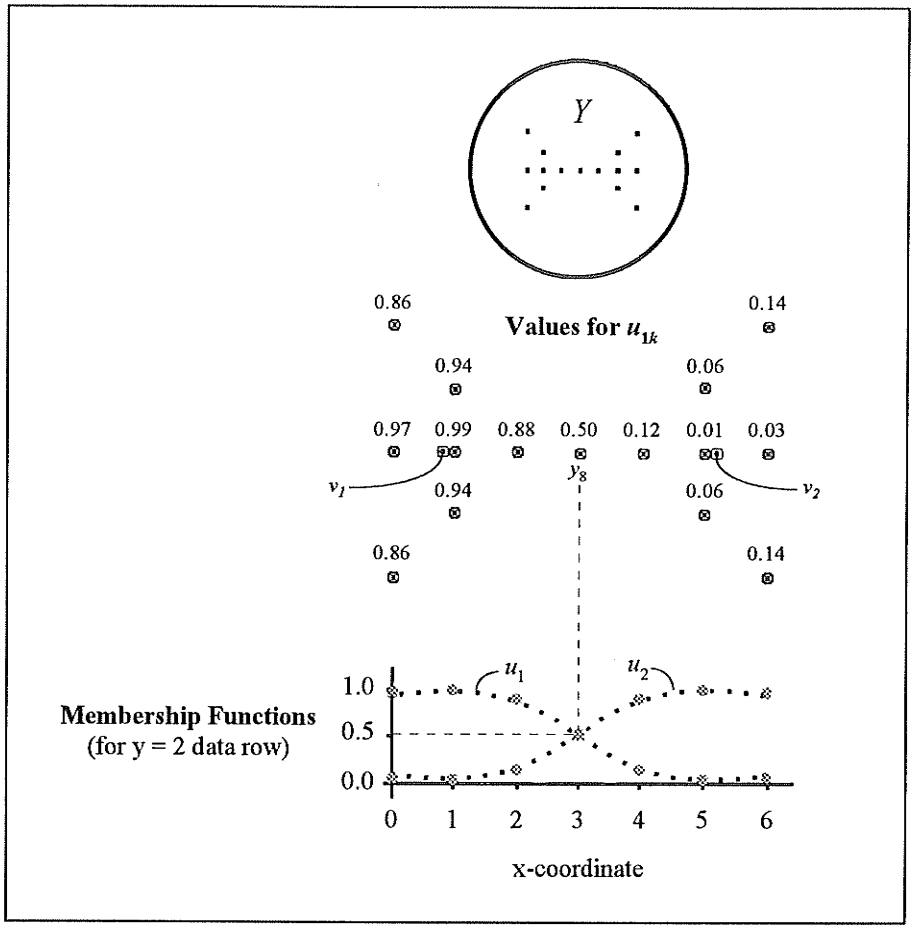

Figure 1.5: Illustration of fuzzy clustering (set to identify two clusters) applied to a simple data set of Cartesian points [adapted from Bezdek, 1981].

Sample	Input Data	Membership Functions	
k	y_k	u_{1k}	u_{2k}
1	(0, 0)	0.86	0.14
2	(0, 2)	0.97	0.03
3	(0, 4)	0.86	0.14
4	(1, 1)	0.94	0.06
5	(1, 2)	0.99	0.01
6	(1, 3)	0.94	0.06
7	(2, 2)	0.88	0.12
8	(3, 2)	0.50	0.50
9	(4, 2)	0.12	0.88
10	(5, 1)	0.06	0.94
11	(5, 2)	0.01	0.99
12	(5, 3)	0.06	0.94
13	(6, 0)	0.14	0.86
14	(6, 2)	0.03	0.97
15	(6, 4)	0.14	0.86

Table 1.2: Cartesian data points input into fuzzy clustering routine (identifying two clusters) and resulting membership functions.

1.3.5 Fuzzy *c*-Means Algorithm

In this section, the mathematical basis for the fuzzy *c*-means algorithm will be developed. Due to the abstract nature of the mathematics involved, analogies to the Butterfly example from the previous section will be drawn at every opportunity. Once the background description is complete, the steps of the fuzzy *c*-means algorithm will be described. The algorithm is aptly named (ie. '*c*-means') since the calculation of the mean data value of each of *c* clusters is required for each iteration of the algorithm.

Let $Y = \{y_1, y_2, ..., y_N\}$ be a sample of N observations in $\mathbf{R}^n$ (n-dimensional Euclidean space), where y_k is the k-th feature vector and y_{kj} the j-th feature of y_k. A feature vector is composed of all the information or 'features' associated with each given observation in Y. In the adapted example in the previous section, $k = 1, ..., 15$ (number of data points), $j = 1, 2$ (the two features are the x- and y-coordinate data), and Y = the entire set of data points. Define an integer c, where $2 \le c < n$, as the number of clusters (or partitions) within a set of data Y. The c-partition of Y is a c-tuple $(Y_1, Y_2, ..., Y_c)$ of subsets of Y satisfying:

(a) $u_i(y_k) \equiv u_{ik} \in [0,1]$ - membership of each feature vector lies in the interval [0, 1]

(b) $\sum_{k=1}^{N} u_{ik} > 0$ for all i - sum of memberships in a certain cluster c, must be greater than 0

(c) $\sum_{i=1}^{c} u_{ik} = 1$ for all k - sum of a feature vectors membership in all clusters must be 1

The symbol U represents a real $c \times N$ matrix ($U = [u_{ik}]$), representing the partition $\{Y_i\}$ and i is the partition index number (ie. cluster number). U is referred to as a fuzzy c-partition

of Y when the elements of U are real numbers in the unit interval [0,1] which continue to satisfy conditions (b) and (c) above. Examining our Butterfly example, we see that U is a 2×15 matrix since there are 2 clusters specified and 15 feature vectors (ie. data points) used. Note that these membership functions satisfy conditions (a) - (c) above (on page 24). Condition (a) is satisfied since all u_{1k} and u_{2k} lie in the interval [0,1]. Condition (b) is satisfied since both the sum of u_{1k} over all k, and the sum of u_{2k} over all k (that is, summing the membership functions for a particular cluster over all data 15 data points) is greater than zero. Condition (c) is satisfied since the sum $(u_{1k} + u_{2k})$ equals 1.00 for each feature vector (that is, for each of the 15 data points).

Several clustering criteria have been suggested for identifying optimal fuzzy c-partitions of Y. In general, this involves a pair-wise comparison of feature vectors to cluster centres as calculated via a centre-of-mass approach . As mentioned earlier, the most popular and best studied criterion is associated with the generalized least squares functional:

$$J_m(U,v) = \sum_{k=1}^{N}\sum_{i=1}^{c}(u_{ik})^m \left\| y_k - v_i \right\|_A^2 \qquad (1.3)$$

where $Y = \{ y_1, y_2, ..., y_N \} \subset \mathbf{R}^n$ = the data to be clustered,

c = number of clusters in Y; $2 \le c < n$,

m = weighting exponent; $1 \le m < \infty$; see description below,

U = fuzzy c-partition of Y; $U \in M_{fc}$; M_{fc} = the set of all fuzzy c-partitions of Y,

$v = (v_1, v_2, ..., v_c)$ = vectors of centres,

$v_i = (v_{i1}, v_{i2}, ..., v_{in})$ = centre of cluster i,

$\| \ \|_A$ = induced A-norm on $\mathbf{R}^n$,

A = positive definite $(n \times n)$ weight matrix, see description below.

In the above equation, the squared distance between y_k and v_i is calculated in the A-norm as:

$$d_{ik}^2 = \|y_k - v_i\|_A^2 = (y_k - v_i)^T A(y_k - v_i)$$

Each squared error is weighted by the mth power of y_k's membership in cluster i $[(u_{ik})^m]$. The set of vectors $\{v_i\}$ are the cluster centres, essentially the centres of mass of the partitioning subsets, and may be calculated by:

$$v_i = \frac{\sum_{k=1}^{N} (u_{ik})^m y_k}{\sum_{k=1}^{N} (u_{ik})^m} \qquad (1.4)$$

In the Butterfly example, the final cluster centres are illustrated in Figure 1.4, with the exact values of:

$$v_1 = (0.85, 2.00) \qquad \text{and} \qquad v_2 = (5.14, 2.00)$$

These values satisfy the centre of mass equation (1.4 above) for the membership functions given in Table 1.2.

The elements of the membership function are determined by (Bezdek, 1984):

$$u_{ik} = \left(\sum_{j=1}^{c} \left(\frac{d_{ik}}{d_{jk}} \right)^{\frac{2}{(m-1)}} \right)^{-1} \qquad (1.5)$$

Other variables in J_m which require further explanation are the fuzzy weighting exponent m and weighting matrix A.

The exponent m controls the relative weights placed on each of the squared errors d_{ik}^2. As $m \rightarrow 1$, the c-partitions which minimize J_m become increasingly hard. By increasingly hard, it is meant the clustering approaches that which would occur if

classical set theory were employed. Considering $m = 1$, it may be shown that J_m minimizes only at hard c-partitions, and the corresponding v_is are simply the geometric centroids of the Y_is. As $m \to \infty$, the membership of the optimal U matrix for J_m is degraded towards the fuzziest state, where each element approaches a value of $(1/c)$. Holding all other parameters constant, each choice of m defines one fuzzy c-means algorithm. There exists no theoretical method of choosing an optimal m, but Bezdek (1984) suggests the best strategy is an optimization approach through processing of the experimental data. This is incorporated in the overall parameter optimisation as described in section 4.1. The Butterfly example employed a value of $m = 2.00$, which is similar to that used in the fuzzy clustering application to gated radionuclide ventriculography.

The weight matrix A controls the shape which optimal clusters assume in $\mathbf{R}^n$. While an infinite number of A-norms is available for use, the choice of $A = I$ (the identity matrix) directs J_m to identify hyperspherical clusters. Since left ventricle boundary shape in the LAO view of a healthy subject is circular or elliptical, this decision is justified. Geometrically, we say the choice of matrix A induces a topology upon the data set (Bezdek, 1981). The Butterfly example also defined $A = I$, thus inclining spherically shaped clusters to be identified. This effect can be readily observed since only geometric data (x- and y-coordinates) were used as input. Thus, the membership function values for data points around the cluster centre generally vary in a spherically symmetric manner (or in this case, a circularly symmetric manner due to the data set being two dimensional). Examining the membership values of u_{1k} in relation to v_1 in Figure 1.4, this effect is apparent.

Explanation of the basic elements of J_m in equation 1.3 are:

d_{ik}^2 = squared A-distance from point y_k to centre of mass v_i.

$(u_{ik})^m d_{ik}^2$ =squared A-error obtained when representing y_k by v_i weighted by a power of the membership of y_k in cluster i.

$\sum_{i=1}^{c}(u_{ik})^m d_{ik}^2$ =sum of squared A-errors due to y_k's partial replacement by all c of the centres $\{v_i\}$.

$\sum_{k=1}^{N}\sum_{i=1}^{c}(u_{ik})^m d_{ik}^2$ =overall weighted sum of generalized A-errors due to replacing Y by v.

With a discussion of relevant background material complete, the fuzzy c-means algorithm may now be presented as a four step process.

(1) Fix c, m, A, ε_L. Initialize membership matrix $U^{(0)}$ randomly. Then at step l, $l = 0$, 1, 2, ...,.

(2) Calculate the c fuzzy cluster centres $\{v_i^{(l)}\}$ using equation (1.4), and $U^{(l)}$.

(3) Compute an updated membership matrix $U^{(l)}$ using equation (1.5) and $\{v_i^{(l)}\}$. This is equivalent to constructing a new set of c partitions.

(4) Compare $U^{(l)}$ to $U^{(l+1)}$ in a convenient matrix norm; if $\| U^{(l+1)} - U^{(l)} \| \leq \varepsilon_L$ stop, otherwise return to (2).

Note the parameter ε_L has been introduced in the algorithm above. This is a threshold value set to control the convergence of the calculation. The theoretical convergence of the sequence $\{U^{(l)}, v^{(l)}, l = 0, 1, 2, ...\}$ generated by this algorithm has been previously studied (Bezdek, 1981), and convergence is generally achieved within 10-25 iterations.

Once convergence is attained, the data points are classified by their membership functions as being a member of cluster i, a non-member of cluster i, or a non-classifiable point (a non-member of all clusters, i = 1 through c). The divisions are based on

properties of the generalized least-squared functional. The lower boundary below which a data point is definitely not a member of cluster i, is defined as $(1/c)$. This choice is based on the fact that a properly convergent set of u_{ik}'s for J_m approach $(1/c)$ as $m \rightarrow \infty$ (Bezdek, 1984). Consequently, this implies that membership in the fuzziest state reduces to $(1/c)$. The upper boundary, above which a point is definitely a member of cluster i, is defined as $((1+c)/2c)$. This boundary is chosen because it lies exactly half the distance between $(1/c)$ and 1. Considering the set of conditions (a) - (c), we see this choice ensures that simultaneous full membership of a single data point to more than one cluster is not possible (a logical restriction).

References

APEX version F1 Application Manual. Ed. Anonymous. Elscint Limited, 1986. CEF-i-CEF-77.

Cardiology: an illustrated text/reference. Ed. Chatterjee, K., M. D. Cheitlin, J. Karliner, et al. Philadelphia: J.B. Lippincott Company, 1991. 1.2-1.18.

Adlassnig, K.P. "Fuzzy Set Theory in Medical Diagnosis." IEEE Transactions on Systems, Man, and Cybernetics 16 (2) (1986): 260-265.

Almasi, J.J., E.G. DePuey, R.L. Eisner, et al. "Totally Automated Computer Processing of Gated Cardiac Blood Pool Studies." Journal of Nuclear Medicine 23 (5) (1982): P24(Abstract)

Bezdek, J.C., R. Ehrlich, and W. Full. "FCM: The Fuzzy c-Means Clustering Algorithm." Computers and Geosciences 10 (2-3) (1984): 191-203.

Bezdek, J. C. Pattern Recognition with Fuzzy Objective Function Algorithms. New York: Plenum Press, 1981. 1-256.

Burow, R.D., H.W. Strauss, R. Singleton, et al. "Analysis of Left Ventricular Function from Multiple Gated Acquisition Cardiac Blood Pool Imaging (Comparison to Contrast Angiography)." Circulation 56 (6) (1977): 1024-1028.

Chang, W., R.E. Henkin, D.J. Hale, et al. "Methods for Detection of Left Ventricular Edges." Seminars in Nuclear Medicine 10 (1) (1980): 39-53.

Christian, P.E., C.A. Notrmann, and A. Taylor. "Comparison of Fully Automated and Manual Ejection Fraction Calculations: Validation and Pitfalls." Journal of Nuclear Medicine 26 (1985): 775-782.

Douglass, K.H., H.N. Wagner,Jr., P.O. Alderson, et al. "Characteristics of Left Ventricular Time-Activity Curves in Normal Volunteers." Journal of Nuclear Medicine 19 (6) (1978): 670(Abstract)

Goris, M. L. "Non-Interactive Identification of the Left Ventricular Area." Nuclear Cardiology: Selected Computer Aspects. Ed. Anonymous. New York, NY: The Society of Nuclear Medicine, Inc., 1978. 139-145.

Green, M.V., W.R. Brody, M.A. Douglas, et al. "Ejection Fraction by Count Rate from Gated Images." Journal of Nuclear Medicine 19 (8) (1978): 880-883.

Jouan, A., J. Verdenet, J.C. Cardot, et al. "Automated Detection of the Left Ventricular Region of Interest by MEans of the Extraction of Typical Behaviors in Cardiac Radionuclide Angiographies." IEEE Transactions on Medical Imaging 9 (1) (1990): 5-10.

Kandel, A. Fuzzy Techniques in Pattern Recognition. New York: John Wiley & Sons, Inc., 1982. 1-356.

Links, J.M., L.C. Becker, J.G. Shindledecker, et al. "Measurement of Absolute Left Ventricular Volume From Gated Blood Pool Studies." Circulation 65 (1) (1982): 82-91.

MacIntyre, W.J., B. Sufka, R.T. Go, et al. "Comparison of Edge Detection and Ejection Fraction Algorithms by a Computer Simulated Cardiac Model." Journal of Nuclear Medicine 23 (5) (1982): P23(Abstract)

Maiers, J.E. "Fuzzy Set Theory and Medicine: The First Twenty Years and Beyond." IEEE Proceedings (1985): 325-329.

Okada, R.D., H.D. Kirshenbaum, F.G. Kushner, et al. "Observer Variance in the Qualitative Evaluation of Left Ventricular Wall Motion and the Quantitation of Left Ventricular Ejection Fraction Using Rest and Exercise Multigated Blood Pool Imaging." Circulation 61 (1) (1980): 128-136.

Palmer, E. L., J. A. Scott, and H. W. Strauss. Practical Nuclear Medicine. Philidelphia: W.B. Saunders Company, 1992. 1-399.

Reiber, J.H.C. "Quantitative analysis of left ventricular function from equilibrium gated blood pool scintigrams: an overview of computer methods." European Journal of Nuclear Medicine 10 (1985): 97-110.

Reiber, J.H.C., S.P. Lie, M.L. Simoons, et al. "Clinical Validation of Fully Automated Computation of Ejection Fraction from Gated Equilibrium Blood-Pool Scintigrams." Journal of Nuclear Medicine 24 (12) (1983): 1099-1107.

Slutsky, R., M. Pfisterer, J. Verba, et al. "Influence of Different Background and Left-Ventricular Assignments on the Ejection Fraction in Equilibrium Radionuclide Angiography." Radiology 135 (June) (1980): 725-730.

Tazaki, E., Y. Hayashi, K. Yoshida, et al. "Development of Automated Health Testing and Services System via Fuzzy Reasoning." IEEE Proceedings (1986): 342-346.

Xie, X.L. and G. Beni. "A Validity Measure for Fuzzy Clustering." IEEE Transactions on Pattern Analysis and Machine Intelligence 13 (8) (1991): 841-847.

Zaifu, S., S. Hongyuan, L. Yanjie, et al. "Application of Fuzzy Set Theory in Health Care System." Applications of Fuzzy Set Theory in Human Factors. Ed. Karwowski, W. and A. Mital. Amsterdam, Netherlands: Elsevier Science Publishers B.V., 1986. 379-391.

Chapter Two: UNCERTAINTY IN EJECTION FRACTION MEASUREMENT

2.0 Introduction

The measurement of ejection fraction through equilibrium gated blood pool imaging may be affected by several sources of uncertainty. These sources can be categorized into three main groups: 1) patient factors, 2) acquisition procedure conditions, and 3) analysis techniques.

Patient factors are those dependent upon the physiological condition and anatomical structure of the patient being imaged. Uncertainties due to acquisition procedure conditions include any error introduced by the equipment used to gather the images, or by the physical nature of the pharmaceuticals involved. Analysis techniques encompass all analytic methods applied to the extraction of EF measurements from gated blood pool images, excluding the parameter optimisation of our developed technique which has been described in section 4.1.

In this chapter, all factors introducing uncertainty into the measurement of EF via equilibrium gated blood pool imaging will be discussed, within the three main categories as mentioned above. Finally, the effect of these uncertainties on EF measurement will be considered.

2.1 Ejection Fraction Uncertainties

2.1.1 Physiological Uncertainties

2.1.1.1 Phase Variations

Due to beat-to-beat variation in the shape of the TAC, the resulting superposition of several hundred of such curves will result in an overall TAC which does not accurately represent LV volume variations. For example, if two LV volume curves are summed, each possessing identical EF and end-diastolic volume but with different systolic time periods, the resultant curve will demonstrate a reduced EF. Since patients exhibit fluctuations in their heart rate, even in a 'steady' state, it is reasonable to assume that most LV volume curves will vary in length with each beat. In a study performed by Green *et.al.* (1978) to investigate the effects of this variation of phase on calculated ejection fraction, it was found that in a statistical sense, the beat length fluctuations did not introduce a significant error. However, the possiblity still exists that these fluctuations may introduce significant errors into the measured EF in patients with extremely low heart rates, due to the distortion introduced into the TAC of such patients.

2.1.1.2 Attenuation

In addition to the effects of blood volume self-attenuation on EF as discussed in section 4.2, physical variation within the patient will also contribute uncertainty to any method attempting to correct for attenuation. The variety of tissue types, volumes, and

geometrical configuration of these different tissues contribute to form a source of uncertainty in any estimate of attenuation. Tissue involved in photon attenuation will possess widely varying attenuation coefficients, and may include lung [3.874 m^{-1}], skin [16.241 m^{-1}], heart [15.645 m^{-1}], fat [13.800 m^{-1}], blood [15.794 m^{-1}], and bone [48.375 m^{-1}] with attenuation coefficients enclosed in square brackets (ICRU 44).

2.1.1.3 Post Meal Effects

The effect of a standardized meal on LV EF using gated blood pool imaging has been studied by Brown *et.al.* (1983). LV EF was determined in a fasting state, as well as 15, 30, and 45 minutes after a meal. It was concluded that significant increases in EF (above normal EF variation) may occur after meals in normal patients and those with moderate LV dysfunction, but not severe LV dysfunction. Brown suggested that the mechanism by which this occurs may be a decrease in systematic vascular resistance resulting in LV unloading. Furthermore in patients with more severe LV dysfunction, it was speculated that chronically increased sympathetic nervous system tone may result in blunting of the usual physiologic responses to a meal, and these patients are less sensitive to the mild degree of afterload reduction induced by food intake due to continued high preload conditions. Therefore equilibrium radionuclide ventriculography studies which are not standardized for patients' mealtimes may introduce an important unmeasured variable that will affect the validity of data in serial studies of left ventricular function.

2.1.1.4 Patients With Aneurysm

Cases of LV aneurysm (distended blood vessel or heart walls) are fairly common, with an incidence estimated in the range 4-30% (Onik *et.al.*, 1980). In gated blood pool studies, they are generally identified as a late-contracting zone in the left ventricle region. To accurately calculate the EF, the activity contribution from this region must be accounted for (Boudraa *et.al.*, 1993). Schicha *et.al.* (1985) demonstrated that gated blood pool studies in cases of anterior LV aneurysm underestimated the LV EF by a mean of 6.2% as compared to biplane cineangiography. Individual cases were underestimated by as much as a factor of two. It is thought that due to the differences in photon attenuation, the proportion of smaller cyclic changes of the count rate originating in the blood within the aneurysm is overestimated, while that of the blood in the posterior portion of the LV is underestimated. Consequently, LV EF of patients with aneurysm of the anterior wall is underestimated.

2.1.1.5 Normal Variation

The intrinsic variability and accuracy of calculating LV EF via gated blood pool studies may be evaluated by performing serial studies on patients. Wackers *et.al.* (1979) found that the mean variability of absolute EF for repeat studies in normal patients was significantly greater than in abnormal patients. This differential variability should be considered in interpreting sequential changes in LV EF. It was concluded that in order to be attributed to nonrandom physiological alterations, the absolute EF change (ie. in absolute EF units) should be 10% or more in normal patients and 5% or more in

abnormal patients. This difference may be a reflection of a pathophysiologic phenomenon. In patients with normal LV performance, there is a greater ventricular reserve and hence an increased chance of responding to a variety of stimuli with augmentation of cardiac pump function.

2.1.2 Uncertainties in Acquistion Protocol/Equipment

2.1.2.1 Nonuniformity of Gamma Camera

Nonuniformity of the gamma camera is the result of both variations in sensitvity across the camera face, and spatial distortions. A two part study was performed by Busemann-Sokole *et.al.* (1985) on a cardiac phantom to study the impact of a nonuniform camera upon ejection fraction. The first part of the study investigated the effect on ejection fraction values when camera uniformity was degraded by improper analyzer window positioning. The pulse height analyser allows the operator to select only the signals from those gamma rays in which the photon energy lies within a certain range of values (ie. a 'window' of values). When the pulse height analyser window was improperly set (by varying levels from 5.2% to 22.7% in terms of differential uniformity), the EF displayed a small variation, within +/- 3% of the expected correctly collected EF. The nonuniformity obtained was analysed by application of the NEMA (National Electrical Manufacturers Association) standards protocol in order to obtain parameters for the differential uniformity present.

The second part of the study determined the effect on ejection fraction values of a nonfunctioning photomultiplier tube. When a selected photomultiplier tube was successively detuned by altering the tube gain, variation in EF became noticeable, especially at low nominal EF values. It was concluded that a reasonable degree of confidence (maximum EF deviation of 5%) may be placed in ejection fraction measurements even when differential camera nonuniformity is as much as 10%.

2.1.2.2 Gating Delays

Most electrocardiograph gating devices have an intrinsic delay between the time that the R-wave is sensed and the time the gating signal is sent (Powers, *et.al*, 1982). The effects of gating delays between 0 and 50 msec on the EF estimate were simulated, while actual measured delay times for clinically attainable heart rates possessed a much smaller range, varying between 0 and 9 msec (Powers, *et.al.*, 1982). Delay between the actual electrical event and its detection by the computer will result in a shift of the perceived R-wave from its actual location. If no fitting of the time activity curve is performed, the maximum counts in the LV will then be artificially decreased (since the first data frame counts will be reduced due to missing the acquisition of that data), resulting in a lower than expected EF. This results from the software restricting the search for a count maximum to the first two thirds of the TAC. Intuitively, the magnitude of the EF underestimation depends directly on the speed of the left ventricle emptying. Powers *et.al.*, 1982, determined that gating delay effects will be most pronounced at higher heart

rates, and that the greatest artificial EF reduction will occur in patients with normal (as opposed to poor) ventricular function.

2.1.2.3 Frame Rate Requirements

The ejection fraction may be influenced by the sampling rate and sampling period employed when the TAC data are collected (Bacharach *et.al.*, 1979; Hamilton *et.al.*, 1978). Hamilton *et.al.* (1978) examined rest-exercise TAC's of two patients using modern sampling theory. Fourier analyis of the TAC's revealed that 95% of the frequency content lies below 7 Hz for a high ejection fraction and heart rate, and below 4.5 Hz for a normal EF and heart rate. The Nyquist sampling criterion states that a signal must be sampled at twice the frequency (or more) for an accurate reconstruction. Thus, sampling rates of 14 Hz and 9 Hz for the high and normal heart rates respectively, are required. A sampling rate of 14 Hz corresponds to a frame rate of 10.5 Hz for a patient with a heart rate of 80 bpm. At frame rates above the minimum for correct reconstruction, calculated EF will decrease slightly as frame rate is reduced towards the minimum, due to loss of high frequency response caused by the lengthening of the sample period. Hamilton suggests using a frame rate about 25 Hz, since the underestimation of EF due to aliasing errors will be negligible (due to this rate satisfying the Nyquist sampling criterion).

In a study of 32 patients, Bacharach *et.al.* (1979) duplicated the effects of performing a study with decreasing temporal resolution. This was done by condensing the original TAC data collected at 10 ms/point into TAC's representing 20, 30, 40 and 50

ms/point by adding consecutive 10 ms/point data together. It was observed that EF did not vary significantly for time frames up to 50 ms. The conclusion indicated that frame lengths of 50 ms (corresponding to a frame rate of 20 Hz) should be sufficient to optimally reduce errors in calculated EF.

At HSC, individual gated blood pool studies are not performed at the same frame rate, but rather the patient's cardiac cycle is divided into a constant number of frames. The number of frames used is set through software, with a default value of 24 (resulting in a sampling frequency of 32 Hz for a patient with a heart rate of 80 bpm). As the heart rate of the patient decreases, each frame will represent a longer and longer time period, while the frequency content of the TAC is also decreasing (Hamilton *et.al.*, 1978). These two effects (increasing frame time length vs. decreasing frequency content) are offsetting, hence by dividing every cardiac cycle into 24 frames as opposed to simply setting a constant frame rate, the TAC should be accurately reconstructed for all heart rates.

As mentioned previously (section 1.1.3.6), the 24 image frames are compressed into 16 frames for display and storage purposes. Linear interpolation is applied to the 24 frame processed data set to construct the non-coincident (in time) images of the 16 frame data set. This compression of data results in an increase in the minimum heart rate which can be reconstructed without worry of possible undersampling errors (as discussed in section 1.1.3.3). The minimum heart rate for a 16 frame study to keep time intervals for each frame below 0.050 seconds is 75 bpm. Data collected at heart rates below this may cause errors in the TAC fit due to undersampling. In the 10 test group, only two patients

exhibited heart rates below 75 bpm at the time of image acquisition. Both the manual and semi-automated analysis of the TAC revealed that in these two cases, the TAC did not exhibit a steep fall off at ES. That is, the TAC curve did not drop from ED volume to ES volume within a 0.050 second time interval (if this did happen, the TAC would be improperly represented by the 16 frame compressed data). Therefore, the compression of 24 frames into 16 frames does not significantly affect the results of the fuzzy technique of estimating EF, for the 10 test studies chosen. Future analyses may avoid this potential problem altogether by performing the analysis on the original 24 frame data.

2.1.2.4 Decay of Activity

The duration of imaging acquisition for the best septal view of the heart is 600 seconds (10 min) using the HSC protocol. This is generally the procedural time interval allowed by most centres to achieve an image with good statistics, while minimizing patient discomfort. The decay of the source within the patient will result in the LV volume curves being composed of fewer and fewer counts as time elapses. The EF may remain the same, but the amplitude will decay at close to the same rate as the radioisotope (not exactly the same rate, due to simultaneous biological removal of the Tc^{99m}). If one calculates the percentage radioactive decay the source suffers during the imaging time interval [$\frac{I}{I_0} = e^{-0.693(t/t_{half-life})}$] using a $t_{half\text{-}life}$ of 360 minutes for Tc^{99m}, the signal intensity will decay by ~1.9 %.

However, if it is assumed that the shape of the LV volume curve does not vary over the image acquisition period, the effect of this amplitude decay will not be observed in the calculated EF. This is a result of the nature of the EF parameter (a ratio of heights on the TAC), and the fact that when curves of identical shape but varying amplitude are averaged together, the shape is preserved. Hence, relative heights (such as the EF) are also preserved.

2.1.3 Uncertainties in Analysis

2.1.3.1 Fourier Curve Fitting

The LV TAC may be fitted with a truncated Fourier series in order to improve statistical precision. Other methods of TAC fitting such as third degree polynomials have been explored, but the Fourier series approximation has been shown to be superior (Zatta, 1985). The EF parameter may then be calculated from the smooth Fourier fit, as opposed to the 'noisy' original TAC. Much work has been performed to find an optimal number of harmonics to fit TAC's (Bacharach, 1983; Halama, 1983; Mukai, 1983). Two sources of error, both dependent on the number of harmonics used in the fit, influence this calculation. First, if the image has poor statistics the truncated Fourier series may not adequately describe the shape of the TAC, due to a large number of harmonics being required for a good reconstruction. Second, due to the noise caused by counting fluctuations, TAC's acquired from the same subject under identical circumstances will fluctuate, thus causing the Fourier fitted curves to fluctuate. Since these two error

sources decrease and increase, respectively, with the number of harmonics used in the Fourier fit, a harmonic which minimizes both effects is suggested (Bacharach, 1983).

Bacharach (1983) found that for the EF parameter, two harmonics are optimum over a wide range of signal-to-noise ratios. For TAC's with large fluctuations (due to counting statistics), increased error is introduced by fitting with fewer than or more than two harmonics. With TAC's containing a greater number of counts, increasing the number of harmonics above two changes the total error only negligibly.

For these reasons, only two harmonics are used in fitting the TAC resulting from the fuzzy clustering LV identification.

2.1.3.2 Fixed vs. Variable LV ROI

A variable LV ROI is an ROI whose boundary changes between end-diastolic and end-systolic image frames. A fixed LV ROI is defined by a single contour drawn in the end-diastolic frame and applied to all other frames of the image. It has been demonstrated (Sorensen *et.al.*, 1979, 1981, Burow *et.al.*, 1977) that a fixed LV ROI, when compared with a variable LV ROI, does not correlate as well with angiography results. Sorenson (1979) and Burow (1977), performed both gated radionuclide equilibrium studies and conventional contrast angiography (an invasive method of finding EF) on patients, thus a 'gold standard' was available to which the radionuclide equilibrium studies could be compared. Results indicated that the fixed LV ROI method of analysing the radionuclide equilibrium studies significantly underestimated the EF, while the varying LV ROI method gave an improved correlation and very little EF

underestimation (compared to contrast angiography data). Sorenson (1979) explained this phenomenon in the following manner. An LV ROI defined at end-diastole and remaining fixed during systole will record counts which do not originate from the LV during systole, and the end-systolic count rate would be overestimated. This overestimation at end-systole would result in a reduction of the calculated EF. Thus, a varying LV ROI method has been incorporated into the fuzzy technique.

2.1.3.3 Algorithmic Dependence

There are many nuclear medicine computer systems available for performing and analysing gated blood pool studies, and the different manufacturerers will employ various approaches to this end. Chang *et.al.* (1980) present an overview of left ventricular edge detection techniques, while Reiber (1985) offers an examination of computer methods available for quantitative analysis of left ventricular function from equilibrium gated blood pool scans. A comparison of EF results between computer systems was performed by Makler *et.al.* (1985). That experiment involved the use of a cardiac phantom to provide as closely identical images as possible to the various hospitals concerned. Their results suggested that different computer systems yielded somewhat varying EF values (up to ±4.7% in terms of absolute EF for a high EF measurement), although this source of variability is less than the potential physiologic variation in an individual patient (see section 2.1.2 above).

2.1.3.4 Choice of Background ROI

Several different methods of selecting the background ROI have been described previously in section 2.5.2. Grove *et.al.* (1986) examined the sensitivity of LV EF to the background correction through analysis of a simple cardiac model. The model was a simple design; the LV was assumed to be spherical in shape, and the background to be completely beneath the heart, instead of a volume distribution. Clinical data did confirm the usefulness of this simplistic model. It was concluded that for varying LV ROI algorithms, when the background correction value is overestimated, the error in the EF can be very large. In contrast, when the background is underestimated, the error is relatively small and insensitive to the value of the background correction. Therefore it would be advantageous to estimate background conservatively, when designing an automated background ROI search routine.

2.1.4 Effects of Errors on Ejection Fraction Determination

2.1.4.1 Introduction

Examining the definition of EF in equation 1.1, it is possible to estimate the deviation of the EF from its true value when errors are made in EDC, ESC, or both. This may be accomplished by application of error propagation theory on equation 1.1.

Generally error sources may be classified as systematic or statistical. Statistical uncertainty in the EF will decrease as the number of counts acquired increases. In

contrast, systematic errors such as incorrect identification of the LV contours are more difficult to tackle, since they cannot be reduced by acquiring more data.

In order to examine the effects of error in the EDC or ESC, error propagation assuming Poisson statistics for all variables involved has been performed by Williams *et.al.* (1978). The fractional uncertainty in the EF as a function of EF and EDC was derived to be:

$$\frac{(\sigma EF)}{EF} = \frac{1}{EF}\sqrt{\frac{(1-EF)(2-EF)}{EDC}}$$

This equation, and simple rearrangements thereof, may be examined to explore the relationship between the error in EF, and the EDC and ESC estimates.

2.1.4.2 Outcome

It was found that statistical variations are more severe at low EFs, requiring approximately ten times the number of counts at a low EF (of say, 20%) than a normal EF (~60%) to achieve the same statistical accuracy (Williams *et.al.*, 1978). Measurement of a low EF is a problem of estimating a small mean difference between two noisy quantities (EDC and ESC).

Overestimation of EDC results in an increase in EF, while underestimation of EDC produces a decrease in EF. The effect of error in EDC alone is non-linear, and most prominent at lower EFs as demonstrated in Figure 2.1 (a).

The effect of error in the ESC estimation is linear with resulting EF, and more pronounced at lower EFs. An over- or underestimation of ESC produces an under- or overestimation of EF respectively as illustrated in Figure 2.1 (b).

In the situation where a systematic error of the same magnitude is made in both the EDC and ESC, the effect on EF is maximal when the true EF is high, and minimal when the true EF is low. This non-linear relationship is described for various EF values in Figure 2.1 (c). Errors in both EDC and ESC of the same absolute amount are a major problem in radionuclide studies. This is generally due to inclusion of counts originating from adjacent non-LV structures, via over- or undercorrection of EDC and ESC through a background estimate.

2.1.4.3 Summary of Error Effect

The magnitude and direction of change in EF is highly dependent upon the true EF value and the particular type of error considered. At a normal or high EF, the most likely error is due to an equal error in both EDC and ESC (Williams, 1978). The next most likely is attributable to error in ESC alone. The effects of statistical error and error due to EDC estimation alone on the measured EF is expected to be minimal. However, when the EF is low, the statistical error is likely to make the dominant contribution to error in EF.

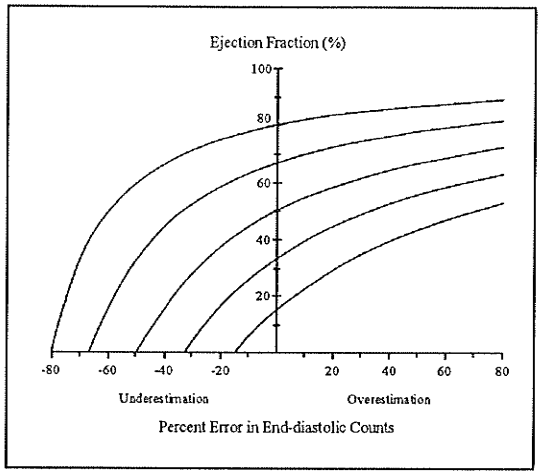

(a)

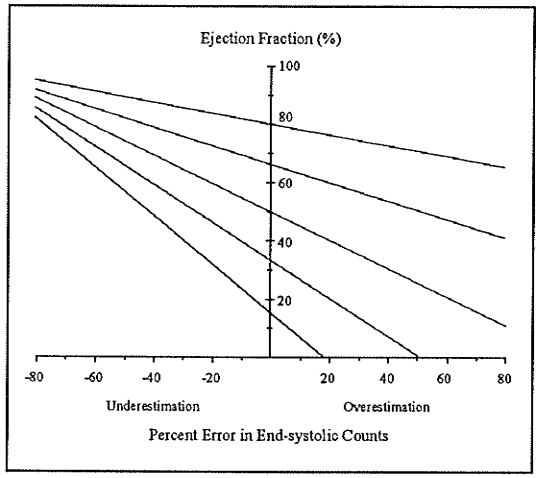

(b)

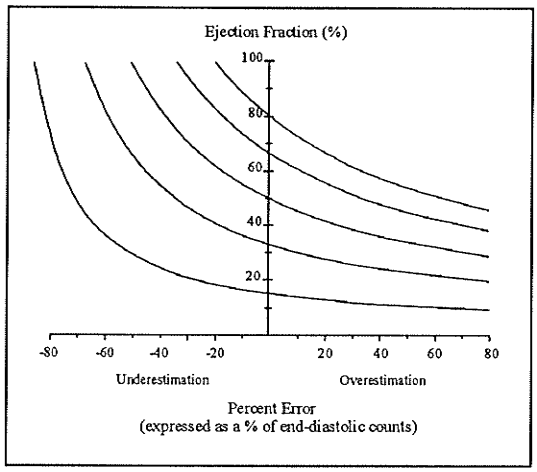

(c)

Figure 2.1: (a) The effect of systematic error in end-diastolic counts alone, (b) the effect of systematic error in end-systolic counts alone, and (c) the effect of systematic errors (of the same magnitude) in both end-diastolic and end-systolic counts.

References

ICRU Report 44: Tissue Substitutes in Radiation Dosimetry and Measurement. Bethesda, Maryland: 1989.

Bacharach, S.L., M.V. Green, D. Vitale, et al. "Optimum Number of Harmonics for Fitting Cardiac Volume." Journal of Nuclear Medicine 24 (5) (1983): P17

Boudraa, A.E.O., J.J. Mallet, J.E. Besson, et al. "Left Ventricle Automated Detection Method in Gated Isotopic Ventriculography Using Fuzzy Clustering." IEEE Transactions on Medical Imaging 12 (3) (1993): 451-465.

Brown, J.M., C.J. White, S.M. Sobol, et al. "Increased Left Ventricular Ejection Fraction After a Meal: Potential Source of Error in Performance of Radionuclide Angiography." The American Journal of Cardiology 51 (June) (1983): 1709-1711.

Burow, R.D., H.W. Strauss, R. Singleton, et al. "Analysis of Left Ventricular Function from Multiple Gated Acquisition Cardiac Blood Pool Imaging (Comparison to Contrast Angiography)." Circulation 56 (6) (1977): 1024-1028.

Busemann-Sokole, E., T.J. Farrell, and T.D. Cradduck. "Effect of Scintillation Camera Nonuniformity on Ejection Fraction Measurements." Journal of Nuclear Medicine 26 (11) (1985): 1323-1330.

Chang, W., R.E. Henkin, D.J. Hale, et al. "Methods for Detection of Left Ventricular Edges." Seminars in Nuclear Medicine 10 (1) (1980): 39-53.

Green, M. V., S. L. Bacharach, M. A. Douglas, et al. "Sources of Virtual Background in Multi-Image Blood Pool Studies." Nuclear Cardiology: Selected Computer Aspects. Ed. Anonymous. New York, NY: The Society of Nuclear Medicine, Inc., 1978. 97-106.

Grove, D.E., R.A. Stein, and J. Nosil. "Effect of background correction on left ventricular ejection fraction calculation through analysis of a simple cardiac model." Medical Physics 13 (6) (1986): 949-953.

Halama, J.R. and J.E. Holden. "The Effect of Stochastic Pixel Noise on the Distributions of Magnitude and Phase Values in the Fourier Analysis of Gated Studies." Journal of Nuclear Medicine 24 (5) (1983): P17

Hamilton, G. W., D. L. Williams, and J. H. Caldwell. "Frame-Rate Requirements for Recording Time-Activity Curves by Radionuclide Angiography." Nuclear Cardiology: Selected Computer Aspects. Ed. Anonymous. New York, NY: The Society of Nuclear Medicine, Inc., 1978. 75-83.

Makler, P.T., Jr., D.M. McCarthy, P. Bergey, et al. "Multiple-Hospital Survey of Ejection-Fraction Variability Using a Cardiac Phantom." Journal of Nuclear Medicine 26 (1985): 81-84.

Mukai, T., N. Tamaki, Y. Yonekura, et al. "Optimum Order Harmonics of Fourier Analysis in Multigated Blood-Pool Studies." Journal of Nuclear Medicine 24 (5) (1983): P17(Abstract)

Onik, G., L. Recht, J.E. Edwards, et al. "False Left Ventricular Aneurysm: Diagnosis by Noninvasive Means." Journal of Nuclear Medicine 21 (2) (1980): 177-182.

Powers, T.A., R.D. Bowen, R.R. Price, et al. "The Effects of Gating Delays on Ejection Estimates: Concise Communication." Journal of Nuclear Medicine 23 (1) (1982): 15-16.

Reiber, J.H.C. "Quantitative analysis of left ventricular function from equilibrium gated blood pool scintigrams: an overview of computer methods." European Journal of Nuclear Medicine 10 (1985): 97-110.

Schicha, H., U. Tebbe, P. Neumann, et al. "Underestimation of left-ventricular ejection fraction by radionuclide ventriculography in patients with aneurysm." European Journal of Nuclear Medicine 10 (1985): 338-340.

Sorensen, S.G., G.W. Hamilton, D.L. Williams, et al. "R-Wave Synchronized Blood-Pool Imaging: A Comparison of the Accuracy and Reproducibility of Fixed and Computer-Automated Varying Regions-of-Interest for Determining the Left Ventricular Ejection Fraction." Radiology 131 (1979): 473-478.

Sorenson, S.G., J. Caldwell, J. Ritchie, et al. ""Abnormal" responses of ejection fraction to exercise, in healthy subjects, caused by region-of-interest selection." Journal of Nuclear Medicine 22 (1981): 1-7.

Wackers, F.J.T., H.J. Berger, D.E. Johnstone, et al. "Multiple Gated Cardiac Blood Pool Imaging for Left Ventricular Ejection Fraction: Validation of the Technique and Assessment of Variability." The American Journal of Cardiology 43 (1979): 1159-1166.

Williams, D. L. and G. W. Hamilton. "The Effect of Errors in Determining Left Ventricular Ejection Fraction From Radionuclide Counting Data." Nuclear Cardiology: Selected Computer Aspects. Ed. Anonymous. New York, NY: The Society of Nuclear Medicine, Inc., 1978. 107-117.

Zatta, G., G.L. Tarolo, B. Palagi, et al. "Computerized analysis of equilibrium radionuclide ventriculography time-activity curve in the assessment of left ventricular performance: comparison of two methods." European Journal of Nuclear Medicine 10 (1985): 198-202.

Chapter Three: DESCRIPTION OF METHOD

3.0 Introduction

This chapter will describe the algorithm developed to calculate left ventricle ejection fractions. This algorithm automatically identifies the LV region in each frame of an equilibrium gated blood pool study, determines a background correction estimate, and calculates the corresponding ejection fraction. Each major processing step is described, in the order of application upon the image set. An accompanying flow chart is provided in Figure 3.1, listing the processing steps and the numbers of the corresponding sections which contain detailed descriptions of the steps.

A general description of the algorithm is useful at this point. The fuzzy *c*-means clustering routine, as described in section 1.3.5, is applied twice in this algorithm. The first application is used to extract the ventricles from primarily phase information. Additional processing, in the form of a simple edge detection, is applied in each image frame. Finally, a second application of the fuzzy clustering routine is performed on each individual image frame, using primarily grayscale information, to extract the LV ROI for that particular frame. The remainder of this section presents a more detailed description of the algorithm.

After the sequence of 16 2D image frames for the LAO view of the heart are loaded, two images are calculated which summarize the temporal information contained in the sequence. The first is the phase image, and contains the normalised estimation of the first harmonic of each pixels' TAC as computed by Fourier analysis. The second image is a pixel-by-pixel estimate of noise in the phase image. Each pixel represents an estimate of the similarity of its corresponding phase value as compared with surrounding phase pixels. These processing routines are illustrated in sections 3.1.1 and 3.1.2.

These two images are combined with the x- and y-coordinate data for each pixel to form a set of 4-tuple input vectors. This set of vectors (one input vector for each image pixel) is then passed into the fuzzy clustering subroutine. The input vectors are normalized to account for patient to patient variability, and adjusted by multiplicative weighting factors to emphasize the more distinguishing features, as described in sections 3.1.3 and 3.1.4. The results of the initial clustering are examined, and the cluster which contains the ventricles is identified for further processing.

The approximate geometric centre of the LV is identified through modification of a standard technique involving row-column signature analysis. To achieve a better estimate of the LV centre, a maximum gradient search routine is employed which identifies the maximum grayscale pixel within the LV, and this pixel is used as the new LV centre. This method uses the results of the row-column signature analysis as a starting point, and is discussed in further detail in section 3.1.5.

Once the LV grayscale centre is identified, a simple edge detection routine is employed on the LV portion which lies beside the right ventricle. A minimum is found along radial rays traced outwards from the LV centre. These minimum pixels represent the intraventricular septum, which is an easily recognizable valley of low counts separating the LV from the RV. These septal pixels are joined by linear interpolation, then the LV image information is isolated by stripping off the RV. The septum identification routine is explained in greater detail in section 3.3. Both the LV centre identification and the septum detection process are applied on each image frame of the study.

The remaining image data comprise a region containing signal from the LV blood volume, as well as pixels exhibiting temporal fluctuations in phase with the ventricles, but of low amplitude. The grayscale pixel data, together with the x- and y-coordinate data form the set of input vectors used in the second application of the fuzzy clustering routine. For this clustering, each pixel in the image thus possesses a corresponding three

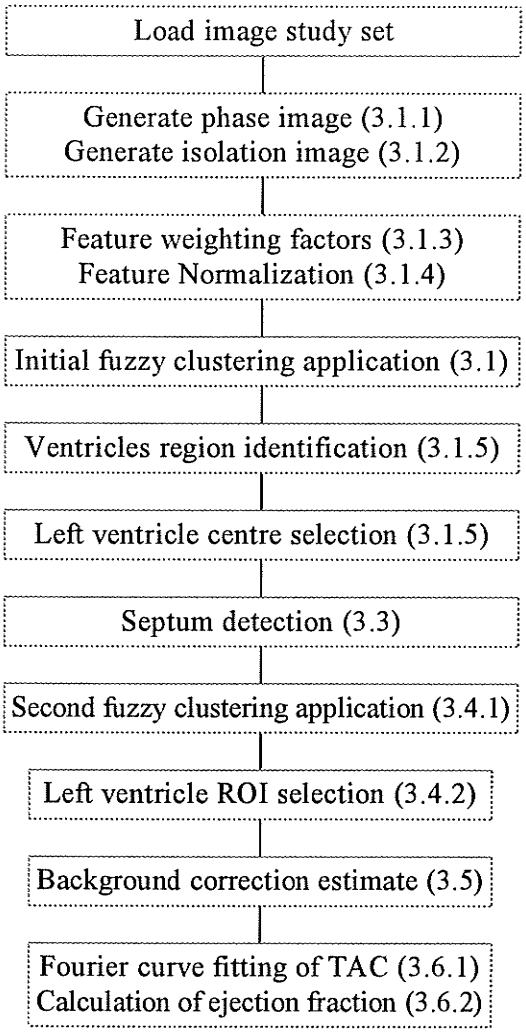

Figure 3.1: Flowchart summarizing steps taken in automated ejection fraction estimate through fuzzy clustering.

component input vector. Two clusters are identified in the remaining image, the LV and non-LV (background, scatter, ventricle wall, etc.). The LV cluster is determined in this way for each image frame as described in section 3.3. This cluster is taken as the LV region-of-interest (ROI) to be used in the calculation of an initial TAC, which is

uncorrected for background. The end-systolic frame is identified as the frame possessing the lowest LV activity, as observed in the uncorrected TAC.

The end-systolic frame is used for the background correction estimate. The process for identifying an ROI representative of background is fully automated. A method which closely simulates the background estimation procedure in the manual processing was developed. Radial rays separated by small angular increments are traced outwards from the LV centre toward the bottom and right edges (with respect to the image space). A region growing algorithm was applied for each ray, in combination with geometric boundary conditions based on radial distance outside the LV contour. The region exhibiting the smallest amplitude fluctuation over the cardiac cycle is defined as the background ROI. The background activity estimate is the count/pixel value within this region on the end-systolic frame. This processing is presented in detail in section 3.5.

Fourier curve fitting using three harmonics is performed on the corrected TAC. From this best fit curve, the ejection fraction parameter is calculated via equation 1.2 as described in section 1.2.2.

Throughout the development of this algorithm, it has been necessary to define or choose many parameters. The value of each of these will have some effect on the performance of the algorithm, but may have little influence on the final ejection fraction result. It is important to gauge these effects, and this is done through an optimisation process described in section 4.1. The optimisation is performed on a select group of parameters thought to have the most critical impact on the ejection fraction output. However, there does exist the possibility of a non-optimised parameter having some effect on the calculated ejection fraction.

3.1 Initial Clustering

3.1.1 Fourier Phase Analysis

The phase image is utilized clinically in assessment of left ventricular function, providing information related to the mechanical contractility of the heart and allowing regional wall motion abnormalities to be diagnosed. The grayscale value of each pixel in the phase image is derived from analysis of that pixel's time activity curve (TAC). The TAC of a pixel is formed by following the grayscale value of a pixel throughout each image frame. The TAC's of two pixels, one lying within the left atria and the other within the left ventricle, are given in Figure 3.2. The length of this curve is the average length of the cardiac cycle over the image acquisition period. In pixels which do not comprise part of a heart chamber, the TAC is virtually a horizontal line (with superposed noise). Fourier analysis is performed on each pixel's TAC and results in an estimate of that TAC's phase. This phase information is then normalized to form the 'phase image' as described below. The phase image derived from the pixel TAC's contains no information regarding the amplitude of each TAC, but effectively describes the timing of onset of contraction (relative to the R-wave).

In relation to the TAC, a pixel in the phase image shows the timing of the minimum of this curve. The timing is measured assuming that a full cardiac cycle contains 360°. These values are normalized to 0 through 255 (corresponding to 0° and 360° respectively) for an 8 bit grayscale display in the phase image. Normal values of the phase of the ventricles lie within the 140°-210° range. Since the phase image summarizes the timing of contraction, the atria and ventricles will generally appear approximately 180° out of phase due to the normal sequence of cardiac contraction (see Figure 3.2). This characteristic makes the phase image an important input feature to the initial clustering process.

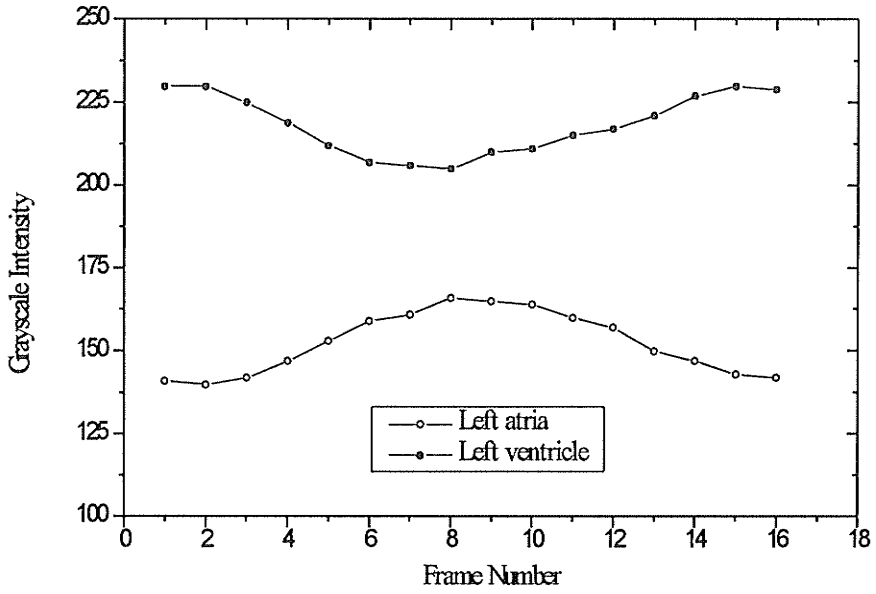

Figure 3.2: Example of time activity curves for pixels lying within the left atria and left ventricle.

Fourier analysis provides a powerful method of describing a TAC. A TAC may be accurately represented as an infinite Fourier series expansion:

$$TAC(t) = a_0 + \sum_{m=1}^{\infty} a_m \cos(2\pi mt - \phi_m) \tag{3.1}$$

where a is the amplitude, m is the number of the harmonic (or term), t is the time (or frame number), and ϕ is the phase value. The amplitude of the first harmonic term is generally larger than that of subsequent terms. The second and third harmonic terms become relatively more important in regions of aneurysm (Vallette, 1990). Thus, the second and third harmonic phase images, while containing clinically useful information, do not enhance the visualization of the ventricles region (Merrick, 1984). An examination of ten image sets revealed that the second and third harmonic phase images

did embody some structure. However, the quality of this structure for the purpose of identifying the ventricles was insufficient to warrant using these images as input features for the initial clustering.

The first harmonic phase image may be calculated by initially describing the TAC of a pixel by Fourier cosine and sine expansions (implicitly incorporating the ϕ phase information from equation 3.1):

$$f_{\sin}(i,j) = \sum_{k=1}^{n} \sin\left[\frac{2\pi h}{n}(k-1)\right] * P(i,j,k) \tag{3.2}$$

$$f_{\cos}(i,j) = \sum_{k=1}^{n} \cos\left[\frac{2\pi h}{n}(k-1)\right] * P(i,j,k) \tag{3.3}$$

where k is the frame number, h is the harmonic number, n is the number of frames comprising one cycle, and P is the pixel grayscale value at coordinates (i,j) in frame k. The first harmonic phase image is found by setting $h = 1$ in the above and:

$$f_{phase}(i,j) = \tan^{-1}\left(\frac{-f_{\sin}(i,j)}{f_{\cos}(i,j)}\right) \tag{3.4}$$

The choice of n in the Fourier series expansions above is taken to be less than the total number of frames available. A typical TAC does not necessarily end at the same graylevel at which it began because normal fluctuations in the R-R interval (that is, time between measured R-wave pulses in the cardiac cycle) result in the later frames including counts from fewer heartbeats than the earlier frames.

Two difficulties arise when using the phase image quantitatively. In a healthy subject, the atrial contraction occurs at the beginning of the cardiac cycle, followed by the contraction of the ventricles approximately 180° later. The normalized grayscale

values for these events in the phase image are 0 and 128 respectively. Due to the inconsistency of the time length of heart cycles during an image acquisition, the timing of the atrial and ventricle contractions as observed in each pixel's TAC will be the resultant average over a large number of heart beats. Secondly, the phase analysis of the cardiac cycle intrinsically defines a sharp beginning and end point at 0° and 360° respectively. Since the calculated first harmonic phase values (ranging between 0° and 360°) are normalized to completely fill a 256 grayscale spectrum, the values of 0° and 360° which essentially represent the same phase value, are represented by maximally different grayscale values.

To reduce the effects of this 'wrap around' problem on the initial clustering a 'decay' process is applied to the phase image, named because of the effect it has on certain pixels in the phase image. This process involves changing pixel grayscale values lying 30° above the 245-255 range to a value of 255. However, the pixel is only changed if it is already touching a pixel of value 255 or 0, so the decay of isolated random noise is minimized. The procedure is applied iteratively on the original phase image. It was found that ten passes were sufficient to reach an equilibrium state. To summarize, this decay process results in low grayscale pixels, which are in contact with maximum intensity pixels, being redefined as maximum intensity pixels. An original first harmonic phase image and decayed phase image are displayed in Figure 3.3. These images demonstrate that the decay process as described above accentuates the atrial chambers and enhances the difference between the atria and ventricles along common edges.

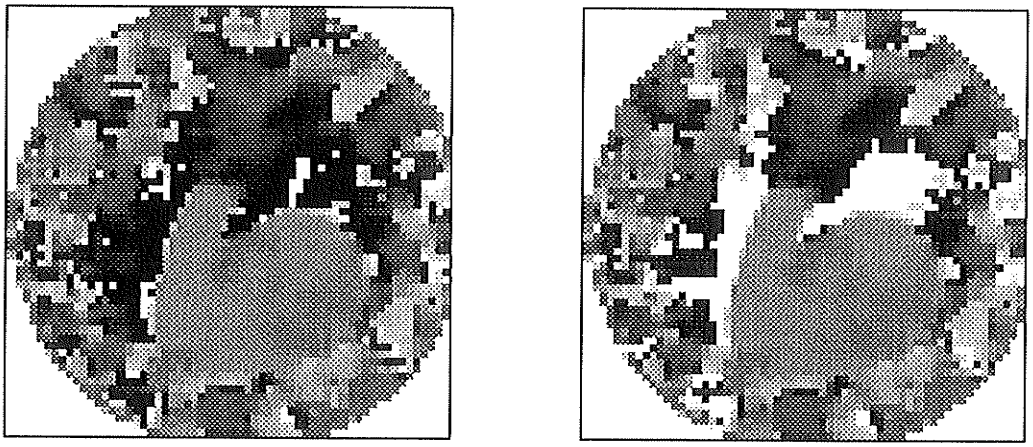

(a) (b)

Figure 3.3: (a) Phase, and (b) decayed phase images.

3.1.2 Isolation Status

A method for estimating the noise of individual pixels as described by Itagaki (1990) is applied to the phase image. This is a fast and simple technique for assessing the similarity of a pixel to its surrounding neighbours. The eight pixels surrounding the pixel of interest are investigated. The number of pixels which have an absolute grayscale difference from the pixel of interest smaller than a preset limit δ is determined (this number is referred to as I from now on). I then varies between zero and eight, and is termed the "isolation status" of the pixel of interest. A value of zero would indicate that the pixel of interest is very different from all the surrounding pixels, since all were outside the $\pm\delta$ range. A value of eight would indicate that the pixel of interest was quite similar to all the surrounding pixels, with all lying inside the $\pm\delta$ range. For example, examine the following pixel of interest with a normalized phase value of 145, and surrounding neigbouring phase values of:

	i - 1	i	i + 1
j - 1	152	162	142
j	147	145	133
j + 1	157	139	134

If $\delta = 10$, only 4 neighbouring pixels lie within the $\pm\delta$ range, so I would be 4. Now if $\delta = 15$, then 7 neighbouring pixels would lie within the $\pm\delta$ range, yielding an I of 7. It should be noted that the value of I is quite sensitive to choice of δ.

To view the isolation status image, I was normalized to fill the entire 0 - 255 grayscale spectrum. Regions of similarity in the phase image are shown as very bright in the isolation image, while regions with a high amount of pixel to pixel variability are dark. Hence, regions of similar phase, such as the ventricles or atria, are emphasized in the isolation image.

An attempt was made initially to chose δ as the standard deviation of the grayscale phase values in a 3×3 matrix surrounding the pixel of interest. This resulted in an erosion of the edges of the ventricles region, due to the standard deviation of edge pixels being higher than that of the centre of a region of similarity. Thus, the choice of parameter δ is made through an optimization process described in detail in section 4.1.

A method of cleaning up the isolation image in areas of noisy data is applied. This processing basically results in an almost binary representation of noise. That is, the noisy pixel values are smeared and averaged, while regions of low noise are preserved. This is not necessary to the functioning of the overall algorithm, but does simplify the interpretation of the isolation component of the average cluster vectors.

Before being used as an input feature to the initial clustering, the isolation image is slightly modified in the following manner. If an isolation image pixel grayscale value lies below 160 (equivalent to an I of 5), then it is replaced by the average of the

surrounding pixels. An example of the isolation image, as derived from the phase image presented in Figure 3.3, and the processed isolation image are illustrated in Figure 3.4. It may be observed that the processed isolation image displayed in Figure 3.4 has essentially been smoothed, without losing any high grayscale (meaning non-noisy) pixel data.

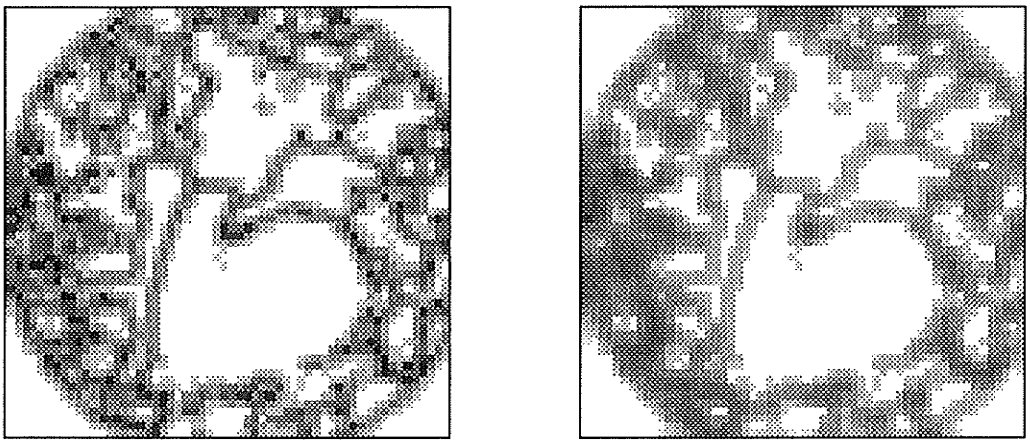

(a) (b)

Figure 3.4: (a) Isolation, and (b) processed isolation images.

3.1.3 Feature Normalization

Images from different patients are usually not comparable due to interpatient variability in the orientation and volume of the heart, even under similar acquisition conditions. Acquired counts will vary between patients, despite the scaling of administered dose to match patient weight. Counts per pixel per unit time are dependent on the heart volume, concentration of radioactive material used, and the background radiation level. A normalization of features suppresses this interpatient variation (Syrchra, 1989). The x- and y-coordinate data are normalized by dividing each by the

median value. Since each individual image frame is 60×58, the median values are 30 and 29 respectively. This ensures equal emphasis is placed on the x- and y-coordinate data, even though the image frame is slightly elongated along the x-direction. The phase and isolation data are also normalized through division by their median values.

3.1.4 Feature Weighting Factors

For the initial clustering, both the phase and isolation images are used as features, as well as the x- and y-coordinate data for each pixel. By preweighting the features, their relative importance in terms of discriminating classes may be established. Hence, more weight can be given to those features which are more useful in distinguishing classes. Previous experiments have indicated that features of high magnitude, yet possessing low discriminatory power, will minimize the clustering criterion but give a misrecognition [Boudraa, 1993]. A set of weighting factors is introduced to emphasize the more powerfully discriminating features.

The weighting for the x- and y-coordinate data is restricted to be the same. This is necessary since the inherent resolution of the gamma camera in both these directions is the same. Since the isolation data is directly derived from the phase data (hence, dependent variables), the weighting factors for the phase and isolation data are restricted to be the same value. Therefore, only two weightings are needed: one for the phase and isolation data, the other for the coordinate data. However, because these input components are normalized by their median values (ie. the median value will be represented by a 1.0 input), only one weighting need be used, and the other weighting may be taken as 1.0. Hence the weighting is performed on the more important features, the phase and isolation data, and the coordinate data is held after normalization at an effective weighting of 1.0.

3.1.5 Ventricles Region Identification

3.1.5.1 Use of Cluster Centre Data

The first clustering application results in the division of the feature vectors into five clusters. The number of clusters is an input parameter. Five clusters were chosen: one to identify the atria, one to identify the ventricles, one to identify the resultant movement of the great vessels (essentially a type of 'noise'), and two to identify noise in the phase image. The reasoning for this is as follows. In the ideal phase image, the only two distinct features which should exhibit the same phase are the atria and ventricles. However, we may assume that these two features lie about 180° apart. Assuming the most general case, on a finite number line ranging from 0° to 360° insertion of two features which are known to be separated will result in three inter-feature regions. One region lies below the lower of the two known features, one region lies inbetween the two known features, and one region lies above the higher of the two known features. For this reason, the fuzzy clustering algorithm is set to identify 5 clusters using the phase data. Granted, the atria contraction ideally should begin at 0°, thus restricting one of the two known features to lie at one end of the degree number line, which could be described adequately with 4 clusters. The use of 4 clusters was explored, but the impact on final ejection fraction results compared to using 5 clusters was insignificant, hence the most general case scenario was adopted. Figure 2.5 illustrates the resulting clusters after the first clustering application. Note that Figure 3.5 (c) is the output of the fuzzy clustering routine using the images in Figure 3.5 (a) and (b) as input. The clusters were randomly assigned a grayscale value so as to maximize the contrast between the clusters. The actual grayscale values of each cluster in Figure 3.5 (c) are meaningless to the algorithm and chosen for visualization only.

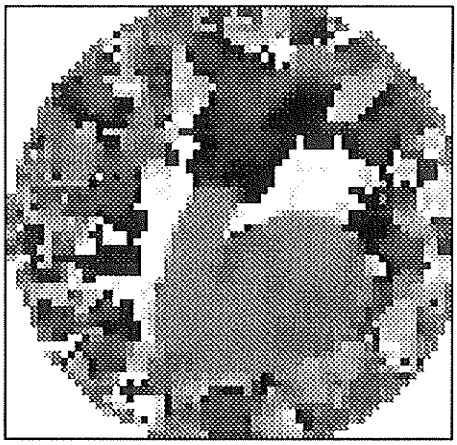

(a)

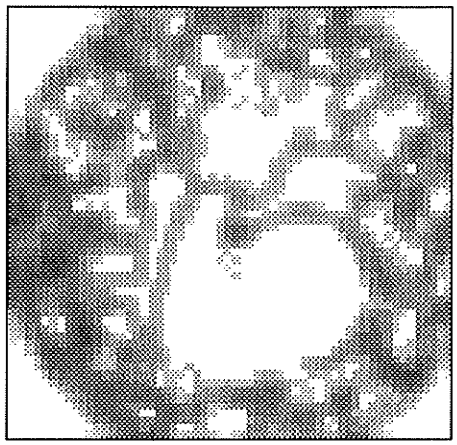

(b)

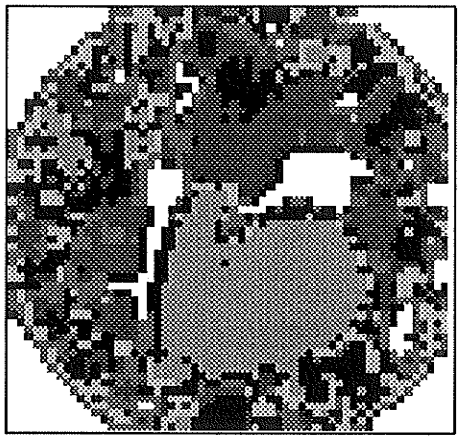

(c)

Figure 3.5: (a) Phase image, (b) isolation image, and (c) results of using (a) and (b) together with *x*- and *y*-coordinate pixel data as input feature vectors to the fuzzy clustering routine.

The cluster centre vector is utilized to assist in recognizing a particular cluster as representing the ventricles. During any clustering application, the fuzzy clustering subroutine keeps track of all cluster centres. Each cluster centre is defined as a vector in the feature space, beginning at the origin and ending at the cluster centre coordinates, which are simply each feature's average value in that particular cluster.

The two features used to discriminate the ventricles cluster from the atria and other clusters are the phase and isolation values. From the previous discussion of the gating method, it is known that the first image frame is acquired when the left ventricle is approximately at maximum volume and is about to begin contraction. Examination of a typical ventricular volume versus ECG signal (Palmer,E.L., *et. al*, 1992) shows that the ventricles will be at a volumetric minimum somewhere in the 100° to 210° range, as demonstrated in Figure 3.6. The typical minima would occur at about 165° for a normal heart. This range of phase values is used to rule out clusters from being ventricle candidates. Any cluster centre whose phase centre coordinate does not lie within the 100° to 210° range (71 to 149 grayscale) is not considered further as a ventricles cluster candidate. The remaining clusters which do satisfy this criterion are examined for their isolation center coordinate. Of the remaining clusters, the one with the highest isolation centre coordinate is chosen as the ventricles cluster. This is the cluster whose average isolation value is the highest, implying a high degree of similarity among its pixels. This approach works very effectively, since only the atria and ventricles clusters will possess a high isolation centre coordinate, and the atria will have been disposed of previously due to the phase comparison. The average x- and y-coordinate values are not useful in identifying the cluster representing the ventricles.

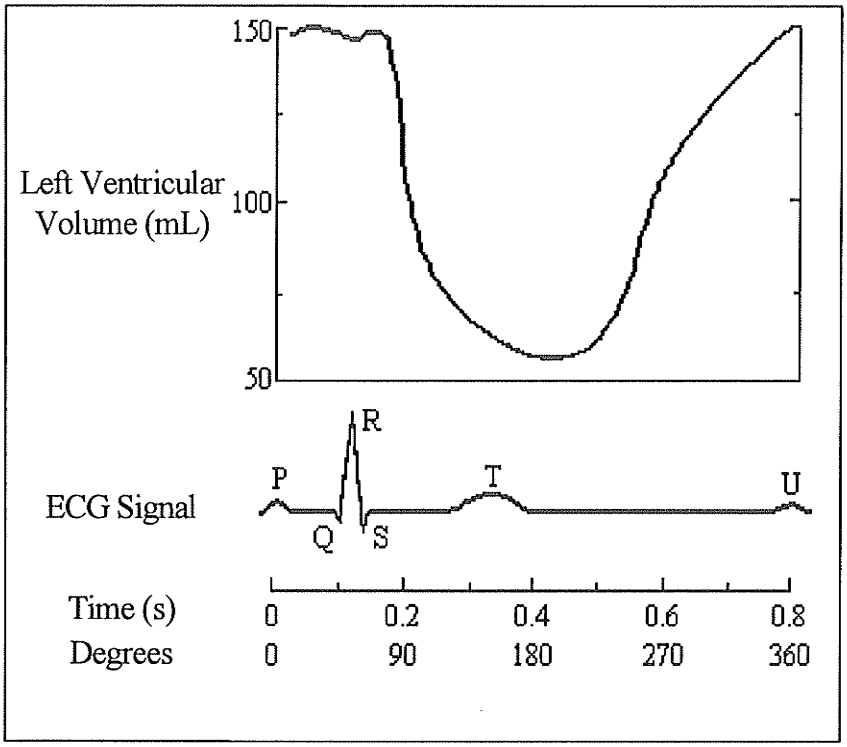

Figure 3.6: Superposition of left ventricular volume-time curve and ECG signal for a typical cardiac cycle (adapted from Palmer, *et.al.*, 1989).

3.5.1.2 Defining a Clean Ventricle Cluster

The cluster identified as the ventricles is not a single, continuous shape, but is generally comprised of the ventricles plus some background noise which has been incorrectly classified as belonging to this cluster. This background noise simply consists of pixels which happen to possess phase and isolation characteristics similar to the ventricles due to random statistical fluctuation. Usually these pixels are separated in Cartesian space from the true ventricles, as depicted in Figure 3.7 (a). A simple method of eliminating these small isolated clumps of noise involves applying a growth segmentation algorithm beginning at the ventricles x- and y-coordinate centre point. A growth segmentation algorithm is an image processing technique which, when given a starting point, will expand a region surrounding this point based on some predefined

classification criteria. This routine grows the given centre point of the ventricles cluster (as identified by the fuzzy clustering algorithm in terms of the average x- and y-coordinate of the cluster) outwards and the only restriction is that the region may not grow into or across any zero pixel values. Since the only non-zero pixel values are those belonging to the identified ventricles cluster, this growth segmentation algorithm effectively eliminates any outlying clumps of noise from the main ventricles region. Obviously it is essential that the initial coordinates fed into the growth algorithm do, in fact, lie within the correct ventricles region of the cluster. Since the ventricles cluster will contain relatively few noisy pixels, their contribution to the cluster centre coordinates will not be significant enough to pull the centre outside of the main ventricles region. In the clinical images processed, no problems have been observed with this assumption, nor with the growth segmentation algorithm. This is a simple and effective method of removing incorrectly identified noise pixels from the identified ventricles cluster.

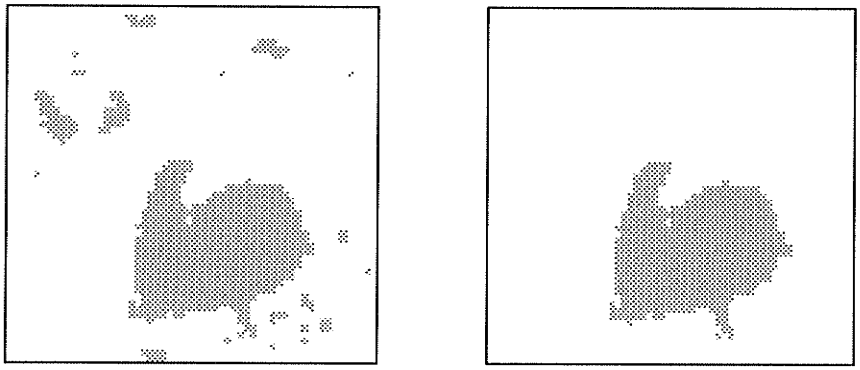

(a) (b)

Figure 3.7: These are binary spatial displays where gray represents an image pixel within the identified ventricles cluster, and white represents image pixels not classified within that cluster. Specifically, (a) Represents the initially identified ventricles cluster, and (b) after application of region growing algorithm to remove noise.

3.1.5.3 Morphological Processing

Further processing of the ventricles cluster is performed by applying a closure to the cluster. A closure is a morphological image processing technique which tends to smooth sections of the boundary by fusing long thin gulfs, eliminating small holes, and filling in boundary gaps (i.e. indentations). Since only the shape of the cluster is modified here, the ventricles cluster is first converted to a binary image (pixel values only 0 or 255). This is accomplished by leaving all pixels with a value of 0, while converting all non-zero pixel values to a value of 255. A closure is defined as a dilation followed by an erosion process as described below (Pratt, 1991).

The dilation is accomplished by using a 3×3 square structuring element as a convolution mask. This mask is passed over the image, and if any part of the mask overlaps a nonzero pixel, then the image underneath the entire mask is set to 255. The erosion is performed in the same manner, except that if any part of the mask overlaps a zero valued pixel, then the image underneath the entire mask is set to 0. The slight enlargement of the cluster area resulting from the dilation process is countered by the shrinking effect of the erosion. In this way, the ventricles cluster boundary is smoothed, and any interior regions which were not clearly identified as belonging to the cluster are now included. As illustrated in Figure 3.8 the identified ventricles cluster, displayed as a binary image, engulfs a pixel of noise at the top of the septum, as well as a thin extension at the bottom on the left ventricle side (resulting from phase values similar to the left ventricle pixels). The morphological processing applied removes the noise pixel, solidifies the small branch, and generally smooths the contour edge. A smooth contour edge is desirable because in reality the heart is composed of smooth edges.

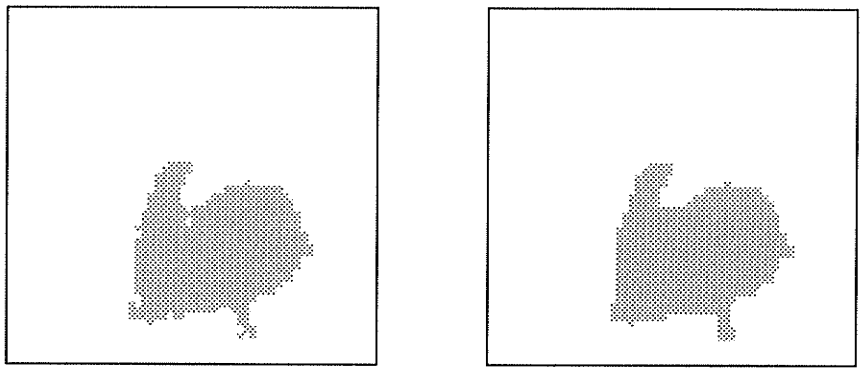

(a) (b)

Figure 3.8: (a) Identified ventricles cluster, and (b) same cluster after morphological processing.

The final shape of the ventricles cluster is applied as a mask to all frames of the image set. Any pixels which lie within this mask are passed on for further processing, while those lying outside the mask are no longer used.

3.2 Left Ventricle Centre Detection

3.2.1 Geometric Centre Calculation

3.2.1.1 Description of Method

The approximate geometric centre of the left ventricle is found by applying a modification of a method presented by Reiber, *et. al*, 1983. The original method developed by Reiber sums the grayscales of all the columns and rows in the first frame of the study. These row and column signatures are then smoothed with a five point averaging operation. A provisional centre is found by searching the row and column sums at the right lower corner of the image for the first (for reasons described in the following paragraph) local maximum values above precalculated row and column thresholds. These threshold values are defined through an empirically derived equation. A 98% success rate of correctly identifying the approximate left ventricle centre was attained by Reiber with this method. The remaining unsuccesful 2% identified points outside the left ventricle.

The revised method employs the same basic technique, that of examining the row and column signatures. However, this is done only after the ventricles cluster is applied as a mask to each of the 16 frames of the study. Each frame now contains only data which corresponds to the ventricles mask. The rest of the grayscale data in each frame are not processed any further. The column and row sums are found, and these are divided by the number of pixels contributing to each sum. This normalization process renders the individual column and row signatures independent of column or row length. This step is unnecessary in the original method since the signatures are taken from a square matrix. Use of the irregular shaped ventricles cluster as a mask makes the normalization step essential to the successful performance of this routine. Only columns or rows containing more than seven pixels are allowed to contribute to the signatures, so

as to remove those columns and rows which lie on the edge of the ventricles cluster. No smoothing is performed on the column and row signatures. The column signature is scanned from right to left, and the column coordinate of the first local maxima found is defined as the x-coordinate of the initial LV centre. The first local maxima is used when scanning the column signature because a normal heart should exhibit a lateral separation of the left and right ventricles, with the septum in between. The row signature is searched for the global maximum, which is defined as the y-coordinate of the initial LV centre. The global maximum is used here since the left and right ventricles should be at approximately the same vertical height within the image. The approximate geometric LV centre is found in every image frame.

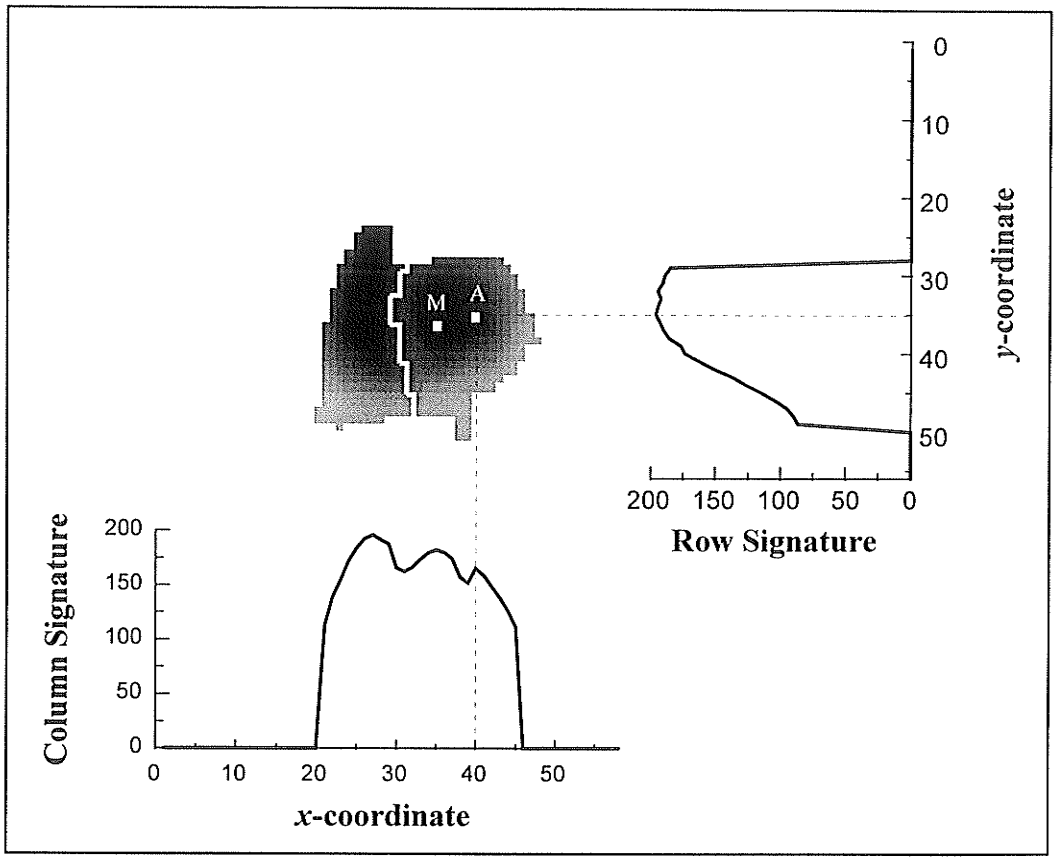

Figure 3.9: Demonstration of column/row signature method as adapted from Reiber, *et.al.*, 1983. Approximate geometric centre for this image is identified as (40, 35) and labeled as 'A'. The grayscale maximum of the left ventricle (see section 3.2.2) is labeled as 'M'.

3.2.1.2 Enhancing Robustness

The centre identification process as described above may be made much more robust by imposing a few logical restrictions on the choice of the approximate geometric centre. Furthermore, incorporation of the ventricles cluster centre information results in a more powerful and flexible algorithm.

Firstly, in certain situations, such as when the top of the RV displays much higher radioactivity than the LV, the geometric centre may be skewed erroneously upwards, due

to a shifting of the global maxima of the row signature. To correct for this and other similar situations where parts of the RV dominate the LV, a restriction is imposed on the y-coordinate of the geometric centre. If this coordinate is identified within three rows of either the top or bottom of the cluster, then redefine it three units towards the ventricles cluster centre y-coordinate. This is a somewhat arbitrary choice, but would actually be used only in a worst-case scenario. The correction simply ensures the approximate LV centre will lie between the mitral valve and apex. In conjunction with application of the algorithm described in the next section (3.2.2), this simple correction is adequate to handle the aforementioned situations.

Secondly, a major problem which can occur with this algorithm, is the lack of an LV local maximum in the column signature. That is, there is no decrease observed in the column signature due to the lower activity within the septum, as one moves from the LV columns into the RV columns. This difficulty will result in failure using the original method. By checking the first local maxima found in the right-to-left scan of the column signature and comparing it to the ventricles cluster centre x-coordinate, images in which this problem occurs may be identified. If the first local maxima is found to lie to the left of the ventricles cluster centre, then this problem has occurred. Once this situation is recognized, the ventricles cluster centre coordinates are used to roughly estimate an x-coordinate for the LV geometric centre. This x-coordinate is redefined as the coordinate lying halfway between the ventricles cluster centre x-coordinate and the rightmost edge of the ventricles cluster, within the row coinciding with the previously identified LV geometric centre y-coordinate. This solution has been successful in all encountered situations (1 image set to date) of a missing local column signature LV maximum.

3.2.2 Grayscale Local Maximum Detection

This algorithm uses the approximate LV geometric centre coordinates as described in the previous section as the initial starting point. At this point, the grayscale gradients between the pixel of interest and the surrounding eight neighbours are calculated (a positive value indicating a neighbour with a larger grayscale value). The point possessing the highest gradient value is labeled as the new pixel of interest. The gradient process is then repeated, and eventually the pixel of interest migrates to the maximum grayscale pixel of the local maxima region encompassing the original starting point.

In situations where there are more than one surrounding gradient of highest value, the algorithm chooses randomly between the alternatives. If the pixel of interest is found to be at the same graylevel as one or more surrounding pixels, and if there are no pixels higher (eg. a case of joined multiple pixel grayscale maxima), than the pixel of interest simply slides randomly to one of these neighbouring pixels. The graylevels of the two previously identified pixels of interest are stored. If these two values match the current graylevel, then the gradient searching is stopped. This signifies discovery of multiple pixel grayscale maxima. Of course, if a unique maximum grayscale value is found, the gradient search will also stop.

A 9×9 square matrix surrounding the pixel of interest is examined. Any pixel possessing a grayscale in that matrix which is the same as the pixel of interest will be identified as contributing to the LV grayscale maximum. The average of all of these pixel's x- and y-coordinates will be the LV graylevel maximum centre coordinates. However, if a higher grayscale value is found and lies within a four unit radius of the original identified centre, this new point is redefined as the maximum grayscale centre. The maximum grayscale centre in relation to the approximate geometric LV centre of a sample image frame is illustrated in Figure 3.9.

Only one problem has been encountered so far using this process. If the initial geometric centre coordinates do not lie within the local region of the LV, then the LV grayscale maximum centre pixel will be erroneously identified. The most probable situation will be a migration towards the RV grayscale maximum. By comparing the grayscale maximum pixel coordinates with the ventricles cluster centre coordinates, this situation may be recognized if the x-coordinate of the former is less than the x-coordinate of the latter. Situations where this may occur are characterized by an initial y-coordinate being too low, resulting in a starting pixel of interest lying too high on the LV. Thus the gradient may be slightly stronger towards the RV as compared to the LV. This type of condition may be identified through comparison of the grayscale maximum x-coordinate with the ventricles cluster centre x-coordinate. The situation may be corrected easily enough by modifying the initial pixel of interest coordinates and repeating the maximum grayscale pixel search. The modified initial x-coordinate is defined as the cluster centre x-coordinate plus one third of the distance to the right side of the ventricles cluster. The modified initial y-coordinate is defined as halfway between the previous initial pixel of interest y-coordinate and the cluster centre y-coordinate.

Additionally, for false early local maxima encountered in the column signature scan (such as that demonstrated in Figure 3.9) the gradient search routine will still be able to correctly identify the LV grayscale max. By applying this gradient search routine, the initial guess of LV geometric centre need only fall within the local region of the LV. The maximum grayscale pixel of the LV is found in each frame of the study.

3.3 Septum Identification

3.3.1 Introduction

The tissue wall separating the left ventricle from the right ventricle is known as the intraventricular septum. This wall is approximately 1 cm thick and is divided into two major zones. The outer two-thirds relative to the LV is composed of compact muscle, while the inner third is a trabeculated zone (ie. strands of connective support tissue). In the radionuclide images, the septum is an area of low intensity since it does not contain any continuous blood volume, but is perfused to some extent with blood due to the active muscle tissue. This area of low intensity separates two areas of high intensity, the left and right ventricles. The septum is a major anatomical landmark visible in all normal LAO view gated blood pool cardiac studies. For this reason, a straight-forward grayscale edge detection algorithm should be the simplest and most reliable approach of identifying this feature. Three different algorithms for identifying the septum were examined, all of which are based on simple edge detection methods.

For each method, the pixel identified as 'the septum' is not included as part of the LV. It may be demonstrated that the inclusion of these 'septum' pixels in the LV has little effect on the final ejection fraction calculation. Applying the adopted septum identification technique on a sample image set illustrates the magnitude of the effect. The calculated EF without including the septum pixels is 35.3%, and including the septum pixels is 34.4%. The difference of 0.9% (in absolute EF units) is insignificant.

3.3.2 Techniques Explored

3.3.2.1 First Derivative Method

This routine identifies the septum by examining the first derivative of the grayscale data on rays traced radially outwards from the previously identified grayscale maximum of the left ventricle. These radial rays are drawn at 10 degree intervals between 180 and 360 degrees. The previously described (section 1.1.3.6) spatial and temporal filtering reduces noise in the images. The derivative is calculated by subtraction of grayscale values of successive points along the radial line. The derivative will initially have a negative value as the grayscale drops off from the LV maximum, but will rise again once the grayscale values begin increasing, for example when the ray enters the RV. The pixel associated with the first minimum value of the derivative is identified as the septal point for that particular ray. If the edge of the ventricles region is encountered before a clear minimum is found (for example, at the top of the LV), then the pixel lying just outside the ventricles region along the ray is defined as the septal point for that ray. Once this process is repeated for all the rays, the identified septal points are joined by linear interpolation. The right ventricle is then stripped away from the image. The results of this routine on a sample image set are contained in Figure 3.10.

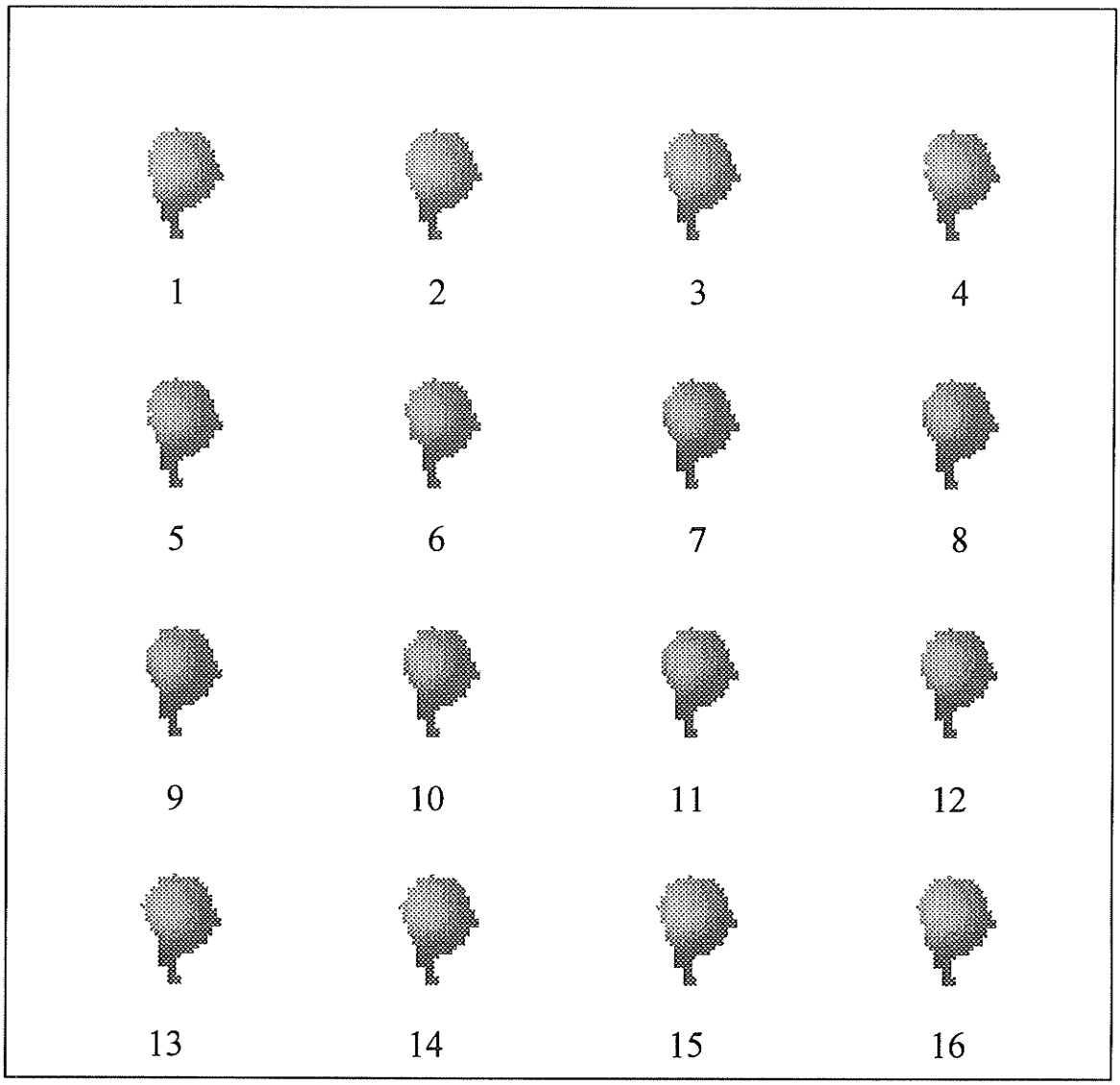

Figure 3.10: Results of first derivative septum identification routine on a 16 frame example image set.

3.3.2.2 First Minimum Method

This procedure examines radial rays traced outwards from the identified left ventricle grayscale maximum, and defines the first grayscale minimum encountered as the septal point for that ray. The radial rays are separated by 10 degree increments and

are spread out between 180 and 360 degrees relative to the LV grayscale maximum. Consecutive pixels along the ray are examined, and the pixel which demonstrates an increase in intensity relative to the previously examined pixel is identified as a septal pixel. The application of this septum search method is illustrated in Figure 3.11.

In addition to the noise reduction achieved through the preprocessing, two conditions are placed on the search for the minimum in order to increase the robustness of the algorithm. The first condition compares the grayscale value of the pixel of interest with the grayscale maximum of the LV, and does not allow a pixel to be identifed as the septum point if the difference is within ±5 grayscale levels. This accounts for a possible small error in identifying the LV grayscale maximum which is described as follows. If the LV grayscale maximum is defined by averaging the *x*- and *y*-coordinates of multiple maximum values (ie. in the event of a tie for highest grayscale), the defined point may in fact lie between the multiple maxima and thus when radial rays are examine, a false minimum is encountered when the radial ray passes over a true maximum. An example of this scenario lies in Table 3.1 below.

y-coordinate	*x*-coordinate				
	30	31	32	33	34
28	227	231	229	230	229
29	229	***235***	234	***235***	231
30	227	230	233	***235***	231
31	225	228	230	229	228
32	220	224	226	223	220

Table 3.1: Sample grayscale values to illustrate a 'false' minimum situation.

As may be observed, there are three grayscale values tied for the maximum at 235. By taking the average of the *x*- and *y*-coordinates of these pixels, the LV centre would be defined at (32, 29), which has a grayscale value of 234. Thus, when a ray is traced outwards from the LV centre to the 'left' along row 29, the applied condition corrects the algorithm from misidentifying the minimum as point (32, 29). The second condition attempts to account for a slight increase in pixel intensity along a ray, en route to the real septal minimum. This is simply a pixel with a high amount of noise. Occasionally, a small increase of one grayscale level may be observed while tracing a ray towards a true minimum. For example, the sequence of grayscale values along a single ray may look like:

Pixel	1	2	3	4	5	6	7	8	9	10	...
Grayscale	235	230	228	229	220	209	200	195	200	206	...

Obviously a clear minimum is located at position 8, but a false minimum at position 3 also exists (due to the slight increase in grayscale of pixel 4). However, if the algorithm is suspicious of any minima whose succeeding pixel grayscale value increases by only 3 units or less, these false minima may be identified. When a pixel is labeled as suspicious, the next pixel in the ray is examined and compared with the previous pixel grayscale value. If an increase over the previous value is found, then the minima being examined will be correctly identified as the septal point, otherwise it will be passed over in search of a more definite minimum.

When minima for all rays have been identified, linear interpolation is used to join the points into a solid boundary. The right ventricle is then stripped off of the image.

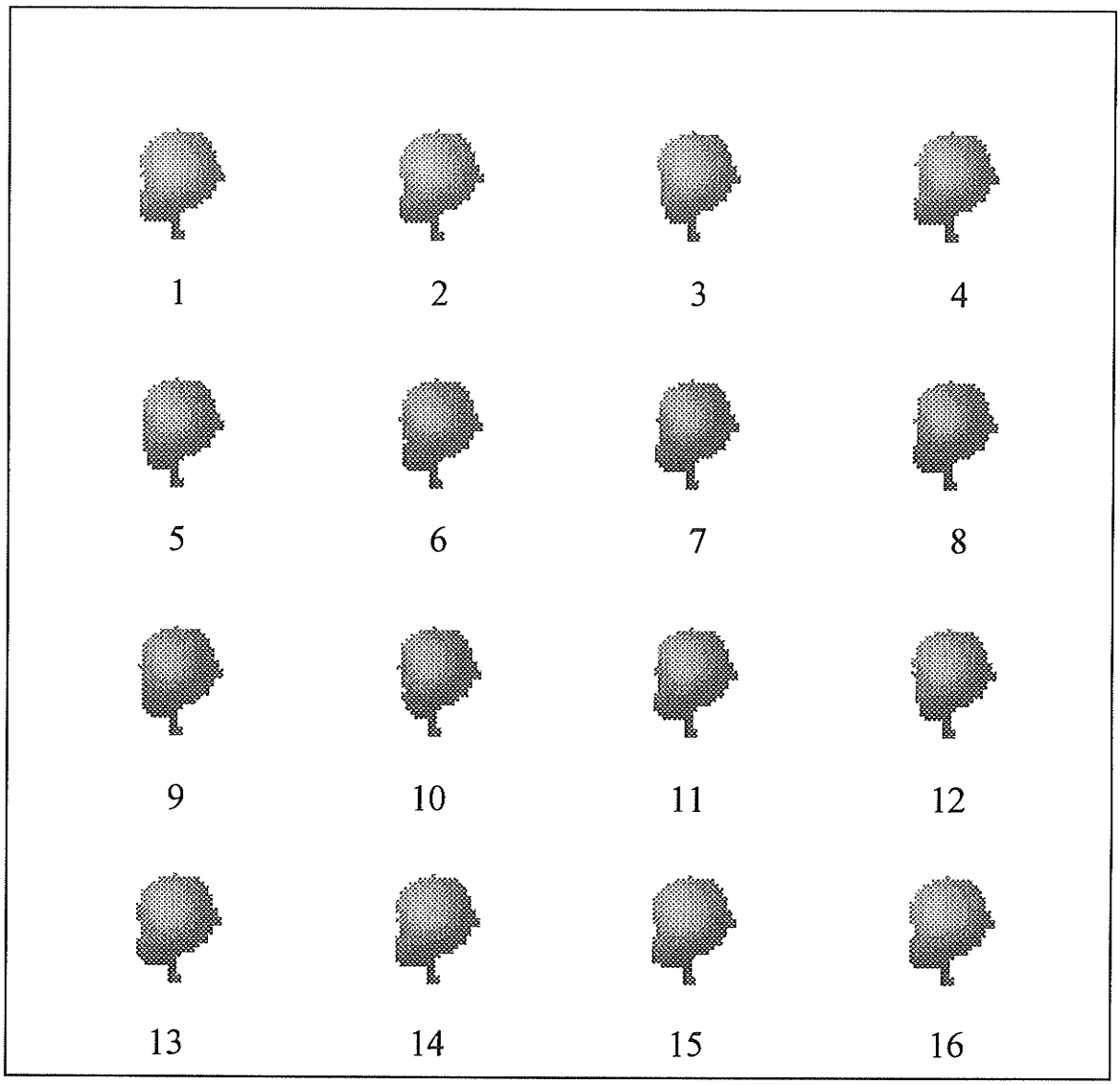

Figure 3.11: Results of first minimum septum identification routine on a 16 frame example image set.

3.3.2.3 Minimum/Horizontal Scan Method

This method combines the minimum method as described above with a horizontal scanning process. Noise is smoothed by the preprocessing and robustness routines previously described (section 3.3.2.2). The routine utilizes the minimum method to identify the top portion of the septum, between 270 and 360 degrees relative to the LV centre. For the bottom portion of the septum, the image matrix is scanned horizontally from right to left, by row. The starting x-coordinate for each row scan is the LV centre x-coordinate. The starting y-coordinate is one below the LV centre y-coordinate. The first minimum encountered along each row is identified as the septal point for that row. Due to the anatomy of the heart, the shape of the normal patient's septum will exhibit some curving in below the LV. This means that the points identified as minima in the row scans will generally move closer and closer towards the LV centre x-coordinate, as the rows farther towards the bottom of the heart are scanned. Once a row is reached where there is no clearly defined minimum (ie. a minimum identified at, or within 2 pixels of the LV centre x-coordinate), the horizontal scanning is stopped. Using the identified septal point from the previous row scan as a starting point, an artificial septum is traced out as a straight line at a 20 degree angle to the vertical, and moving down and to the right. Since the starting point of this line is the last clearly identified septal pixel, the artificial line lies underneath the LV proper, and hence the actual angle of the artificial line is not of critical importance. This artificially defined portion of the septum will consist of only a few pixels. The septal points identified using the minimum method are joined by linear interpolation. The rest of the defined septal points are present for

each row, thus linear interpolation is unnecessary. Finally, the right ventricle is stripped from the image. Figure 3.12 displays the results of this routine on a sample image set.

The horizontal scanning approach is used on a portion of the septum which may not exhibit a distinct circular shape around the identified LV grayscale maximum, and therefore first minimum technique (as described in the previous section) would not operate exactly as desired. For instance, the first minimum technique located minima in the lower portions of the septum which did not satisfactorily correspond with manual definitions.

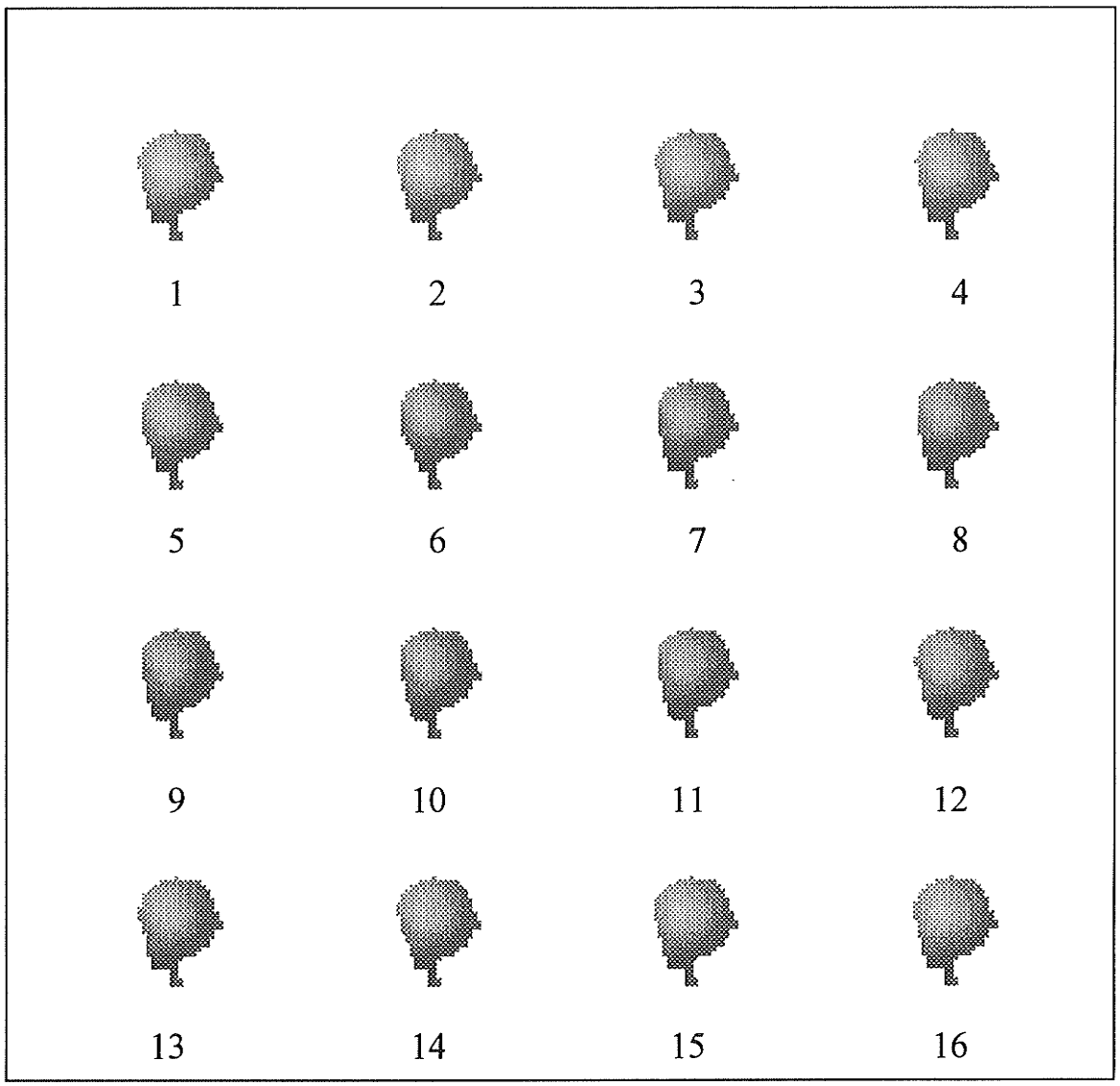

Figure 3.12: Results of minimum/horizontal scan septum identification routine on a 16 frame example image set.

3.3.3 Results

All three methods were employed on a set of ten studies (each study from a different patient). Figures 3.10, 3.11, and 3.12 illustrate the three methods applied to the same image set. It may be observed that the first derivative technique defines a very 'tight' LV boundary, that is, close to the LV centre. The first minimum method works well for the septum region directly between the LV and RV and gives a relatively 'looser' fit compared to the first derivative, the boundary tends to become lax at the bottom of the LV, possibly overlapping the RV in some instances (unwanted). The minimum/horizontal scan method results in a loose fitting contour at the top of the septum, as well as a loose contour at the bottom of the LV, but not overlapping the RV region. The loose fitting contour at the bottom of the LV generally allows for a better LV contour fit, based on this visual examination and comparison to the contours defined in the manual analysis. Therefore, the minimum/horizontal scan method has been incorporated into the fuzzy clustering LV detection algorithm.

3.4 Second Clustering

3.4.1 Features Used

The clustering algorithm is applied a second time on each of the 16 individual image frames, as opposed to the first application which was applied only to the phase image for ventricles identification. Only data from the remaining ventricles region, following the removal of the right ventricle as described previously, is utilized in this second clustering. The input vector for each pixel now consists of three features. The prime component is the grayscale value of the pixel, while the second and third components are the x- and y-coordinates of the pixel. If only grayscale data were used in the clustering routine, the result would be a thresholded image. Utilization of the geometric information induces a spherical shape (perfectly spherical never occurs, but generally a slight ellipse is produced) on the clustered data, which corresponds to the expected profile shape of the LV in the LAO view.

The features are normalized in a manner similar to that performed in the initial clustering. The x- and y-coordinate data, as well as the grayscale data, are normalized by their median values. Weighting factors for the x- and y-coordinate data are restricted to be the same, and are chosen to be 1.0, for reasons described previously described in section 3.1.4. The weighting for the grayscale data is found through an optimization process, described in detail in section 4.1.

3.4.2 Left Ventricle Region of Interest

The second clustering application results in the given image frame data being grouped into two separate clusters, as demonstrated in Figure 3.13. In the normal heart image, one of these clusters corresponds well with the LV, while the other cluster forms a narrow band of pixel data surrounding the LV cluster in a crescent shape along the right and lower edges (in the image). This crescent shaped area is assumed to be signal originating from blood volume external to the heart. There also exists a small territory of unclassifiable pixels which lie between the two identified clusters. This thin region is generally 1-2 pixels in width, where the membership function is considered to be borderline between the two clusters. These pixels are not considered to be a part of either identified cluster.

To distinguish which data cluster corresponds to the desired LV region of interest, the cluster centre vectors are examined. The discriminating feature is the grayscale component of the cluster centres. The LV ROI's cluster centre will possess a higher value for the grayscale component than the external cardiac region. Identification of the LV ROI becomes a matter of choosing the cluster with the highest grayscale component in the cluster centre vector.

The identified LV boundary may not be a smooth convex curve. A morphological closing is performed on the LV ROI with a 2×2 structuring element to smooth the LV boundary. Essentially this processing removes contour protuberances

consisting of single pixels. In this fashion, a smooth LV ROI is defined in each image frame, based on the results of the second application of the clustering algorithm.

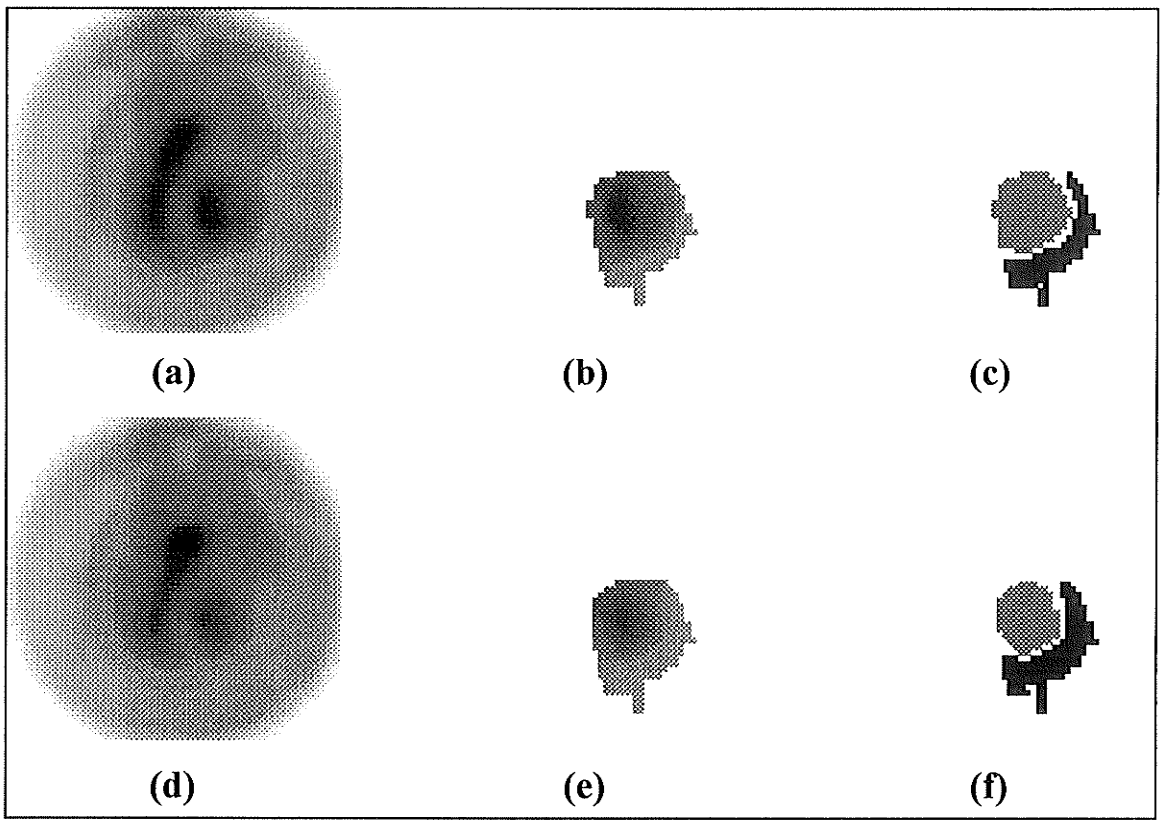

Figure 3.13: (a) End-diastolic frame of example image set, (b) corresponding input image for second clustering application, (c) resulting clusters, (d) end-systolic frame of example image set, (e) corresponding input image for second clustering application, and (f) resulting clusters.

3.4.3 Calculation of Ejection Fraction

After identifying a LV ROI in each image frame, the pixel grayscale values within each ROI may be summed to yield a time activity curve. Multiplying the background activity per pixel by the number of pixels populating each LV ROI produces the appropriate background correction required for each point in the TAC. Subtracting these correction values from the original TAC results in a background-corrected TAC from which the ejection fraction may be calculated.

A smooth curve is fitted to the TAC before the ejection fraction calculation proceeds. This is done because statistical fluctuations limit the accuracy of quantities derived directly from the cardiac TAC. This may not be obvious in this work, due to the use of spatially and temporally smoothed data, but should definitely be a concern when using unfiltered data sets. A common method of fitting the TAC is with a truncated Fourier series. Work by Bacharach *et.al.* (1983) and Mukai (1983) indicate that the optimal number of Fourier harmonics to fit to the TAC is 2 (for low end-diastolic counts) or 3 (for high end-diastolic counts). Recalling equation 3.1 and limiting the expansion to 3 harmonics:

$$TAC(k) = a_0 + \sum_{h=1}^{3} a_h \cdot \cos\left[\frac{2\pi h(k-1)}{k_{\max}} + \phi_h\right] \tag{3.5}$$

$$\text{where } \phi_h = TAN^{-1}\left[-\frac{\sum_{k=1}^{k_{\max}} \sin\left[\frac{2\pi h(k-1)}{k_{\max}}\right] \cdot TAC(k)}{\sum_{k=1}^{k_{\max}} \sin\left[\frac{2\pi h(k-1)}{k_{\max}}\right] \cdot TAC(k)}\right], \text{ phase value of harmonic} \tag{3.6}$$

$$a_0 = \frac{1}{k_{\max}} \sum_{k=1}^{k_{\max}} TAC(k), \text{ zeroth amplitude term} \tag{3.7}$$

$$a_h = 2 \sum_{k=1}^{k_{\max}} \cos\left[\frac{2\pi h(k-1)}{k_{\max}} + \phi_h \right] \cdot TAC(k), \text{ amplitude of harmonic term} \tag{3.8}$$

and h = harmonic number

k = frame number

$k_{\max}$ = total number of frames.

Therefore the TAC curve for the LV is fitted by expansion of equation 3.5, with the terms derived through equations 3.6-3.8 above. From this fitted TAC, the ejection fraction may be calculated by equtaion 5.2. A comparison of the original TAC to the fitted TAC for a sample image set is given in Figure 3.14.

This method of smoothing the TAC by Fourier curve fitting is not performed by the manual technique used at the Health Sciences Centre. The manual technique applies a linear interpolation routine between two TAC's (the manually drawn end-diastolic and end-systolic ROI's each giving one TAC) to give a final estimate of the left ventricle TAC. However, this procedure does not accomplish a curve fitting of the data. The semi-automated technique does employ a Fourier curve fitting of the TAC, retaining the first six harmonics with weightings of 1.0, 1.0, 1.0, 0.75, 0.50, and 0.25 respectively. This is equivalent to a low pass filter.

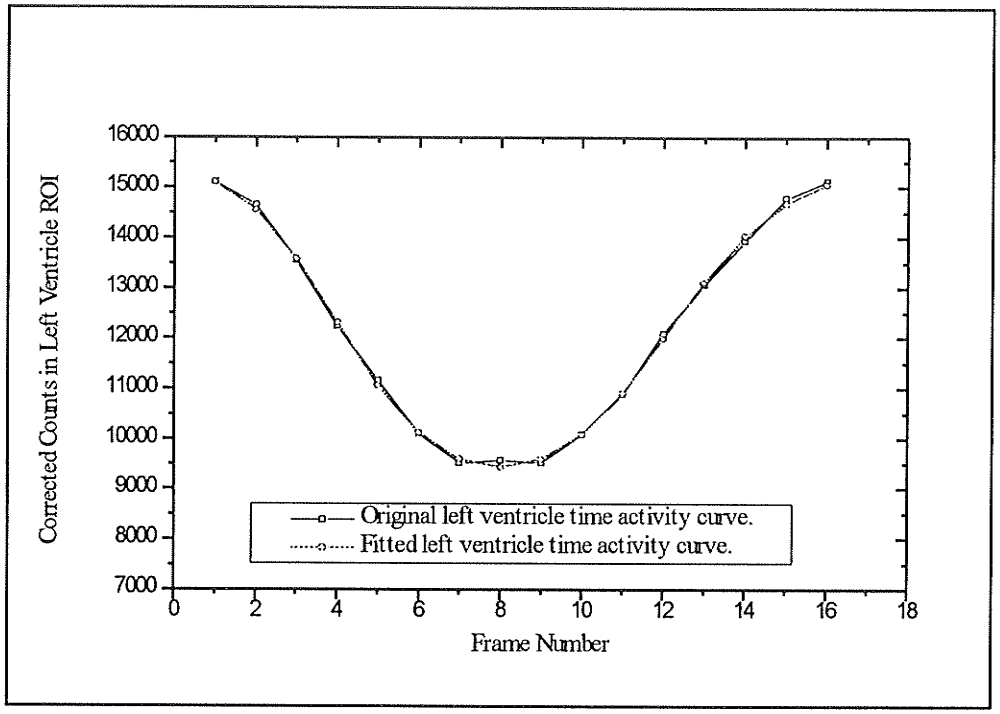

Figure 3.14: Original and Fourier fitted time activity curves for example image set (which has already been spatially and temporally filtered).

3.5 Background Estimation

3.5.1 Introduction

The time activity curve of an LV is composed of two main components: 1) activity originating from within the LV volume, and 2) activity observed within the LV region but actually originating external to the LV volume. The second component is known as background activity. The TAC of the LV must therefore be corrected for the background before calculation of the ejection fraction.

Several factors contribute to the background activity: (a) vasculature lying in front of and behind the LV will contribute to the counts observed in the LV, (b) scattered photons originating externally to the LV may be observed to emanate from within the LV region, and (c) there is also the concept of 'virtual' background introduced by Green et. al. (1978). This concept was developed to describe background sources which arise not from radioactivity external to the LV, but which can be attributed to violations of the two major assumptions of gated blood pool imaging as discussed on page 1. These are: 1) the externally observed LV count rate is absolutely proportional to LV volume, and 2) all cardiac cycles are mechanically identical. The first assumption is violated due to the effects of attenuation of the signal originating in the LV, and the second is violated due to natural variation of the cardiac cycle. Both of these violations result in a decrease in measured EF, which is equivalent to an increase in the 'virtual' background activity.

The background originating entirely outside the LV may, in principle, be corrected for by subtracting a suitably estimated background from each pixel within all LV regions-of-interest. The virtual background sources cannot be corrected for so easily, but the magnitude of their effect is much less than the external background sources (Green et. al., 1978).

3.5.2 Methods of Estimating Background Activity

Several techniques for estimating background activity have been proposed in the literature. All of these techniques assume that the background activity is spatially invariant (which is not true), due to the extreme difficulty in developing a spatially variant model. A list of proposed techniques in the literature follows:

(a) 50% of the counts in the ventricular region of interest at end-systole (Slutsky, *et.al.*, 1980),

(b) the counts in the systolic frame in the region lying between the end diastolic and end systolic outlines (Slutsky et. al., 1980),

(c) the average activity of the pixels along the inferior and left sides of a rectangle defined to encompass both ventricles (Merrick, 1984),

(d) a vertically oriented rectangle (3 pixels wide by 15 high) lying immediately adjacent to the LV region of interest in the end systolic frame (Taylor et. al., 1980),

(e) a crescent shaped region 3 pixels wide, lying 2 pixels outside the LV contour on the end systolic frame, between 3 and 6 o'clock relative to the LV centre (Reiber et. al. 1983),

(f) selecting an 'optimal' background region from six automatically generated regions in the directions of 1 through 6 o'clock with respect to the LV centre on the basis of minimal variance in the background TAC and lowest mean activity level (Reiber, 1985),

(g) a manually defined crescent shaped region 2-3 pixels wide in the end systolic frame, generally chosen in a region of low activity 2 pixels outside the LV region of interest (HSC technique).

3.5.3 Anatomical Landmarks in Background ROI's

With any background correction technique where a region of interest is defined, care must be taken not to include anatomical features unrepresentative of the true background. The descending aorta is generally visible in an LAO gated blood pool scan as a narrow region of increased activity lying to the right of the left ventricle, extending vertically through the image. Often the spleen may demonstrate higher activity due to blood flow to that organ which is located below and to the right of the left ventricle in the image. The inferior vena cava may be visible as a narrow region of increased activity extending below the right ventricle chamber to the bottom edge of the image. Due to anatomical variation between patients, the position of this vein may lie underneath the septal region, or even the left ventricle. Since this vessel is buried deeper than the descending aorta, it is not as distinct a feature. A choice of background region which includes any or a portion of these features which display increased activity will result in an overestimate of background. This will also cause the ejection fraction to be overestimated.

An area of lower than 'true' background activity may occur in cases where the patient is exhibiting stomach gas. The stomach is located slightly below and just to the right of the left ventricle. Gas trapped in the top of the stomach may cause a region of

decreased activity in the image due to the displacement of background blood containing tissue by non-active gas. This is an uncommon situation. However if the defined background region includes a portion of this feature, the background activity and therefore the ejection fraction will be underestimated.

3.5.4 Automated Background ROI Selection

It was decided that the background estimation method employed should simulate the manual technique used by the HSC, since the manual technique results would be acting as the standard of comparison. The adopted algorithm traces rays at 5 degree intervals from 0° to 225° with respect to the identified LV centre in the end-systole image frame only (0° corresponds to 12 o'clock position). The grayscale values of each pixel are examined along every ray, and the minimum pixel lying outside the left ventricle contour but within four pixels of this boundary is selected for further processing. The minimum pixel as opposed to simply a set pixel number is used here to ensure that the following region-growing algorithm is receiving at the very least a local minimum. In this manner, 46 pixel coordinates are chosen (one for each ray traced) to be passed to a region-growing routine, each pixel acting as a 'seed' point. A region-growing routine is an image processing technique which expands pixels or subregions into larger regions. Each of the 46 'seed' points are used as input to the algorithm and from this 46 regions are grown. Growth of the regions occurs by appending to the seed point those neighbouring pixels possessing similar properties. The property examined in

this case is the grayscale value of the pixel. Neighbouring pixels are added to the region if their grayscale is equal to or lower than the grayscale of the seed point. The algorithm stops when the region size reaches 40 pixels. The region size is set as an input parameter, and has been chosen to correspond approximately to the size of manually chosen regions. If the region size fails to grow to 40, and there are no more neighbouring pixels which are of equal or lower grayscale than the seed point, then this limiting grayscale value is increased by one unit, and the growth initiated again. This process is repeated until the region size equals or exceeds 40 pixels. The resulting region is a local grayscale minimum adjacent to the given seed pixel. In order to simulate the crescent shape of the manually chosen background regions, geometric boundary restrictions were imposed during each application of the region-growing routine. These limitations were defined in terms of radius from the left ventricle centre. The growing regions were forced to lie between 2 and 6 pixels outside the LV contour as measured along the radial ray. These boundary conditions resulted in crescent shaped regions of interest, as desired.

This processing results in 46 defined background regions, one for each seed point. For each region, the average activity per pixel is calculated by summing the grayscale values and dividing by the number of pixels within the region. Neighbouring regions exhibited significant overlap, and background activity calculated from neighbouring regions is similar in magnitude. However, when viewed altogether, the regions varied significantly depending on location (for example between 136 counts/pixel at 40° to 89

counts/pixel at 160°). The region possessing the lowest average activity per pixel is chosen as the estimate of the background activity (see Figure 3.15 below).

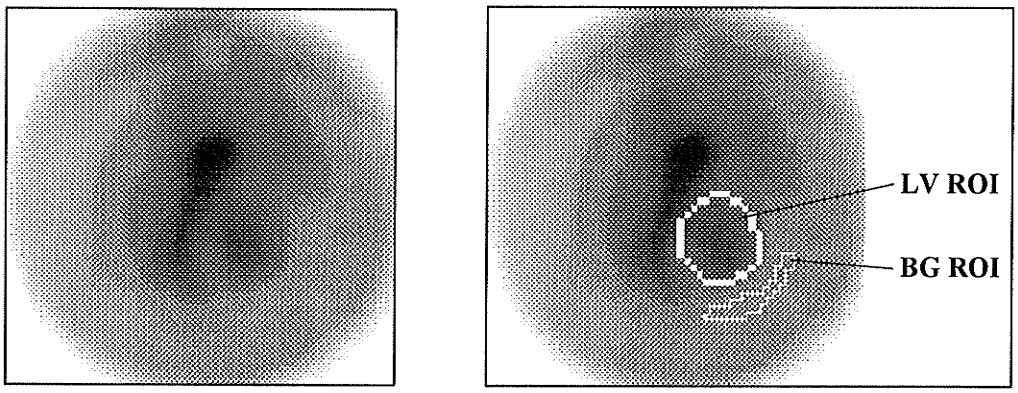

(a) (b)

Figure 3.15: (a) End-systolic frame, and (b) end-systolic frame with left ventricle region of interest (LV ROI) and background region of interest (BG ROI) defined.

This attempts to simulate the choice of a region of low activity in the HSC technique. Due to the choice of the minimum activity per pixel, as well as the method by which the background regions are grown, it is felt that if the estimation differs from that of the HSC technique, the difference will be an underestimation of the background. This is advantageous when one considers the work of Grove, *et.al.*, 1986. They find, using ideal geometrical models, that in situations where the background is overestimated, the error in ejection fraction may be very large. However, when the background is underestimated, the resulting error in ejection fraction is smaller (relative to an equal overestimation), as illustrated in Figure 3.16. Thus, if the background estimate is not accurate, it is

preferable to make an underestimate since an error in that direction will have less impact on the ejection fraction.

It is emphasized that this work is not advocating the use of a zero background correction, as suggested by others (Gandsman, 1982; Gandsman, 1990). The work by Grove is interpreted here as merely suggesting that an underestimation of background will result in less error in the calculated EF than an overestimation. Idealizations in Groves' work, such as a spherically shaped heart and correctly defined LV ROI's at both ED and ES, make generalizations of absolute magnitudes (observed in Figure 3.16) to clinical situations difficult.

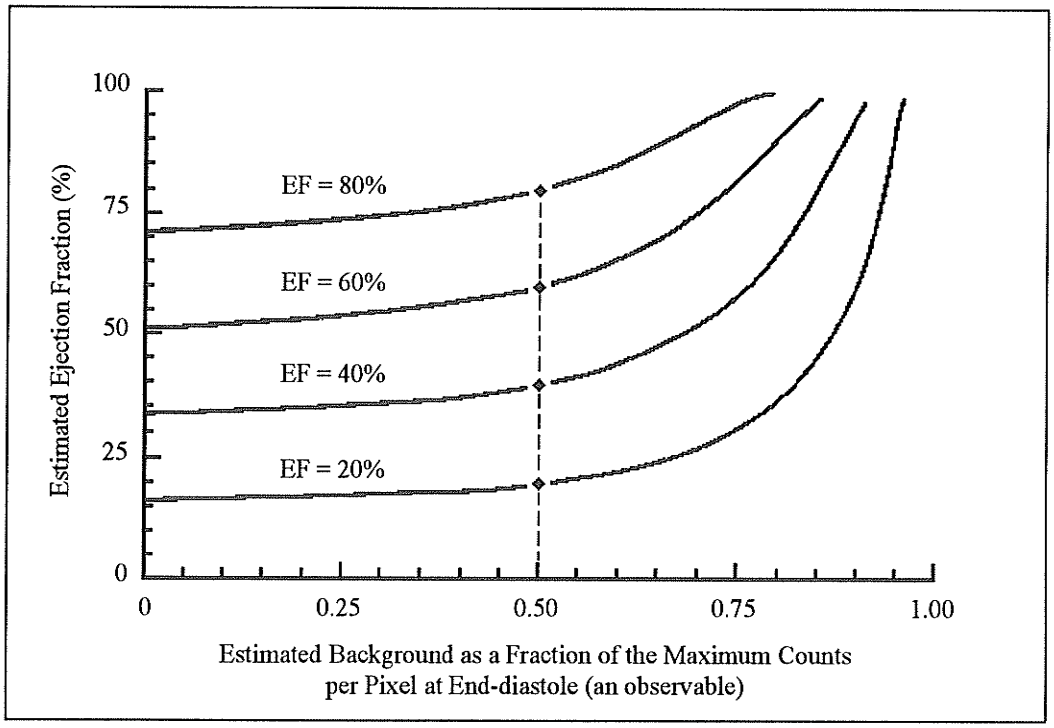

Figure 3.16: The effect of an error in background correction estimation on calculated ejection fraction for four values of true ejection fraction (EF = 20, 40, 60, and 80%) with the true background defined as 0.50 of the maximum counts per pixel at end-diastole [adapted from Grove, *et.al.*, 1986].

The effect of the number of pixels defining the background region was explored in a set of ten images. The number of pixels composing the background region was increased from 10 to 80 in steps of 5, and the resulting ejection fraction examined. The results are presented in Figure 3.17. It is shown that in all of the test cases, the larger the background region, the higher the background activity estimate and therefore the higher the ejection fraction. In most of the test cases, the ejection fraction is affected very little by the size of the background region, demonstrating that the exact number of pixels comprising the region is not crucial. The variation in the measured EF due to the choice of the background region size is within ±1.5% as observed in the analysis of the ten image test set in Figure 3.17.

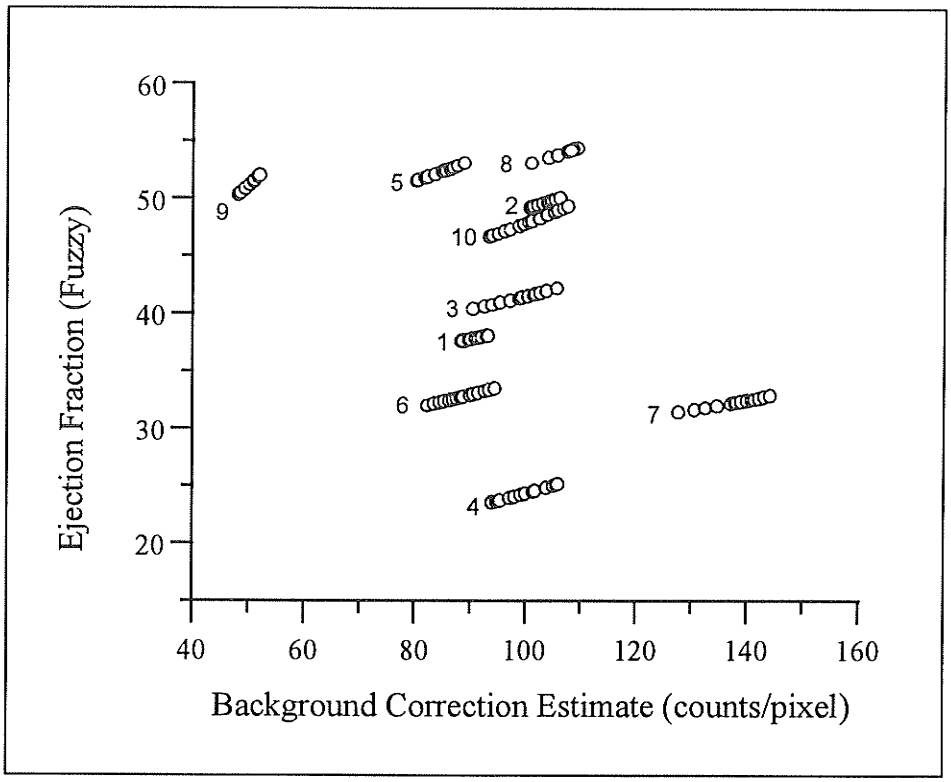

Figure 3.17: Effect of background correction estimate on calculated ejection fraction for ten image sets (as labeled 1-10). The data points are attained by varying the size of the background region of interest from 10 to 80 pixels in steps of 5 (thus yielding 15 data points per image set).

References

Cardiology: an illustrated text/reference. Ed. Chatterjee, K., M. D. Cheitlin, J. Karliner, et al. Philadelphia: J.B. Lippincott Company, 1991. 1.2-1.18.

Bacharach, S.L., M.V. Green, D. Vitale, et al. "Optimum Fourier Filtering of Cardiac Data: A Minimum-Error Method: Concise Communication." Journal of Nuclear Medicine 24 (1983): 1176-1184.

Boudraa, A.E.O., J.J. Mallet, J.E. Besson, et al. "Left Ventricle Automated Detection Method in Gated Isotopic Ventriculography Using Fuzzy Clustering." IEEE Transactions on Medical Imaging 12 (3) (1993): 451-465.

Gandsman, E. J., D. L. North, and E. W. Bough "The Nature of the Background in Radionuclide Ventriculography: Deductions From the Mathematical Behaviour of the Ejection Fraction" Physics in Medicine and Biology 35 (11) (1990): 1467-1476.

Gandsman, E. J., R. S. Schulman, I. B. Tyson, et al. "Calculation of the Left Ventricular Ejection Fraction by Gated Radionuclide Angiography Without Direct Background Correction." Radiology 144 (2) (1982): 377-381.

Green, M. V., S. L. Bacharach, M. A. Douglas, et al. "Sources of Virtual Background in Multi-Image Blood Pool Studies." Nuclear Cardiology: Selected Computer Aspects. Ed. Anonymous. New York, NY: The Society of Nuclear Medicine, Inc., 1978. 97-106.

Grove, D.E., R.A. Stein, and J. Nosil. "Effect of background correction on left ventricular ejection fraction calculation through analysis of a simple cardiac model." Medical Physics 13 (6) (1986): 949-953.

Itagaki, H. "Improvements of Nuclear Magnetic Resonance Image Quality Using Iterations of Adaptive Nonlinear Filtering." IEEE Transactions on Medical Imaging 12 (2) (1993): 322-327.

Merrick, M. V. "The heart." Essentials of Nuclear Medicine. Ed. Anonymous. New York: Churchill Livingstone, 1984. 72-107.

Mukai, T., N. Tamaki, Y. Yonekura, et al. "Optimum Order Harmonics of Fourier Analysis in Multigated Blood-Pool Studies." Journal of Nuclear Medicine 24 (5) (1983): P17(Abstract)

Palmer, E. L., J. A. Scott, and H. W. Strauss. Practical Nuclear Medicine. Philidelphia: W.B. Saunders Company, 1992. 1-399.

Pratt, W. K. "Morphological Image Processing." Digital Image Processing. Ed. Anonymous. 2nd ed. New York: John Wiley & Sons, Inc., 1991. 449-490.

Reiber, J.H.C. "Quantitative analysis of left ventricular function from equilibrium gated blood pool scintigrams: an overview of computer methods." European Journal of Nuclear Medicine 10 (1985): 97-110.

Reiber, J.H.C., S.P. Lie, M.L. Simoons, et al. "Clinical Validation of Fully Automated Computation of Ejection Fraction from Gated Equilibrium Blood-Pool Scintigrams." Journal of Nuclear Medicine 24 (12) (1983): 1099-1107.

Slutsky, R., M. Pfisterer, J. Verba, et al. "Influence of Different Background and Left-Ventricular Assignments on the Ejection Fraction in Equilibrium Radionuclide Angiography." Radiology 135 (June) (1980): 725-730.

Sychra, J.J., D.G. Pavel, and E. Olea. "Fourier Classification Images in Cardiac Nuclear Medicine." IEEE Transactions on Medical Imaging 8 (3) (1989): 270-275.

Taylor, D.N., N.W. Garvie, B. Chir, et al. "The Effect of Various Background Protocols on the Measurement of Left Ventricular Ejection Fraction in Equilibrium Radionuclide Angiography." British Journal of Radiology 53 (1980): 205-209.

Valette, H.B., M.H. Bourguignon, P. Merlet, et al. "Improved Detection of Anterior Left Ventriuclar Aneurysm with Multiharmonic Fourier Analysis." Journal of Nuclear Medicine 31 (1990): 1303-1306.

Chapter Four: ANALYSIS

4.0 Introduction

During the application of the fuzzy clustering algorithm, many parameters must be defined. These include the fuzzy exponent weighting values (see section 1.3.4) and the input vector weighting factors (section 3.1.3 and section 3.1.4). In addition, the δ factor in the isolation image calculation (section 3.1.2) and the decay value (section 3.1.1) must also be defined prior to calculation of the ejection fraction.

Ideally, these values should be set at the most stable operating points to reduce the effects of these choices on the resulting EF value. An optimisation process for identifying the most stable set of operating parameters for a test set of 10 studies is described in this chapter.

Self attenuation due to the blood volume itself is generally unaccounted for in the normal estimation of EF from gated blood pool images. The fact that the blood volume is a distributed source which also acts as an attenuator results in a slight overestimation of EF unless a correction is made. A computer simulation has been created to estimate the magnitude of this problem, and the results lead to a novel method of correcting an EF estimate for self attenuation by the blood volume. This chapter also discusses the computer simulation and results, in addition to the correction method devised.

4.1 Optimisation Process

4.1.1 Introduction

The fuzzy *c*-means algorithm as applied to left ventricle detection requires several parameters to be specified during the course of execution (refer to sections 1.3.4, and 3.1-3.5). There appears to be no theoretical or computational evidence which distinguishes optimal values of these parameters. The best strategy for selecting optimal parameters seems to be based on an experimental approach (Bezdek, 1984). This consists of identifying the most stable operating point by examining output for a discrete range of inputs for each parameter.

Many parameters have been defined throughout the algorithm developed in Chapter Three. Some of these will have a greater effect than others, on the resulting EF. The most important parameters in terms of effect on EF were selected for optimisation. It is important to note that the optimisation process assumes these parameters are independent, which may not necessarily be the case. The optimised parameters include:

1) decay parameter of the phase image
2) isolation parameter (δ)
3) fuzzy weighting exponent used for first clustering (m_1)
4) feature weighting factor used on first clustering input vectors (w_1)
5) fuzzy weighting exponent used for second clustering (m_2)
6) feature weighting factor used on second clustering input vectors (w_2)

This section will discuss in further detail the method used to optimise these parameters and the results of this optimisation process. An estimate for the uncertainty resulting from the use of a parameter set optimised for several images as opposed to a parameter set optimised to a single image will be described in section 5.1.

4.1.2 Optimisation Method

The choice of a global set of optimised parameters has been performed in a two step process. Given a test group of 10 normal heart studies, each image set was initially analysed to achieve stable parameters for that particular study. The ten sets of individually optimised parameters were then analysed to yield a single, global set of parameters optimised for all 10 studies. Thus, the optimisation process functions to identify stable operating points, which may not necessarily be the most correct ones in terms of output EF. Optimisation to achieve stability during operation is an attainable goal whereas optimisation to achieve the correct EF is virtually impossible, since no technique offering 100% accuracy currently exists.

An initial analysis during which the parameter values for all 10 studies were investigated enabled the recognition of clinically useful ranges of the parameters involved. By clinically useful, it is meant that the LV ROI identified via the algorithm seems to coincide reasonably with the LV structure observed. Optimisation was then concentrated within a liberal estimate of range values. The parameters were optimised

one at a time, and in the same sequence they were input during the program execution. Once identified, the value was fixed during optimisation of the subsequent variables. Background correction was not employed during the entire optimisation process, since only the relative stability of the resulting EF was examined, and not the absolute magnitude. Exclusion of the background correction should increase the reliability of the optimisation process, since it is not possible to optimise the background estimate in the same sense as the previously mentioned parameters. This is because the background activity is not determined through implementation of the fuzzy clustering algorithm, while the optimised parameters are all involved in the direct execution of the fuzzy clustering algorithm. The subroutine determining the background activity estimate merely utilizes the final clustering results of the LV contour definition in the end-systolic frame (as described in section 3.5.4).

The parameter being optimised was stepped throughout the previously identified useful clinical range in small increments, in order to identify local trends in the effect on EF. At each step, the ejection fraction was calculated via the fuzzy process. A graph of EF as a function of the parameter value proved useful for determining the range of values over which the parameter exhibited stability. The range of stability was determined visually from each graph of EF versus parameter, and quantitatively consisted of any region which displayed less than a 1% variation in EF as compared to surrounding regions. To further ensure stability, the 'edge' points of each identified stable range were not included in defining the stable range. Thus, the minimum stable region size consisted of three adjacent points, of which only the centre point would be used in defining the

region. A stable range was identified for every parameter described in section 4.1.1, and for every image set. It was observed in several cases that a parameter could exhibit more than just a single region of stability, so all regions were recorded. Figure 4.1 displays the variation of resulting EF as a function of the fuzzy weighting exponent used for the second clustering application (m_2) on a test study. Note that three stable regions defined as above are evident from this graph, over the range examined. These regions would include the values covering 1.65-1.80, 2.00-2.20, and 2.35.

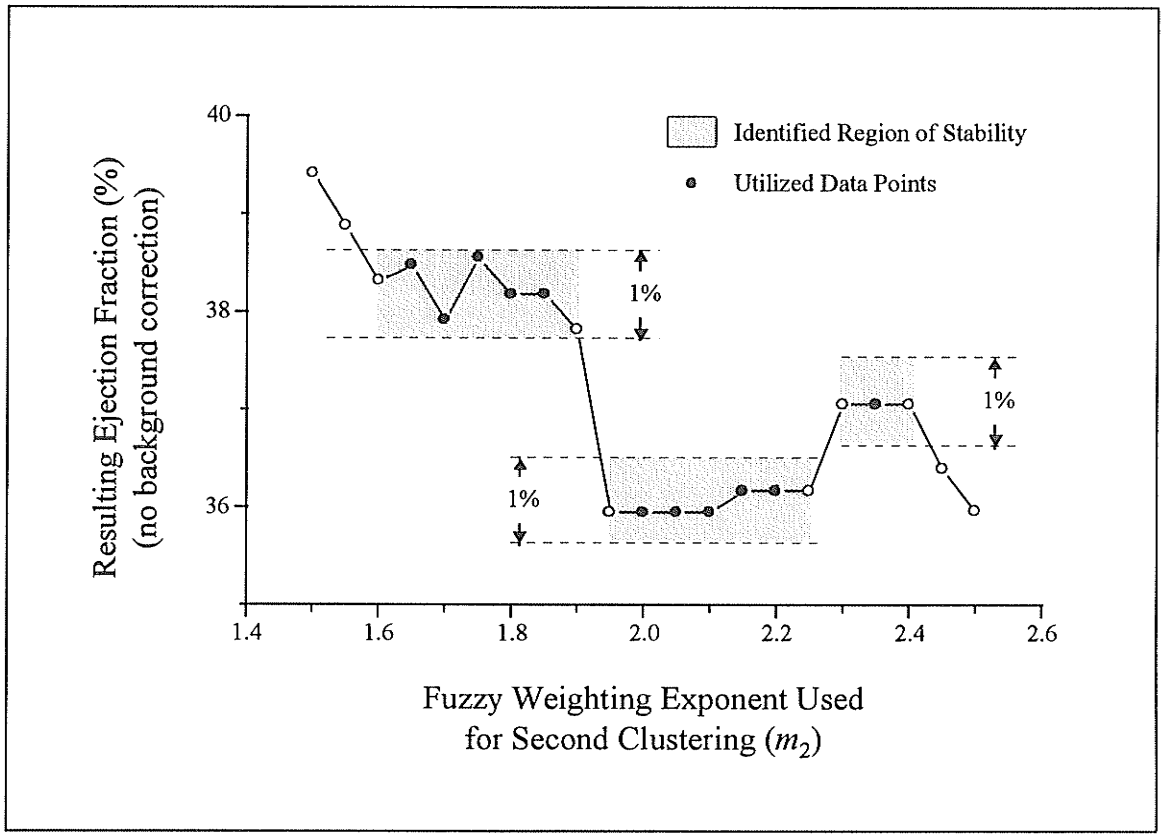

Figure 4.1: Variation of ejection fraction (uncorrected for background) with the fuzzy weighting exponent used for the second clustering application (m_2) on a test study. Three regions of stable operation are apparent from this graph: values of 1.65 - 1.80, 2.00 - 2.20, and 2.35 inclusive.

The weighting factor effect on EF in both the first and second fuzzy cluster applications results in a region of high stability (essentially no variation in EF) when the weighting factor reaches a certain magnitude. Once this plateau is reached, it signifies the weighted input parameter is dominant over the unweighted inputs. This does not mean that the unweighted inputs are not affecting the output. The stability demonstrates that the weighted parameter is the primary distinguishing feature in this range as intuitively expected, and desired (recall section 3.1.3). An example of this type of stable region for the grayscale weighting used in the second clustering application is given in Figure 4.2.

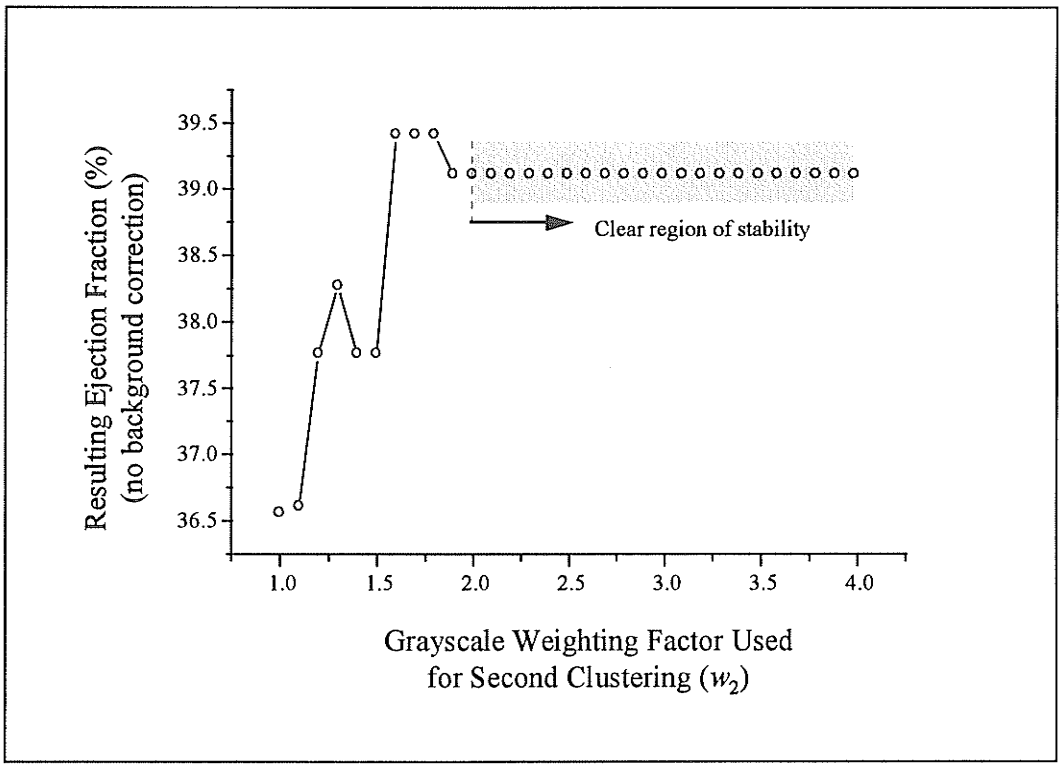

Figure 4.2: Variation of ejection fraction (uncorrected for background) with the grayscale weighting factor used for the second clustering application (w_2) on a test study. A single distinct region of stable operation is apparent from this graph: values of 2.0 and upwards.

The second step of the optimisation process entailed analysing the parameter ranges determined during the first step. The frequency of occurrence of each discrete parameter point over a region of stability was registered for all 10 image sets. These data could then be viewed in histogram format, for easy analysis (see Figure 4.3 for an example of the first fuzzy weighting exponent, m_1). The frequency of stable occurrences versus the actual value of the parameter yielded a useful summary of data from which the globally optimum parameter may be selected. The selection process consisted of choosing the most frequently occurring stable value of each parameter. If two neighbouring parameter points had equal frequencies of occurrence, the average parameter value would be designated as optimal. When two non-neighbouring parameter points had equal frequencies of occurrence, the value with the higher nearest neighbour stable frequencies was chosen as the optimal parameter. It should be noted that this technique is based on a 'modal' approach as opposed to an 'average' approach. This method was utilized because an average optimised value may not occur frequently in individual image sets, and thus provide stable values for fewer image sets than a parameter choice based on frequency of occurrence.

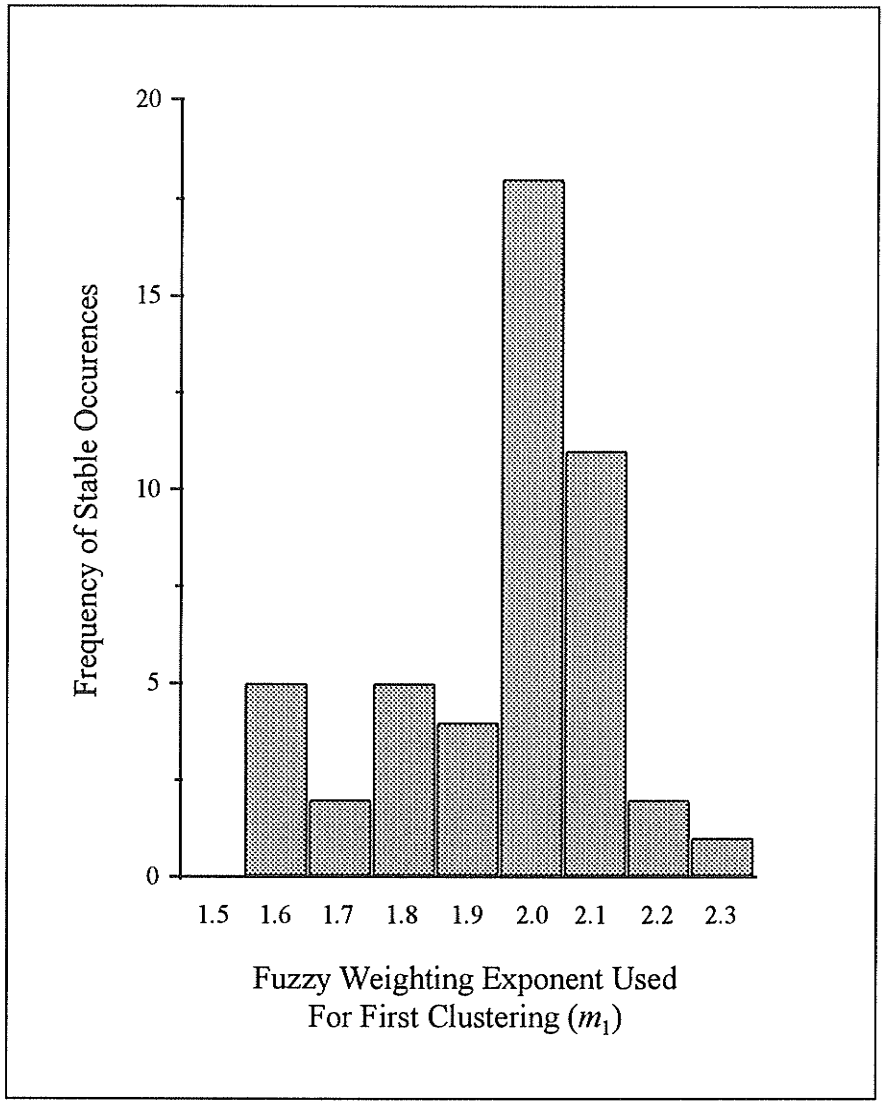

Figure 4.3: Histogram of stable occurrences of the fuzzy weighting exponent used for the first clustering (m_1), as compiled for 10 image sets. The most frequently occurring value is the 2.00-2.10 bin, thus 2.05 is taken as the optimal value.

The histograms for each optimised parameter are presented in Appendix A, and are discussed now. The decay parameter has a wide range of stable values, with an average value over the four highest bins of 32.5. The raw data suggests that the decay

parameter value has little effect on EF. The isolation δ parameter demonstrats two dominant bins, those of 30 and 35. The average of these two is taken as the optimal value, at 32.5. The fuzzy weighting exponent for the first clustering, m_1, displays a single dominant bin with a value of 2.05 (since the bin width is 2.0 - 2.1, the representative value is 2.05). Examination of the phase and isolation weighting factor, w_1, reveals the minimum stable operating value to be 3.2. This histogram must be interpreted carefully. It demonstrates that the output EF of six study sets are stable for values of 2.1 and higher, seven study sets are stable for values of 2.3 and higher, eight study sets are stable for values of 2.5 and higher, nine study sets are stable for values of 3.0 and higher, and all ten study sets are stable for values of 3.2 and higher. Thus the value of 3.2 is chosen to ensure a stable region over *all* sample study sets. The fact that 3.2 is greater than the minimum value stable value necessary in nine of the study sets is inconsequential, since the EF output does not fluctuate once the minimum plateau value is reached (as demonstrated in Figure 4.2). However, an arbitrarily large value should not be chosen since it would make the contribution from the unweighted inputs negligible. A similar argument may be utilized for the grayscale weighting factor, w_2, with the optimal value chosen as 3.2. The histogram describing the second fuzzy weighting parameter, m_2, possess a bimodal distribution. That is, there are two regions of frequent stable occurrences, one around 1.6, and the other around 2.1. Due to the greater magnitude of stable occurences, as well as the wider range of stability (higher surrounding bins), the 2.1 bin was selected. Thus, the global m_2 parameter representing all ten study sets was chosen to be 2.15 (since the bin covers values 2.10-2.20).

Therefore, through the above processing steps a set of globally optimised parameters has been found. This set of parameters is representative of the 10 image sets employed in the optimisation procedure, not just a single image set. The globally optimised set of parameters has been used to reanalyse each of the 10 image sets, as described in 5.1.1. The results of the optimisation process are presented below in tabular format:

Parameter Description	Optimised Value (for 10 image sets)
decay parameter	33
isolation parameter (δ)	35
fuzzy weighting exponent (m_1)	2.05
phase and isolation weighting factor (w_1)	3.2
fuzzy weighting exponent (m_2)	2.15
grayscale weighting factor (w_2)	3.2

Table 4.1: Results of parameter optimisation employing data collected from ten studies.

4.2 Attenuation Effects

4.2.1 Introduction

A basic assumption in radionuclide ventriculography is that the external count rate observed in the LV by the gamma camera is absolutely proportional to the LV volume. However, due to photon attenuation (and scatter) by the various tissues lying inbetween the source activity and the gamma camera, this relationship is non-linear (Dell'Italia, 1985; Links, 1982; Nickoloff, 1983; Rabinovitch, 1984). The LV blood volume itself also constitutes an attenuation and scattering medium. Hence, source points lying further away from the camera will suffer more attenuation due to the larger amount of intermediate material. Therefore a gradient of detection sensitivity exists along the line of sight of the gamma camera through the LV (Green *et.al.*, 1978). This implies that the observed LV in gated blood pool scans is anteriorly weighted in the camera viewing direction (ie. voxels closer to the camera contribute relatively more signal than voxels further away). To illustrate the effect the attenuation will have on the detected signal, consider two point sources of equal activity, one at the apex of the LV, and the other in the back of the LV at the mitral valve, each point lying along the same line of view with respect to the gamma camera. If average cardiac dimensions of 7.5 cm long axis, 6.4 cm short axis for end-diastole and 5.5 cm long axis, 3.4 cm short axis for end-systole (Cardiac Imaging: a companion to Braunwald's Heart Disease, 1991) and an attenuation coefficient equal to the broad beam value for 140.5 keV photons in water

[0.12 cm^{-1}] (Gandesman, 1990) are assumed, the point source at the heart apex will register only ~62 % of the counts emitted by this source if it were located at the skin surface. The point source lying at the mitral valve would register about ~30 % of the skin surface activity. This example illustrates that detection sensitivity may vary by a factor of 2 from the 'front' to the 'back' of the LV.

Cardiac phantom studies were performed by Green *et.al.* (1978) for the purpose of assessing the non-linearity of the counts vs. volume relationship. It was suggested that this relationship depended on viewing angle, absolute end-diastolic volume and EF, and LV shape. Yeh (1981) investigated the attenuation effects within an ellipsoid model and predicted a ~4.5% underestimate of EF. Gandesman (1990) examined the effects of self-attenuation of the blood volume on the calculated EF using spherical and cylindrical models and calculated an apparent underestimation of EF by 2-5%. Although a minor concern in healthy hearts, this effect could give rise to a chronic underestimation of the true EF in dilated and failing ventricles (Green, 1978). These effects are further investigated via computer simulation in this analysis as described in section 4.2.2 below. The work by Green also indicated that the loss of photons originally moving toward the detector may be partially compensated by the detection of photons not initially moving toward the detector but scattered by intervening material into the detector. Owing to this effect, count-volume linearity may be improved in patients over results indicated by in-air phantom studies.

4.2.2 Computer Simulation

In order to achieve a more accurate estimate of the effects of photon attenuation upon EF, a computer model was developed. This simulation allows varying LV contours to be examined, and varying gamma camera angles with respect to the LV long axis. An LV contour shape is defined by an input file containing a set of discrete points representing one-half of the LV contour along the long axis. The computer program then generates the full LV shape by assuming rotational symmetry about the long axis of the LV. Linear interpolation is used to fill in the boundary shape between defined contour points. The coordinate system used is Cartesian, with the x-axis defined as the LV long axis, the y-axis defined as the LV short axis, and the z-axis defined to retain orthogonality (see Figure 4.4). The gamma camera viewing angle and voxel size are set as input values. The voxel size indicates the volume element size which will be examined in the simulation; the smaller the voxel size, the more accurate the simulation results at a cost of increased computing time. The gamma camera angle is converted to a direction vector with length 0.1 mm.

Planar contours of the LV are generated by taking slices in the x-y plane at increments along the z-axis defined by the voxel size. For each slice of LV data, a rectangular region just encapsulating the LV contour is analysed. The x- and y-coordinates are stepped through by increments of the voxel size. Each point is examined to discover if it lies within the defined LV boundary in that plane. If the point is found to be inside the LV, then the length from the point to the LV contour in the direction of the

gamma camera is calculated. This length is used to find the attenuated signal reaching the LV surface from the voxel being examined. For example, considering the attenuation coefficient to be 0.12 cm^{-1} as before, a 5 cm interval of tissue would cause a $[1-\exp(-0.12*5)] \approx 45\%$ reduction of signal. All voxels in the rectangular region encompassing the LV boundary are inspected. Therefore by summing only points lying within the LV and multiplying by the voxel volume, an estimate of the true volume of that LV contour may be achieved. Summing the attenuated signal from all those points within the LV contour and multiplying by the voxel volume will yield an estimate of the effective volume measured at the gamma camera resulting from attenuation of the radioactivity originating in the LV. Figure 4.4 portrays a schematic representation of this computer model.

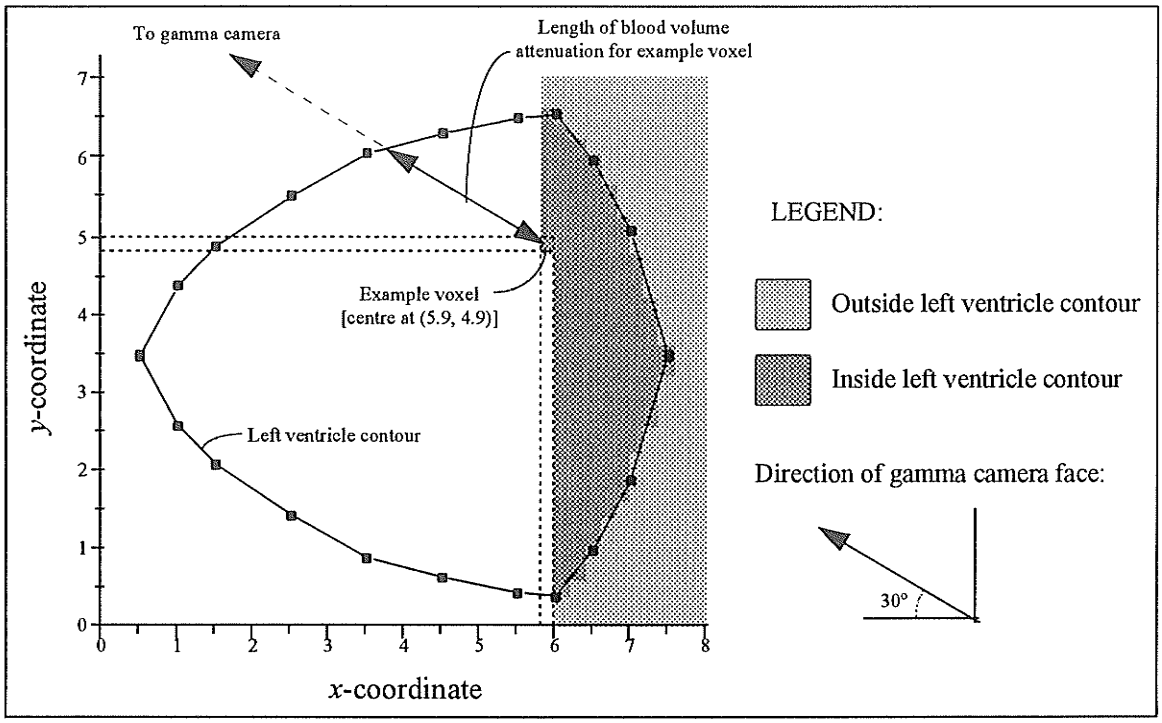

Figure 4.4: Illustration of computer simulation geometry for left ventricle cross section through $z = 0$. User defined input parameters: voxel size = $2\times2\times2$ mm^3, angle of gamma camera line of sight to left ventricle long axis = 30°. The array of voxels is scanned by incrementing down the y-coordinate for an entire column, and repeating this columnar scan for each x-coordinate value (moving in the negative x direction).

By using realistic LV dimensions for both end-diastole and end-systole (Cardiac Imaging: a companion to Braunwald's Heart Disease, 1991) in this computer simulation, the true and apparent LV volumes may be calculated for any orientation of gamma camera angle. In this way, the effect on EF due to attenuation alone may be estimated. Results of the computer simulation on a spherical test contour verify that the model functions properly, through convergence to the true volume of 113.097 cm^3, as demonstrated in Figure 4.5. The slight underestimation (by 3.2%) is expected due to the

linear interpolation between curved surface points resulting in a 'connect-the-dots' style of contour lying within the true elliptical shape.

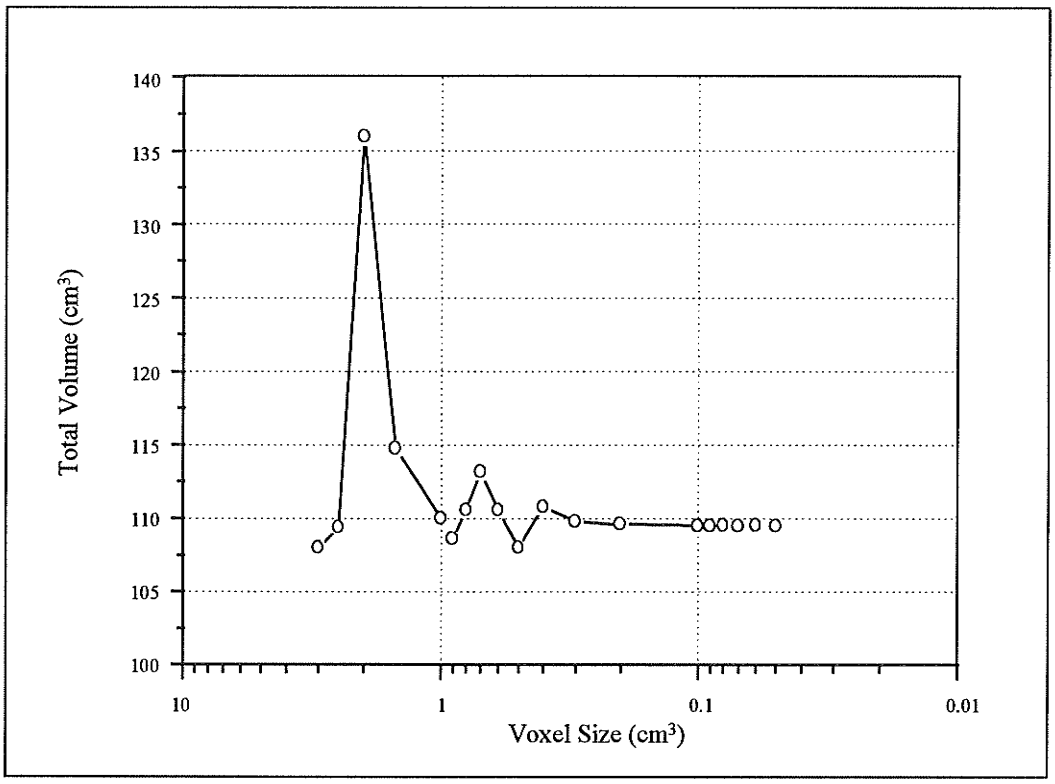

Figure 4.5: Convergence of calculated volume of computer simulation for an ideal spherical input of radius 3.0 cm. Ideal geometric volume is $4\pi(3.0)^3/3 \approx 113.1$ cm^3. Computer simulation results in a calculated volume convering to 109.5 cm^3. The slight underestimation (by 3.2%) is expected due to the linear interpolation between spherical surface points resulting in a 'connect-the-dots' style of contour lying within the true spherical shape.

4.2.3 Estimate of Magnitude

To assess the magnitude of the self-attenuation by the blood volume, computer simulation is utilized. End-diastolic and end-systolic contours with dimension and shape based on standard textbook information (Cardiac Imaging: a companion to Braunwald's Heart Disease, 1991) are used in this simulation, with the long axis of the LV defined as lying at 40° to the gamma camera face surface. Due to the larger volume of the LV at end-diastole (compared with end-systole), the end-diastolic volume should result in a greater attenuation of signal. A voxel size of 0.09 cm per side is employed to yield the following results:

	End-diastolic model	End-systolic model	Resulting EF (%)
True Volume (cm^3)	112.66	30.51	72.9
Effective Attenuated Volume (cm^3)	87.52	26.01	70.3

As predicted, the magnitude of self-attenuation demonstrated by the end-diastolic model is greater than the end-systolic model. In the end-diastole situation, 22.3% of the original signal produced in the LV has been attenuated by the LV blood volume itself, while only 14.7% attenuation occurs in the end-systole model. This results in a mild underestimation in the true EF of 2.6% for these chosen heart dimensions. This value compares well to the results ~4.5% by Yeh (1981) and 2-5% by Gandesman (1990). Note that this underestimate will increase for a dilated ventricle situation.

The magnitude of this effect is large, and warrants correction. The following section discusses a novel method for correcting a measured ejection fraction for the self-attenuation due to the LV blood volume.

4.2.4 Correction Method

Several methods have been proposed to correct for photon attenuation in radionuclide ventriculography. These involve geometric modeling (Clements, 1981; Dell'Italia, 1985), chest wall thickness estimates (Parrish, 1982), imaging of patient blood samples (Links, 1982), simultaneous imaging of an added source (Kronenberg, 1985; Nickoloff, 1983; Rabinovitch, 1984), and measuring LV length through an alternate modality such as 2D echocardiography (Thomsen, 1984).

A relatively simple method for correcting the EF for the self-attenuation of the blood volume may be implemented with a minimal amount of manual intervention and use of two look-up tables summarizing the results found by the computer simulation. The look-up tables consist of a set of multiplicative correction values for effective LV lengths versus measured angles of the gamma camera (with respect to the LV long axis). A table for each of the end-diastolic and end-systolic portions of the heart cycle may be found in Appendix B. By estimating the long axis length of the LV at both end-diastole and end-systole, and assuming similar heart shape to that used in the computer model (which was based on clinical data), multiplicative correction factors for the ED and ES

volumes may be found, and together these may be interpreted as a single multiplicative correction factor for the EF.

The long axis length estimates may be obtained from the gated sequence of images collected in the anterior view. Recall this is one of the three standard views of the heart acquired under the HSC equilibrium gated blood pool imaging protocol (refer to Figure 1.1). A simple manual measurement of the width (in x-dimension) and height (in y-dimension) of the LV long axis may be performed directly from the image. These values in pixel units may be converted to SI units with knowledge of the spatial resolution of the image which may be procured from the ratio of (width of field of view):(number of pixels across image). For the camera used to acquire all studies in this analysis, the field of view is 11.0 inches (27.9 cm) and the image width is 64×64 pixels. Hence each pixel in the image represents a 0.44×0.44 cm^2 area. The manual LV width and height estimates must be modified as below, due to the geometry of the anterior camera angle view with respect to the best septal view (see Figure 4.5 below).

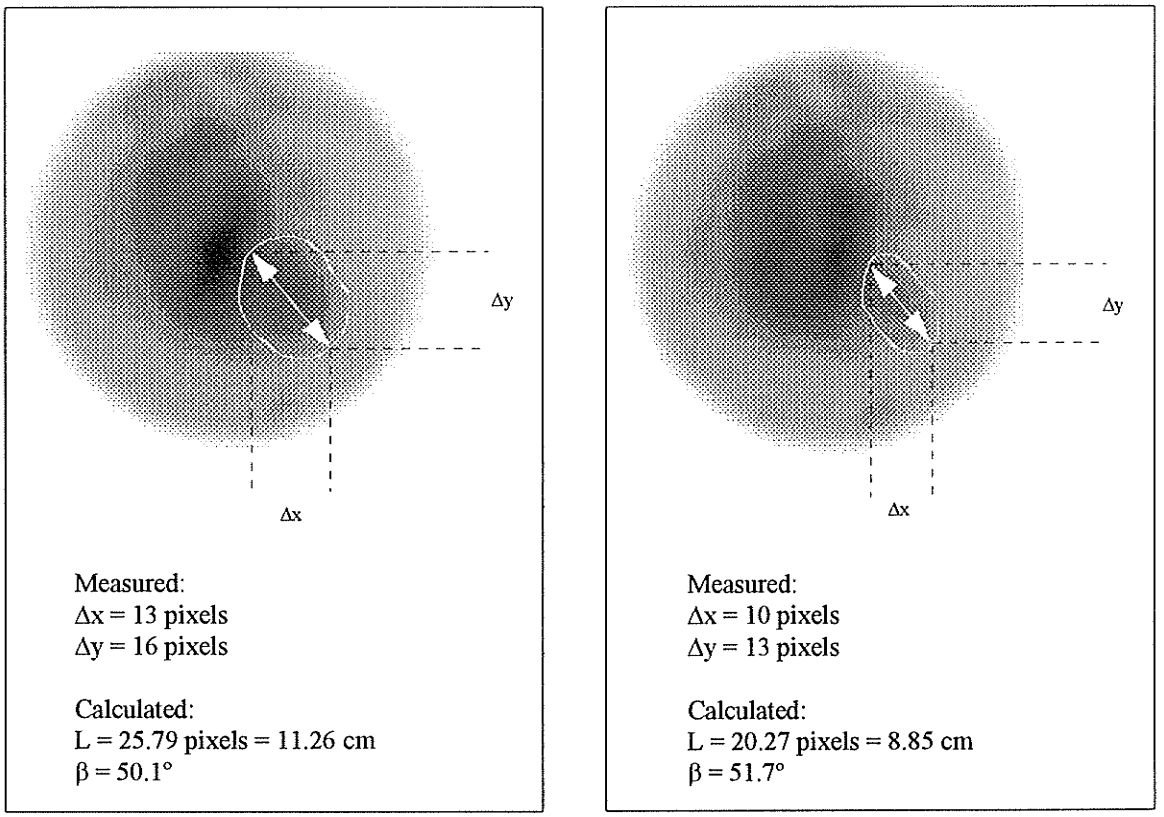

(a) (b)

Figure 4.5: Manual measurements of Δx and Δy parameters from the anterior view study, with resulting calculated values of left ventricle long axis length (*L*) and angle to the vertical (β) as found using equations 4.2 and 4.4. (a) End-diastolic image frame, and (b) end-systolic image frame.

The values of the length of the LV long axis (*L*) and the angle of this axis to the vertical (β) are solved below, using Figure 4.6 to illustrate the geometry and parameters involved. To determine the length of the LV long axis, the equation for length of a line in Cartesian coordinates may be used:

$$L = \sqrt{(\Delta x)^2 + (\Delta y)^2 + (\Delta z)^2} \tag{4.1}$$

Since the angular relationship between the anterior view and the best septal view is known to be 40°, then

$$\Delta z = \frac{\Delta x}{\tan(40^\circ)}$$

So equation (4.1) becomes:

$$L = \sqrt{(\Delta x)^2(1+\cot^2(40^\circ)) + (\Delta y)^2} \tag{4.2}$$

Now, the angle of the LV long axis to the vertical (β) may be found by rearranging

$$\tan(\beta) = \frac{\left(\frac{(\Delta x)}{\sin(40^\circ)}\right)}{(\Delta y)} \tag{4.3}$$

for β, as follows:

$$\beta = \tan^{-1}\left(\frac{\Delta x}{\Delta y \cdot \sin(40^\circ)}\right) \tag{4.4}$$

Hence, the manually measured values of Δx and Δy as described above in Figure 4.5 are utilized in equations (4.2) and (4.4) to generate the LV long axis length and angle to the vertical.

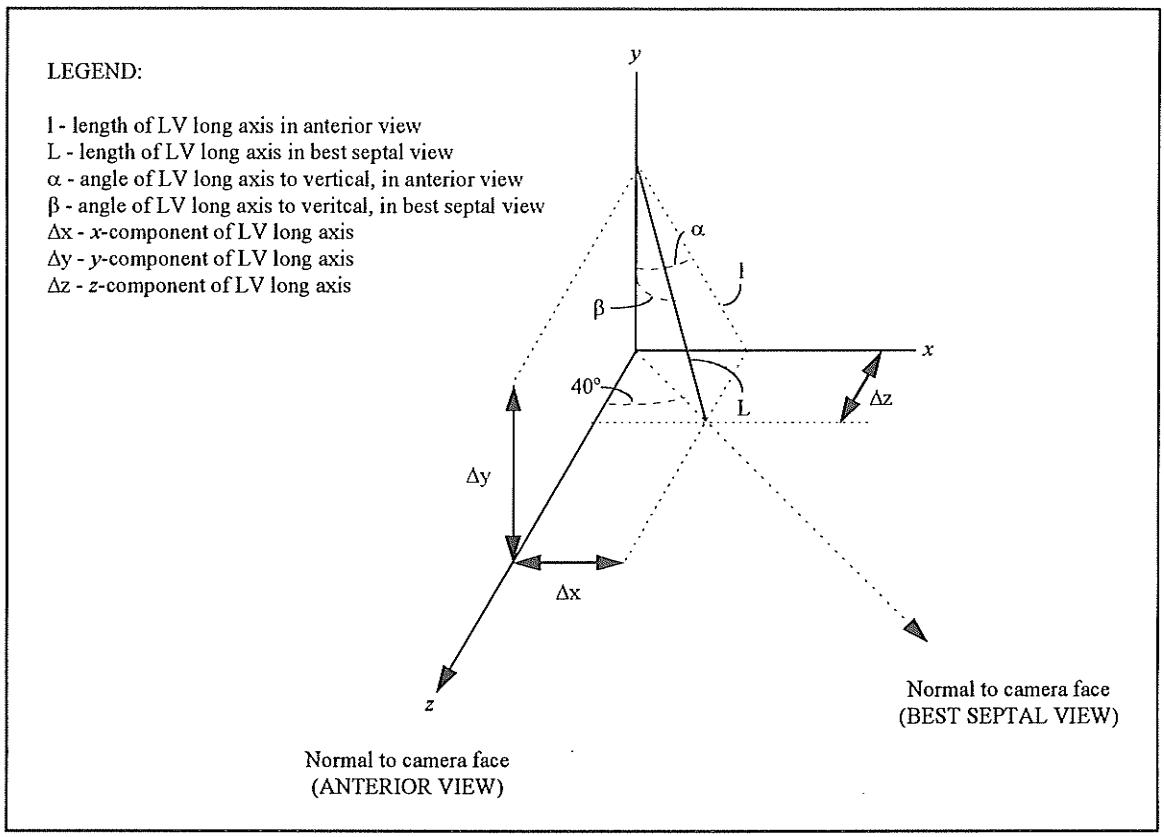

Figure 4.6: Illustration of the geometry and parameters involved when using the Δx and Δy manually determined parameters to calculate values for the long axis length and the angle of the long axis to the vertical.

The values of L and β are then used to find a multiplicative correction factor in the look-up table appropriate for heart shape (eg. end-diastolic or end-systolic table). The values of L and β as measured in the end-diastolic image frame will yield a correction factor of C_{ED}, and similarly for the end-systolic image, a correction factor C_{ES}.

The uncorrected ejection fraction is found using,

$$EF = 1 - \frac{ESC}{EDC}, \tag{4.5}$$

while the corrected ejection fraction (EF_C) is found as:

$$EF_C = 1 - \frac{ESC \times C_{ES}}{EDC \times C_{ED}} \tag{4.6}$$

Rearranging equation (4.5) and substituting into equation (4.6) yields an expression for a corrected ejection fraction in terms of known values:

$$EF_C = 1 - (1 - EF)\left(\frac{C_{ES}}{C_{ED}}\right) \tag{4.7}$$

The correction factors are the ratio of the true LV volume to the effective attenuated LV volume, as calculated by computer simulation. Direct substitution of this definition into equation 4.7 results in the correct expression for the true ejection fraction.

For the example image set given in Figure 4.5, the L and β values correspond to correction factors C_{ES} and C_{ED} of 1.2904 and 1.4913 respectively (using the appropriate look-up tables in Appendix B). Using equation 4.7 for a measured EF of 37.4% (fuzzy method), these values yield a corrected ejection fraction of 45.8%. Thus, assuming the simulated heart shape is similar to the measured heart, self-attenuation due to the blood volume in this test case results in an underestimate of EF of approximately 8.4% (in absolute EF).

This underestimate is quite large compared with the underestimate of 2.6% using textbook cardiac dimensions discussed previously. This is a consequence of the large long axis dimensions (11.26 cm for ED, 8.85 cm for ES) estimated for the example image relative to the average axis dimensions (7.0 cm for ED, 5.5 cm for ES) used in the ideal case. The difference may be attributed to the test case being a heart of significantly above average dimension. A more accurate estimate of the length dimension would be achieved by an experienced technician.

4.2.5 Effect of Error in Long Axis Length Estimate

A simple error analysis is performed in this section. The error in Δx and Δy estimates above is assumed to be equal in magnitude, δp pixels. Thus we have from equation (4.2):

$$L = \sqrt{(\Delta x \pm \delta p)^2 \cot^2(40°) + (\Delta y \pm \delta p)^2} \tag{4.8}$$

Applying simple error propagation rules to this equation, we may solve for the error in L (named δL), in terms of δp, and after some math we achieve:

$$\delta L = \frac{\delta p\left(\Delta x \cot^2(40°) + \Delta y\right)}{\sqrt{(\Delta x)^2 \cot^2(40°) + (\Delta y)^2}} = \frac{\delta p\left(\Delta x \cot^2(40°) + \Delta y\right.}{L} \tag{4.9}$$

The ideal estimate of δp is ±0.5 pixels, for the case when the shape of the LV is well defined (that is, half of the smallest division). Unfortunately a clear boundary is not available, hence the error estimate δp must also incorporate the uncertainty in LV boundary location (again assuming that this error will be the same in the x and y directions). Taking a rough estimate of δp including this LV boundary uncertainty to be ±2.5 pixels, and using the values of Δx, Δy, and L from Figure 4.6 (a), we may make an estimate of δL using equation (4.9):

$$\delta L = \frac{(2.5)\left(13\cot^2(40°)+16\right)}{25.79} = 3.34 \text{ pixels} = 1.46 \text{ cm}$$

Thus, using the measurements from Figure 4.6 (a), and assuming an error in Δx and Δy of ± 2.5 pixels, an uncertainty of ± 1.5 cm in length (or 13%) results. The range of L for this case becomes 9.8 cm - 12.7 cm. Consulting the ED correction look-up table in Appendix B, we see that the range of C_{ED} values is 1.42 - 1.54 (or approximately 1.49 ± 0.06). Similar analysis of data in Figure 4.6 (b) yields an estimated range of C_{ES} values of 1.24 - 1.34 (or approximately 1.29 ± 0.05). Combining the two estimates of error and applying simple error analysis techniques to equation (4.7) yields:

$$\delta EF_c = \left[\frac{\delta C_{ES}}{C_{ES}} + \frac{\delta C_{ED}}{C_{ED}}\right] \cdot \frac{C_{ES}}{C_{ED}} \cdot (1 - EF) \tag{4.10}$$

By using $\delta C_{ES} = 0.05$ and $\delta C_{ED} = 0.06$, the uncertainty in the corrected EF due to uncertainty in the lengths of the two long axis estimates alone is 4.3% (absolute EF units). From this example it is concluded that the estimate of long axis length is critical to the overall accuracy of this attenuation correction method.

References

Cardiac Imaging: a companion to Braunwald's Heart Disease. Ed. Marcus, M. C., H. R. Schelbert, D. J. Skorton, et al. Philadelphia: W.B. Saunders Company, 1991. 1-1318.

Bezdek, J. C., R. Ehrlich, and W. Full. "FCM: The Fuzzy c-Means Clustering Algorithm." Computers and Geosciences 10 (2-3) (1984): 191-203.

Clements, I.P., M.L. Brown, and H.C. Smith. "Radionuclide Measurement of Left Ventricular Volume." Mayo Clinic Procedures 56 (1981): 733-739.

Dell'Italia, L.J., M.R. Starling, R.A. Walsh, et al. "Validation of attenuation-corrected equilibrium radionuclide angiographic determinations of right ventricular volume: comparison with cast-validated biplane cineventriculography." Circulation 72 (2) (1985): 317-326.

Gandsman, E.J., D.L. North, and E.W. Bough. "The nature of the background in radionuclide ventriculography: deductions from the mathematical behavior of the ejection fraction." Physics in Medicine and Biology 35 (11) (1990): 1467-1476.

Green, M. V., S. L. Bacharach, M. A. Douglas, et al. "Sources of Virtual Background in Multi-Image Blood Pool Studies." Nuclear Cardiology: Selected Computer Aspects. Ed. Anonymous. New York, NY: The Society of Nuclear Medicine, Inc., 1978. 97-106.

Kronenberg, M.W., M.D. Parrish, D.W. Jenkins,Jr., et al. "Accuracy of Radionuclide Ventriculography for Estimation of Left Ventricular Volume Changes and End-Systolic Pressure-Volume Relations." Journal of American College of Cardiology 6 (5) (1985): 1064-1072.

Links, J.M., L.C. Becker, J.G. Shindledecker, et al. "Measurement of Absolute Left Ventricular Volume From Gated Blood Pool Studies." Circulation 65 (1) (1982): 82-91.

Nickoloff, E.L., P.D. Esser, W.H. Perman, et al. "Physical Basis for Linear Attenuation Corrections in Radionuclide Determination of Left Ventricular Volume (LVV)." Medical Physics 10 (4) (1983): 523(Abstract)

Parrish, M.D., T.P. Graham,Jr., M.L. Born, et al. "Radionuclide Ventriculography for Assessment of Absolute Right and Left Ventricular Volumes in Children." Circulation 66 (4) (1982): 811-819.

Rabinovitch, M.A., V. Kalff, K. Koral, et al. "Count-based left venticular volume determination utilizing a left posterior oblique view for attenuation correction." Radiology 150 (1984): 813-818.

Thomsen, J.H. "Estimation of Absolute Ventricular Volume (To the Editor:)." Chest 85 (5) (1984): 711-712.

Thomsen, J.H., A.K. Patel, B.R. Rowe, et al. "Estimation of Absolute Left Ventricular Volume from Gated radionuclide Ventriculograms: A Method Using Phase Image Assisted Automated Edge Detection and Two-dimensional Echocardiography." Chest 84 (1) (1983): 6-13.

Chapter Five: RESULTS

5.0 Introduction

When developing any new technique, the results must be objectively evaluated. This may be achieved in part through quantitative comparison with a previous technique in which confidence is placed, the so called 'gold standard'. In this chapter, the fuzzy clustering method of identifying the left ventricle and calculating ejection fraction is compared to the manual technique used at the HSC.

In addition, the error in the fuzzy method due to the choice of a single set of operating parameters over individually optimised parameter sets is estimated.

5.1 Comparison to Standard Technique

5.1.1 Fuzzy Versus Manual Method

The automated method of left ventricular detection and ejection fraction calculation as described in Chapter Three of this thesis has been applied to a test set of 10 images. The test images were chosen at random from the patient data base at HSC. The only characteristic necessary for inclusion in the test group was that the phase image of the heart be normal. That is, it was required that the phase images of the test group data sets exhibit no regions of noticeable dyskinetic motion. With the first clustering

application using the phase image (first harmonic phase, x- and y-coordinates) and the isolation image (a derivative of the phase image) as input, it is obvious that the results will be significantly dependent upon the phase image. Since the aim of this thesis is to develop an automated left ventricle detection method for normal hearts, the requirement that the phase images be normal is a rational limitation when selecting test images. It is anticipated that the algorithm as developed in this work would not function properly on studies demonstrating abnormal phase images. However, the possibility does exist for modification of this technique to analyse studies exhibiting abnormal phase images.

The group of ten test images were selected at random from the patient database at HSC. All the studies within this group were performed between January 2 and January 9 of 1995. The phase image for each study was generated. If the phase image displayed any significant deviations from the norm (compared to standard literature examples), it was not included in the test group.

The group of test images has been analysed with the manual and semi-automatic methods, as described in sections 1.2.3 and 1.2.4 respectively. The fully automated fuzzy technique was applied to each image set, after an optimum set of operating parameters had been derived (as discussed in section 4.1). The results of all three techniques on the test group are presented in Table 5.1.

Study Number	Ejection Fraction (%)		
	Manual	Semi-automatic	Fuzzy automated
1	47.2	41.4	37.8
2	54.6	59.4	49.3
3	52.6	50.0	41.0
4	35.9	30.9	23.7
5	62.7	59.0	52.0
6	38.3	41.7	32.4
7	41.4	36.4	32.0
8	57.3	58.7	54.2
9	53.4	55.9	50.6
10	64.8	60.8	47.2

Table 5.1: Results of three ejection fraction analysis techniques on a sample set of 10 test studies. Ejection fractions are given in percentages.

The manual technique is used as the 'gold standard' for comparison of the fuzzy automated method. The correlation coefficient for the manual and fuzzy results is found to be 0.90, and the fuzzy technique underestimates the EF on all test images, by 7.75 % (in units of absolute EF) on average as illustrated in Figure 5.1. The slope of the best fit line is 0.97, close to a value of 1.0 which would be expected for a perfect correlation between the two methods, and indicates an excellent correlation between the two methods. The significant underestimation is due to the fuzzy method identifying tighter boundaries around the LV, as compared to the manual technique, and is further described in section 5.1.2.

The reasoning behind the liberal definition of LV contours in the manual method is explained with the help of Figure 2.1 (c) [page 54]: since an exact estimate of EF will

generally be impossible, less error will be introduced by making an overestimation of the LV contour rather than an underestimation. However, it should be noted that this reasoning loses validity at higher true ejection fractions. This approach of identifying 'looser' LV boundaries is taken due to the lack of a more reliable method.

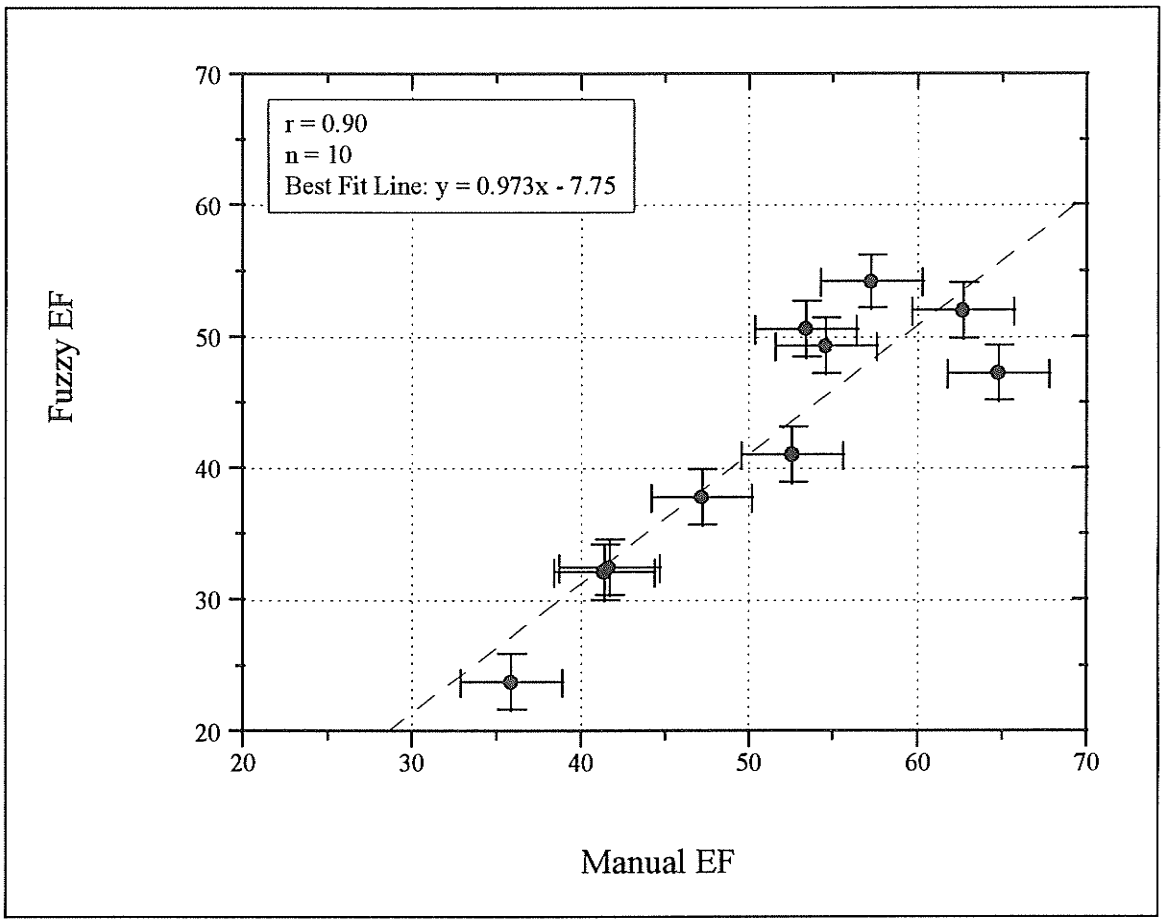

Figure 5.1: Comparison of manual and fuzzy techniques for calculating ejection fractions for a test group of ten images.

Error bars placed on the data points in Figure 5.1 have a magnitude of ±3% for the manual technique and ±1.8% for the fuzzy method. The exact nature of the information contained in these error bars is discussed in the remainder of this section.

The uncertainty due to intra- and inter-observer variation using the manual method has been previously reported by Kaul (1983) and Okada (1980) to range between ±3% and ±6% under normal clinical conditions. The most optimistic estimate resulting from these studies is taken as ±3%. Uncertainty due to choice of an optimal set of operating parameters for the whole test group (as opposed to individually optimised parameter sets) using the fuzzy technique is estimated at ±1.8% as calculated in section 5.3.

These estimates ignore other possible sources of uncertainty (as discussed in chapter 4) which may effect the EF evaluation. However, since all other sources will influence results from both techniques in a similar manner, the only difference in the uncertainty between the two methods are those uncertainties discussed above. The fuzzy technique, being fully automated, will not suffer any intra- or inter-observer variation while the manual technique does not require any optimisation of parameters used. Hence, the fuzzy method as developed here seems to reduce the overall statistical uncertainty in the EF estimation, as compared to the most conservative estimate of error in the manual technique.

All computer code for the fuzzy clustering technique is written in HP FORTRAN-9000. Execution time takes approximately 150 seconds (it should be noted, however, that this has not been streamlined for computational speed) on a HP 715/75 workstation.

5.1.2 Underestimation of Ejection Fraction

The average underestimation by 7.75% of the fuzzy clustering EF results as compared to the manual analysis is directly attributable to the relatively tight LV boundaries identified by the fuzzy approach. By defining a wider or 'looser' boundary around the LV especially in the ED frame, the manual method therefore results in a larger number of counts being attributed to the ED frame as compared to the fuzzy clustering method. This difference causes the EF calculated via the manual technique to be higher than when computed with the fuzzy technique. To verify that this reasoning is correct, the effects of loosening the identified (via the fuzzy method) LV boundary on a single test study was analysed.

The LV boundary in the end-diastole frame was grown outwards by repeated addition of a single layer of pixels along the 0° to 200° region of the boundary (illustrated in Figure 5.2), so as to approach the manually defined boundary. The EF was recalculated for each new end-diastole LV ROI, holding the end-systole LV ROI and background estimate constant, and employing equation 1.2. The LV boundary of the end-systole frame was then expanded by a single pixel in a similar manner, and the EF recalculated for each of the increased end-diastole boundaries. The results are summarized in Tables 5.2 and 5.3. Ideally, it was expected that the EF would converge as the boundary of the LV approaches the background activity level. While it was expected that the end results will yield similar EF's, since the manual contours were used as guides, the verification should be strengthened by examining the convergence to the

manual EF. This tendency is observed to some extent, but the convergence is not as rapid as expected due to the area of higher than background activity in the 0° to 60° region of the LV boundary. This area is demonstrating activity which may originate from the left atria, and hence will not fall away to background activity levels.

The data in Table 5.3 demonstrate that when holding the end-systolic LV ROI constant, growth of the end-diastolic LV ROI leads to values in excess of the manual EF estimate of 47.2%. If the end-systolic LV ROI is grown by one layer, then the growth of the end-diastolic LV ROI more closely approaches the manual EF estimate. When the end-systolic LV ROI is grown by two pixel layers, growth of the end-diastolic LV ROI converges to a value much less than the manual EF estimate. This analysis indicates that the underestimation of the EF estimate by the fuzzy technique results from the tightness of LV ROI in the end-diastolic frame, as compared to that identified using the manual method.

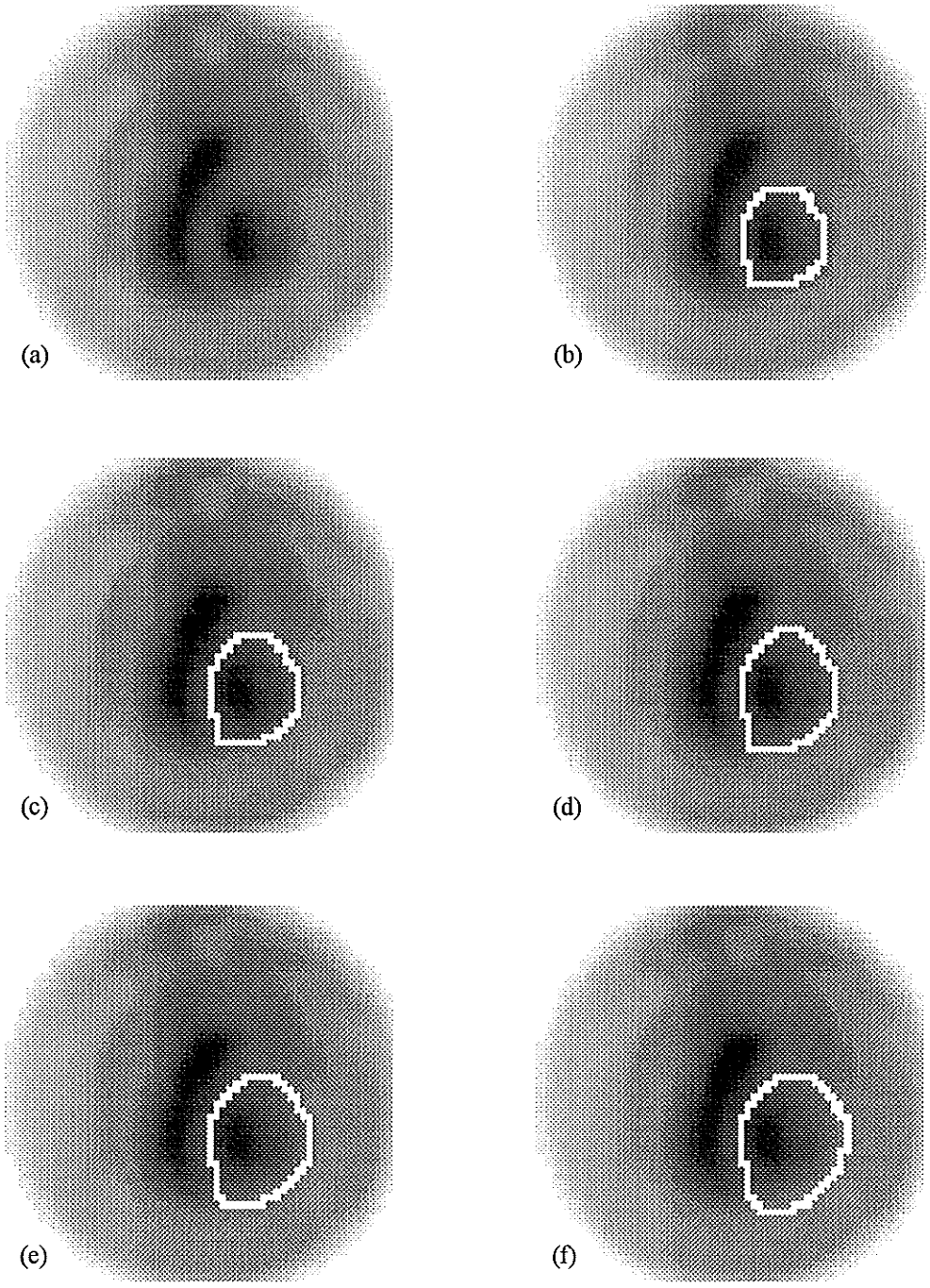

Figure 5.2: **The evolution of the LV ROI in the end-diastolic frame, for the purposes of identifying the origin of the 7.75% on average underestimation of EF by the fuzzy method as compared to the manual method. (a) The original end-diastolic image frame, (b) the original fuzzy identified LV ROI, (c) +1 layer of pixels added to the LV ROI, (d) +2 layer of pixels added to the LV ROI, (e) +3 layer of pixels added to the LV ROI, and (f) +4 layer of pixels added to the LV ROI.**

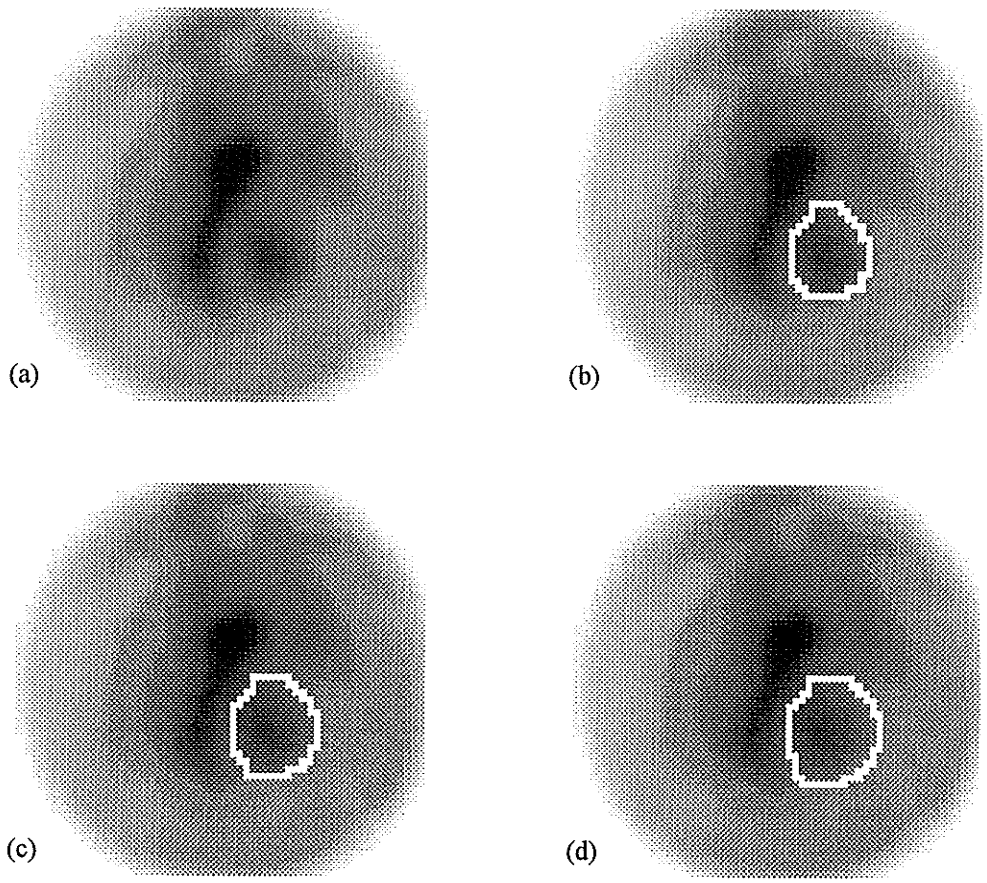

Figure 5.3: **The evolution of the LV ROI in the end-systolic frame, for the purposes of identifying the origin of the 7.75% on average underestimation of EF by the fuzzy method as compared to the manual method. (a) The original end-systolic image frame, (b) the original fuzzy identified LV ROI, (c) +1 layer of pixels added to the LV ROI, (d) +2 layer of pixels added to the LV ROI.**

Boundary Grown	Number of Pixels Added to LV ROI	Average Intensity of Added Pixels	Average Added Pixel Intensity Corrected for Background	Increase in LV ROI Counts
+1 on ED	24	160.83	70.90	1701.6
+2 on ED	25	144.32	54.39	1359.7
+3 on ED	24	122.61	32.68	751.5
+4 on ED	21	115.71	25.78	541.4
+1 on ES	18	144.61	54.68	984.2
+2 on ES	21	123.38	33.45	702.4

Table 5.2: Raw data obtained from adding on layers of single pixels to the LV ROI boundaries in the region of 0° to 200°, on both end-diastolic (ED) and end-systolic (ES) frames.

Description of Added LV ROI Boundaries	Resultant Ejection Fraction
original ES, original ED	35.3
original ES, +1 ED	42.7
original ES, +2 ED	47.5
original ES, +3 ED	49.9
original ES, +4 ED	51.4
+1 ES, +1 ED	36.1
+1 ES, +2 ED	41.5
+1 ES, +3 ED	44.2
+1 ES, +4 ED	45.8
+2 ES, +2 ED	37.1
+2 ES, +3 ED	40.1
+2 ES, +4 ED	41.8

Table 5.3: Resulting ejection fractions calculated using various combinations of modified LV ROI's in both end-diastolic and end-systolic frames.

5.2 Comparison of Manual and Automated Background Selection

In this section, the background activity estimates made by the automated routine (as described in section 3.5) are compared to those made during the manual analysis. Unfortunately, the background activity estimated during the manual analysis is not saved to disk, nor printed out on hardcopy. The only available relevant information is the shape of the background ROI overlain on the end-systolic image frame, along with the end-systolic LV ROI. This information was utilized by overlaying the background ROI shape on the original image data. This was accomplished by digitizing the film image on a Vision Ten Inc. film scanner and scaling the image size to match the original frame, overlaying the background ROI shape on the original frame, then manually reading out the background pixel grayscale information. This method was the best available to recover the manual background activity estimates.

The automated background activity estimate compared well with the manual background estimate, as summarized in Table 5.4. As expected, the automated method returns lower background estimates than the manual, on average. However, this underestimation is only ~1.7 in units of number of grayscales of activity. It is important to be able to assess the effect of this underestimation on the resultant EF. The magnitude of effect is dependent upon the counts in the LV ROI in both ED and ES, as observed in equation 1.2. Taking a hypothetical example, if one assumes EDC = 20000, ESC = 12000, n_{ED} = 120, n_{ES} = 80, and a BG of 100, then equation 1.2 yields an EF of 50.0%. An underestimation in BG by 5%, taking BG to a value of 95, will result in an EF of

48.8%. Hence, for this hypothetical situation, an underestimation of BG by 5% results in an underestimation of EF by 1.2%. Interestingly, an overestimation of BG by 5% results in an overestimation of EF by 1.4% (similar to the observed effect in Figure 3.16). Only two automated background estimates are outside of a ±5% range from the manual method. Image set four was the most severely underestimated at -11.3%. Image set seven demonstrated an overestimate by the automated routine, this being attributable to the relatively small size of BG ROI delineated by the manual method.

Image Set Number	Number of Sampled Pixels	Manual BG Estimate (grayscales)	Automated BG Estimate (grayscales)	Percentage Difference (%)
1	16	91.8	89.8	-2.0
2	16	105.7	102.2	-3.3
3	12	95.5	99.2	+3.9
4	20	110.6	98.1	-11.3
5	18	81.8	85.3	+4.9
6	16	88.8	87.6	-1.4
7	6	129.2	138.3	+7.1
8	18	113.3	108.6	-4.2
9	18	52.1	50.9	-2.3
10	18	100.8	99.7	-1.1

Table 5.4: Comparison of manual and automated background activity estimates for ten image sets.

A graphical comparison of the manual and automated background estimate methods also verifies an excellent relationship.. Figure 5.4 demonstrates this, with a linear best fit line possessing equation $y = 1.01x - 1.65$, and a correlation coefficient of $r = 0.93$. The slope value is very close to the ideal identity of 1.0, while the intercept

indicates an underestimation of 1.65 grayscales, on average, is to be expected. This value may be slightly high due to the unusual circumstances of the +7.1% overestimate in image set seven as discussed above.

Therefore, the underestimation of background activity will result in only a minor underestimation of EF, on the order of ≤1%. The more significant underestimation observed in image set four will result in a larger effect, compounded by the lower EF magnitude. For this particular image set, the underestimation of background will be more significantly responsible for the underestimation of fuzzy EF (23.7%) vs manual EF (35.9%), than in other image sets.

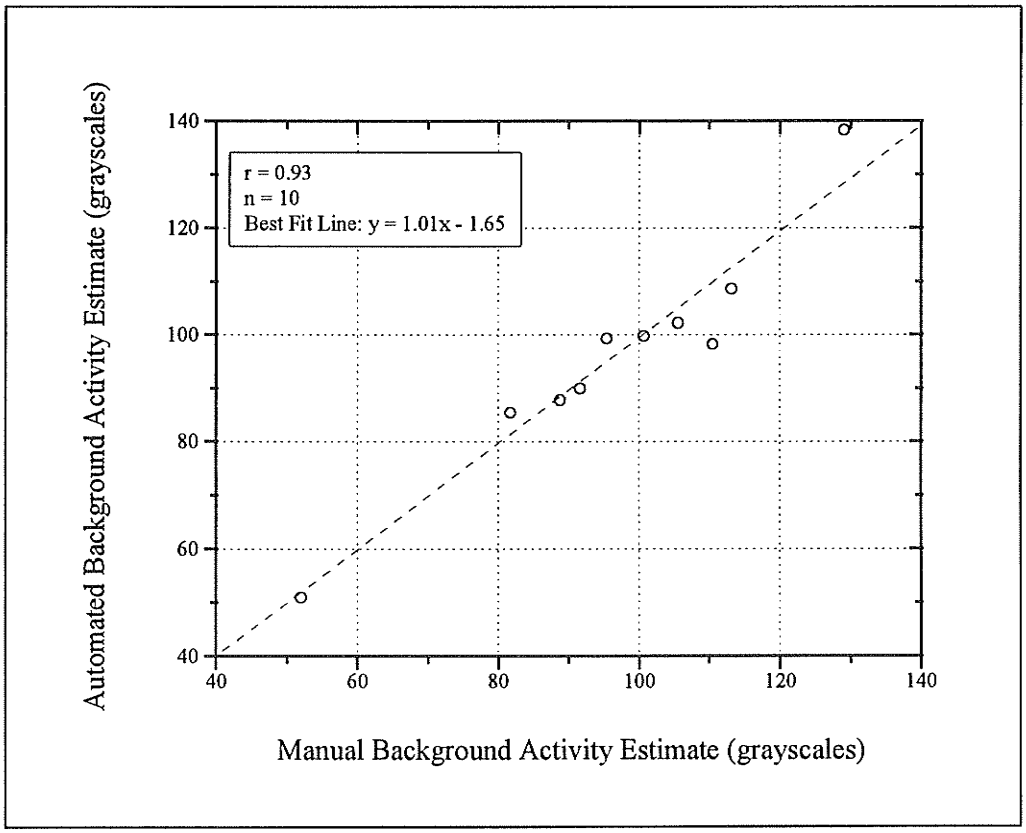

Figure 5.4: Automated versus manual background activity estimates, in units of grayscales, for ten image sets.

5.3 Estimated Uncertainty Due to Parameterization

The uncertainty due to selection of a global set of optimal parameters to use for all image sets is estimated. From previous analysis (see section 4.1), the stable operating range of required input parameters has been established for each individual image set in the test group. The scope of EF output for these stable operating ranges is found by calculating the EF via the fuzzy clustering method for every discrete value within the stable operating range, of all the optimised parameters. The maximum and minimum values of the resulting list of ejection fractions define the size of the uncertainty range (via subtraction of the minimum value from the maximum value) for that particular image set. This processing has been performed on all image sets. Table 5.5 below contains all the relevant data for this analysis.

Image Set Number	Output ejection fraction range using stable parameters (%)	Uncertainty in ejection fraction (%)
1	29.4 - 32.7	3.3
2	46.1 - 52.1	6.0
3	27.5 - 32.0	4.5
4	17.9 - 18.5	0.6
5	39.0 - 43.4	4.4
6	24.0 - 26.5	2.5
7	22.7 - 27.9	5.2
8	51.5 - 54.2	2.7
9	35.6 - 39.6	4.0
10	35.8 - 37.8	3.0

Table 5.5: Range of ejection fraction values as evaluated over stable range of operating parameters for each image set tested.

The values in column three of Table 5.5 above are averaged to yield a single uncertainty estimate of ±1.8%. This value represents the average uncertainty in the fuzzy technique ejection fraction calculation due to selection of a single set of parameters over individually optimised sets.

References

Kaul, S., C.A. Boucher, R.D. Okada, et al. "Sources of Variability in the Radionuclide Angiographic Assessment of Ejection Fraction: A Comparison of First-Pass and Gated Equilibrium Techniques." American Journal of Cardiology 53 (1983): 823-828.

Okada, R.D., H.D. Kirshenbaum, F.G. Kushner, et al. "Observer Variance in the Qualitative Evaluation of Left Ventricular Wall Motion and the Quantitation of Left Ventricular Ejection Fraction Using Rest and Exercise Multigated Blood Pool Imaging." Circulation 61 (1) (1980): 128-136.

Chapter Six: SUMMARY

The primary objective of this thesis was to develop a fully automated computer algorithm which would calculate ejection fraction from gated blood pool images of the heart of a normal patient. A secondary goal of this thesis was to compile a comprehensive index of sources of error or uncertainty which may affect the calculation of ejection fraction using gated blood pool imaging. Furthermore, the error in ejection fraction due to photon attenuation was explored in greater detail, and a novel and simple correction method proposed.

An automated left ventricle detection routine was developed. The use of edge detection methods, currently the most popular automated approach to left ventricle detection, was avoided in favor of a more adaptable type of algorithm. A method for detecting the left ventricle based primarily on application of the fuzzy *c*-means clustering algorithm was devised.

The technique developed in this thesis begins with a fuzzy clustering application to phase information calculated from an entire LAO view image set. A subroutine which identifies the septum based on simple edge detection techniques is applied. The second application of the fuzzy clustering algorithm on each processed image frame results in delineation of the left ventricle in each image frame. By summing the counts in each frame, a time activity curve (uncorrected for background counts) is produced for the image set. An automated background estimation routine provides an estimate of background activity which is applied to the uncorrected time activity curve in a spatially

uniform, time dependent manner. This corrected time activity curve is fitted using a Fourier series expansion up to the second harmonic. The estimated ejection fraction is calculated from this background corrected and Fourier fitted time activity curve.

The success of the fuzzy algorithm as developed in this work is primarily dependant on the quality of the phase image. Regions of dyskinetic wall motion must be absent from the phase image of the data sets to be analysed by the fuzzy technique. An exciting possibility exists to modify this algorithm into one which will also be able to analyse hearts which exhibit poor phase images.

Several parameters necessary to the functioning of the algorithm were optimised to find a set of stable operating values which could be applied to the entire set of images, and any new image set requiring analysis. The uncertainty in the ejection fraction as a result of the selection of these parameters was evaluated as ±1.8%.

Comparison of the fuzzy method to the manual method demonstrates a good correlation ($r = 0.90$), but an underestimation of 7.8% on average. This underestimation is primarily a consequence of the manual method defining relatively loose contours, especially in the end-diastolic image frame, thus emphasizing the difference between end-diastolic and end-systolic counts and increasing the resulting ejection fraction value.

The effects of photon attenuation in the blood volume were discussed. A computer simulation gauging the magnitude of these effects was developed. Also, a novel manual technique was advanced for correcting the ejection fraction estimate for attenuation effects by using image data from the anterior view study combined with a look-up table summarizing the computer simulation results.

An extensive inventory comprising sources of potential error or uncertainty was compiled and discussed. Error/uncertainty was classified into three main categories: physiological sources, acquisition procedure sources, and analysis sources. The effect of errors in the end-diastolic and end-systolic counts on ejection fraction were described.

The results of this work indicate that an automated method of calculating ejection fraction based on fuzzy clustering shows great promise for use in the clinical evaluation of normal patients. Furthermore, a simple method of correcting for photon attenuation in the blood volume may be used to correct any ejection fraction estimate.

Glossary of Acronyms

BG - background

ED - end-diastolic

EDC - end-diastolic counts

EF - ejection fraction

ES - end-systolic

ESC - end-systolic counts

HSC - Health Sciences Centre, Winnipeg, Canada

LV - left ventricle

R-wave - strong cardiac electrical pulse signaling the onset of left ventricle contraction

ROI - region of interest

RV - right ventricle

TAC - time-activity curve

Appendix A: OPTIMISATION HISTOGRAMS

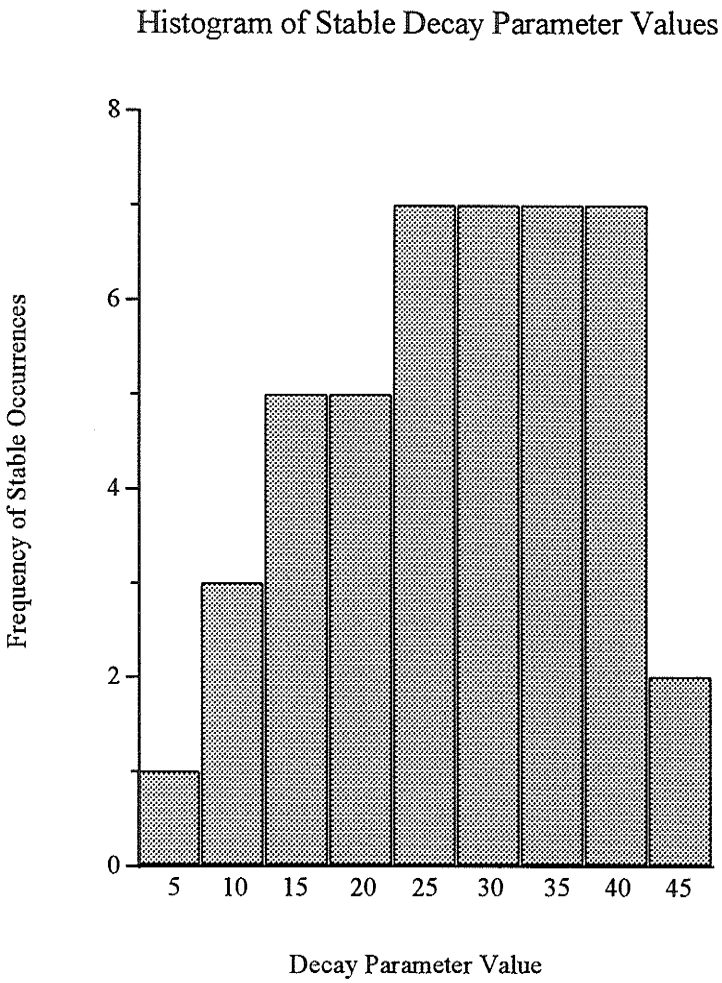
Histogram of Stable Decay Parameter Values
Frequency of Stable Occurrences
0
2
4
6
8
5
10
15
20
25
30
35
40
45
Decay Parameter Value

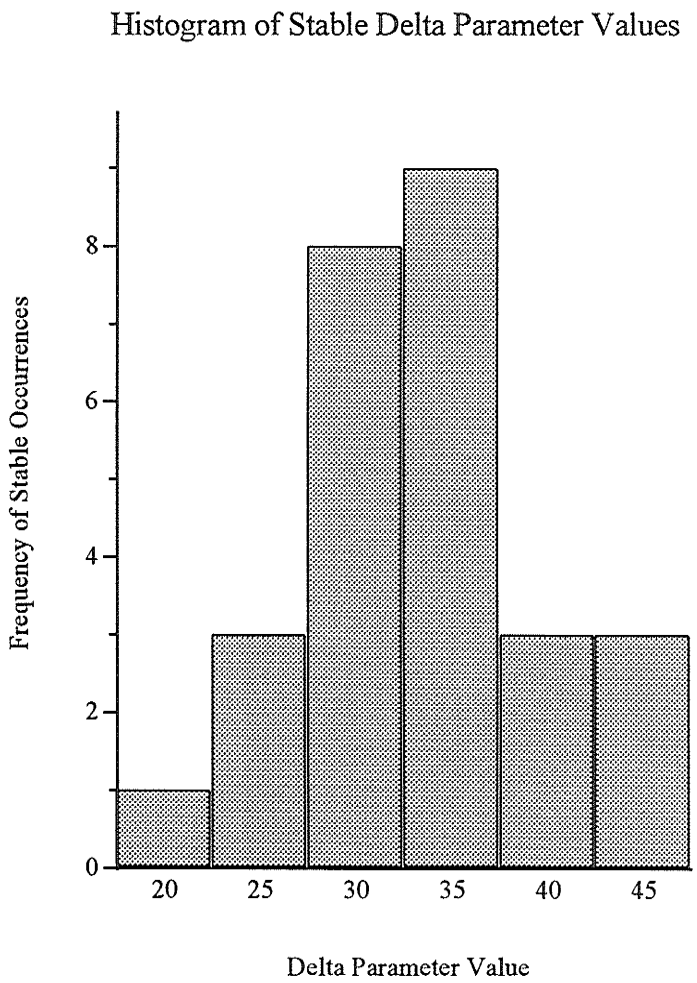
Histogram of Stable Delta Parameter Values
Frequency of Stable Occurrences
0
2
4
6
8
20
25
30
35
40
45
Delta Parameter Value

Histogram of Stable Fuzzy Weighting Exponents Used in First Clustering (m_1)

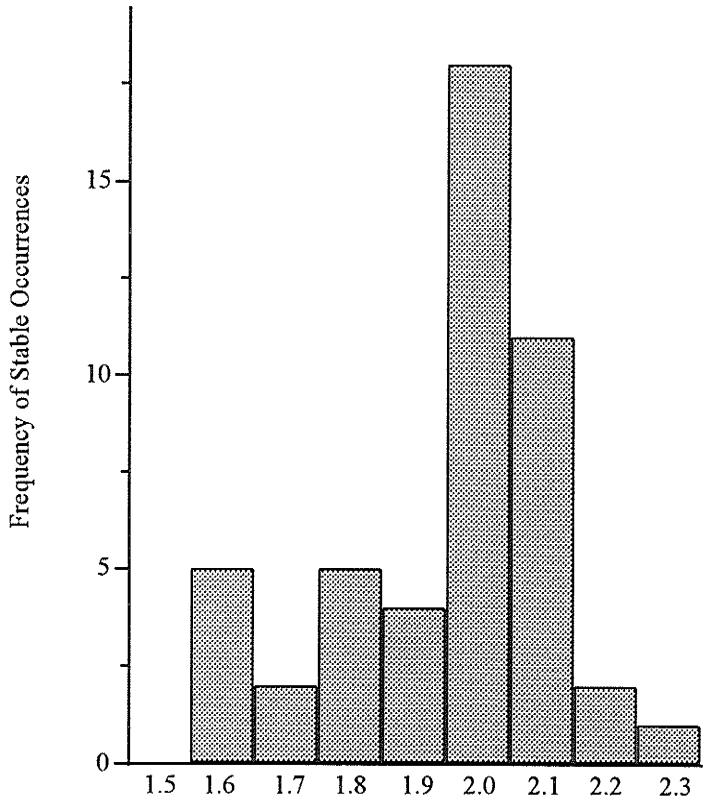

Histogram of Stable Phase and Isolation Weighting Factors (w_1)

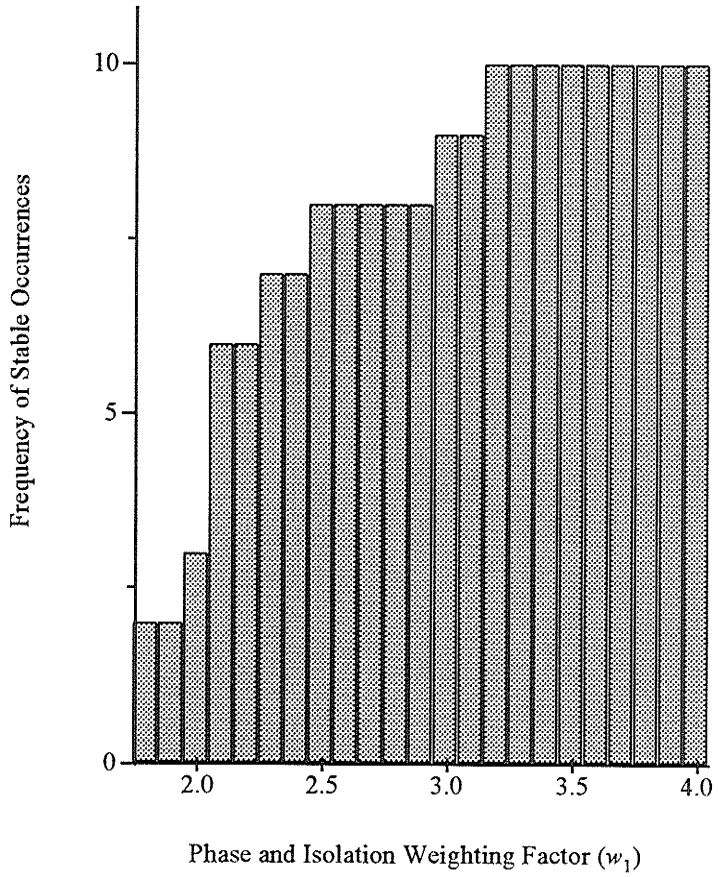

Histogram of Stable Fuzzy Weighting Exponents Used in Second Clustering (m_2)

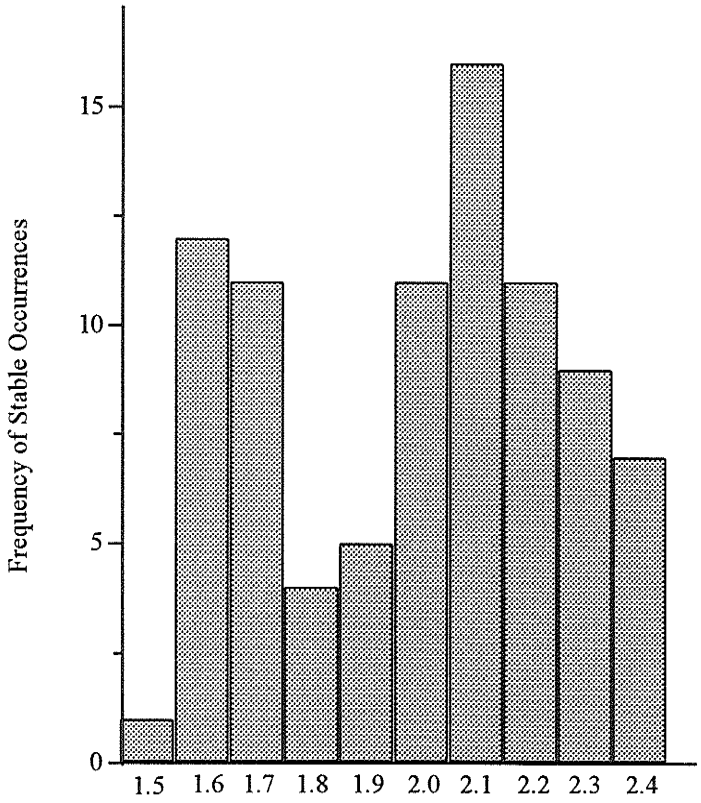

Histogram of Stable Grayscale Weighting Factors (w_2)

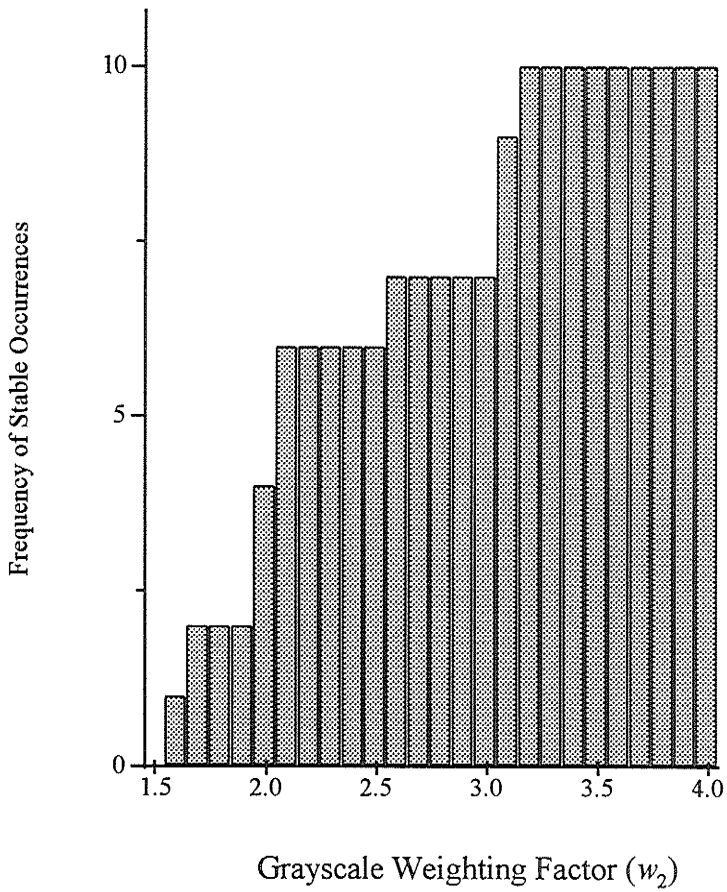

Appendix B: CORRECTION FACTOR LOOK-UP TABLES

Look-up Table for End-Diastolic Correction Value (C_{ED})

β Value - Angle of Cardiac Long Axis to Vertical (degrees)

L Value - Length of Left Ventricle (cm)

	20	25	30	35	40	45	50	55	60	65	70	75	80
4.0	1.1855	1.1767	1.1707	1.1665	1.1635	1.1613	1.1597	1.1586	1.1581	1.1579	1.1581	1.1585	1.1590
4.5	1.2096	1.1996	1.1928	1.1880	1.1847	1.1821	1.1803	1.1791	1.1784	1.1783	1.1785	1.1791	1.1797
5.0	1.2343	1.2230	1.2153	1.2099	1.2061	1.2033	1.2012	1.1998	1.1991	1.1989	1.1992	1.1998	1.2004
5.5	1.2594	1.2469	1.2382	1.2323	1.2280	1.2248	1.2225	1.2210	1.2203	1.2201	1.2204	1.2210	1.2217
6.0	1.2848	1.2710	1.2614	1.2548	1.2501	1.2466	1.2440	1.2424	1.2415	1.2413	1.2416	1.2423	1.2430
6.5	1.3102	1.2951	1.2846	1.2774	1.2722	1.2684	1.2656	1.2638	1.2628	1.2626	1.2630	1.2637	1.2645
7.0	1.3358	1.3194	1.3080	1.3002	1.2945	1.2903	1.2872	1.2853	1.2843	1.2842	1.2846	1.2853	1.2862
7.5	1.3617	1.3440	1.3317	1.3231	1.3170	1.3125	1.3092	1.3071	1.3060	1.3058	1.3063	1.3071	1.3081
8.0	1.3880	1.3689	1.3556	1.3463	1.3397	1.3349	1.3314	1.3291	1.3279	1.3277	1.3282	1.3291	1.3301
8.5	1.4146	1.3941	1.3798	1.3698	1.3628	1.3575	1.3537	1.3513	1.3501	1.3498	1.3503	1.3513	1.3524
9.0	1.4413	1.4194	1.4042	1.3935	1.3859	1.3803	1.3763	1.3737	1.3724	1.3721	1.3727	1.3737	1.3749
9.5	1.4684	1.4451	1.4288	1.4174	1.4092	1.4032	1.3989	1.3962	1.3948	1.3946	1.3952	1.3963	1.3975
10.0	1.4955	1.4708	1.4535	1.4413	1.4326	1.4263	1.4217	1.4188	1.4173	1.4171	1.4177	1.4189	1.4202
10.5	1.5231	1.4969	1.4785	1.4656	1.4564	1.4496	1.4448	1.4417	1.4402	1.4399	1.4406	1.4418	1.4432
11.0	1.5507	1.5231	1.5036	1.4899	1.4802	1.4731	1.4680	1.4647	1.4631	1.4629	1.4636	1.4649	1.4663
11.5	1.5787	1.5495	1.5290	1.5145	1.5042	1.4967	1.4913	1.4879	1.4862	1.4859	1.4867	1.4880	1.4895
12.0	1.6069	1.5762	1.5546	1.5393	1.5285	1.5205	1.5149	1.5113	1.5095	1.5093	1.5101	1.5115	1.5131
12.5	1.6352	1.6030	1.5803	1.5642	1.5528	1.5445	1.5386	1.5348	1.5330	1.5327	1.5336	1.5351	1.5367
13.0	1.6640	1.6302	1.6064	1.5895	1.5775	1.5687	1.5625	1.5586	1.5567	1.5564	1.5573	1.5589	1.5606
13.5	1.6926	1.6574	1.6324	1.6147	1.6021	1.5929	1.5864	1.5823	1.5804	1.5801	1.5810	1.5827	1.5844
14.0	1.7218	1.6849	1.6587	1.6402	1.6270	1.6174	1.6106	1.6063	1.6043	1.6040	1.6050	1.6067	1.6085
14.5	1.7510	1.7126	1.6853	1.6658	1.6521	1.6420	1.6349	1.6305	1.6283	1.6281	1.6291	1.6309	1.6328
15.0	1.7806	1.7405	1.7120	1.6917	1.6773	1.6668	1.6594	1.6548	1.6526	1.6524	1.6535	1.6553	1.6573

Look-up Table for End-Systolic Correction Value (C_{ES})

β Value - Angle of Cardiac Long Axis to Vertical (degrees)

L Value - Length of Left Ventricle (cm)

	20	25	30	35	40	45	50	55	60	65	70	75	80
2.0	1.0810	1.0762	1.0723	1.0688	1.0657	1.0632	1.0612	1.0596	1.0585	1.0578	1.0574	1.0574	1.0577
2.5	1.1020	1.0960	1.0908	1.0864	1.0826	1.0794	1.0768	1.0748	1.0734	1.0725	1.0720	1.0720	1.0723
3.0	1.1233	1.1159	1.1097	1.1044	1.0997	1.0959	1.0927	1.0903	1.0886	1.0875	1.0870	1.0870	1.0874
3.5	1.1445	1.1357	1.1285	1.1222	1.1167	1.1121	1.1085	1.1057	1.1036	1.1024	1.1017	1.1017	1.1022
4.0	1.1660	1.1559	1.1475	1.1403	1.1340	1.1288	1.1246	1.1213	1.1190	1.1175	1.1168	1.1168	1.1174
4.5	1.1878	1.1763	1.1668	1.1585	1.1514	1.1455	1.1407	1.1371	1.1344	1.1328	1.1320	1.1320	1.1326
5.0	1.2093	1.1964	1.1858	1.1766	1.1686	1.1620	1.1567	1.1526	1.1497	1.1478	1.1470	1.1470	1.1477
5.5	1.2314	1.2171	1.2053	1.1951	1.1863	1.1789	1.1731	1.1686	1.1653	1.3136	1.1623	1.1624	1.1631
6.0	1.2538	1.2380	1.2250	1.2138	1.2041	1.1961	1.1896	1.1847	1.1811	1.1789	1.1778	1.1779	1.1787
6.5	1.2762	1.2590	1.2448	1.2325	1.2220	1.2132	1.2062	1.2008	1.1970	1.1945	1.1934	1.1934	1.1943
7.0	1.2986	1.2799	1.2645	1.2512	1.2398	1.2303	1.2227	1.2169	1.2128	1.2101	1.2089	1.2089	1.2099
7.5	1.3215	1.3012	1.2845	1.2702	1.2579	1.2477	1.2395	1.2332	1.2287	1.2259	1.2246	1.2246	1.2257
8.0	1.3443	1.3225	1.3045	1.2891	1.2760	1.2650	1.2563	1.2495	1.2447	1.2417	1.2403	1.2403	1.2415
8.5	1.3675	1.3441	1.3249	1.3084	1.2943	1.2826	1.2733	1.2661	1.2610	1.2578	1.2563	1.2563	1.2576
9.0	1.3909	1.3659	1.3454	1.3278	1.3128	1.3004	1.2904	1.2828	1.2774	1.2739	1.2723	1.2724	1.2737
9.5	1.4146	1.3878	1.3660	1.3473	1.3314	1.3182	1.3076	1.2995	1.2938	1.2901	1.2885	1.2885	1.2899
10.0	1.4381	1.4097	1.3865	1.3667	1.3499	1.3359	1.3248	1.3163	1.3102	1.3063	1.3045	1.3046	1.3061
10.5	1.4619	1.4318	1.4073	1.3864	1.3687	1.3539	1.3422	1.3332	1.3268	1.3227	1.3209	1.3210	1.3226
11.0	1.4860	1.4543	1.4284	1.4064	1.3877	1.3722	1.3598	1.3504	1.3436	1.3394	1.3374	1.3375	1.3392
11.5	1.5099	1.4765	1.4493	1.4262	1.4065	1.3903	1.3773	1.3674	1.3603	1.3558	1.3538	1.3539	1.3557
12.0	1.5343	1.4992	1.4705	1.4462	1.4256	1.4086	1.3950	1.3846	1.3771	1.3725	1.3703	1.3705	1.3723
12.5	1.5588	1.5219	1.4918	1.4664	1.4448	1.4270	1.4127	1.4018	1.3941	1.3892	1.3870	1.3872	1.3891
13.0	1.5835	1.5447	1.5133	1.4866	1.4641	1.4455	1.4306	1.4193	1.4112	1.4061	1.4038	1.4040	1.4060